Investigation of Separate Meter-In Separate Meter-Out Control Strategies

- Master's Thesis -

Mechatronic Control Engineering

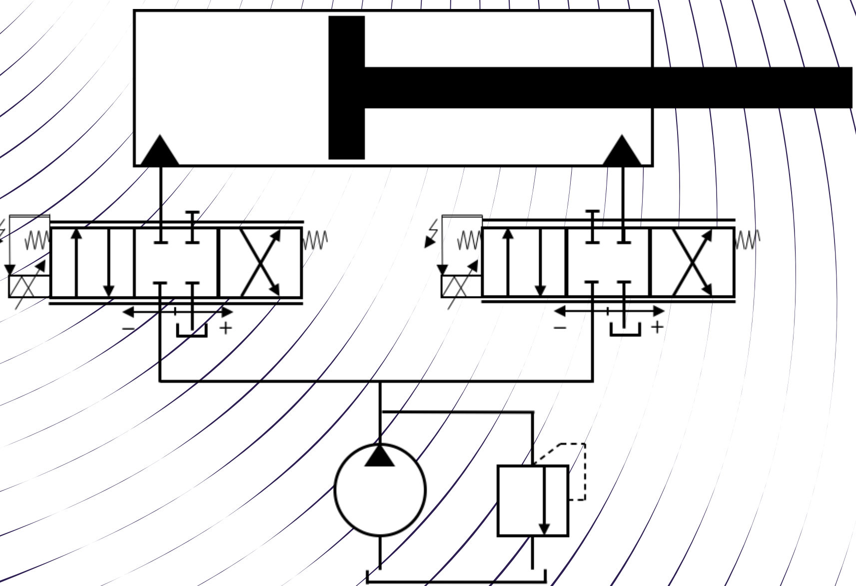

Aalborg University
Department of Energy Technology
Pontoppidanstræde 111
DK - 9220 Aalborg East

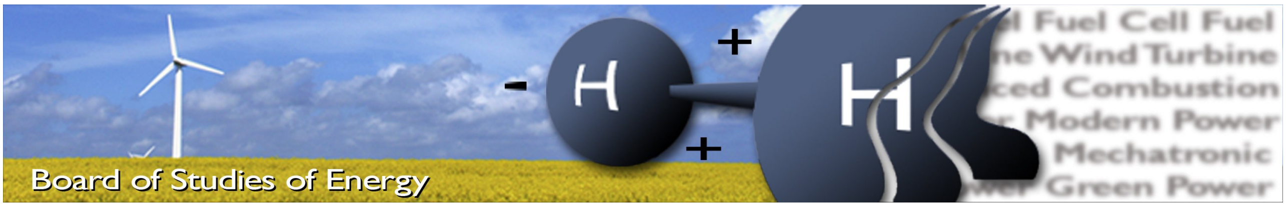

Title:	Investigation of Separate Meter-In Separate Meter-Out Control Strategies
Semester:	4^{th}
Semester theme:	Master's thesis
Project period:	3/2 2020 - 29/5 2020
ECTS:	30
Supervisor:	Henrik C. Pedersen
Project group:	MCE4-1022

Andreas Jakobsen

Jonas Tomczyk Aarup

Rikke Helena Winberg

SYNOPSIS:
The objective of this thesis is to investigate Separate Meter-In Separate Meter-Out, SMISMO, control strategies for a hydraulic cylinder. In the first part of the thesis, highly independent control combinations were found and analysed. An analytical Relative Gain Array analysis concluded that the cross coupling are heavy for certain frequencies and that the suggested input-output pairing change when varying the piston position. In the second part of the thesis, a given hydraulic system was modelled, validated, and analysed. A worst-case linearisation point was chosen and the system was found to be ill-conditioned. Three MIMO controllers were designed for velocity and pressure and compared: Pole Placement, Linear Quadratic Regulator, and Linear Quadratic Integral, LQI, controller. The LQI controller proved good results in regards to transient response, steady state accuracy, parameter variation, and disturbance rejection.

Pages, total:	176
Appendix:	38
Supplements:	0

By accepting the request from the fellow student who uploads the study group's project report in Digital Exam System, you confirm that all group members have participated in the project work, and thereby all members are collectively liable for the contents of the report. Furthermore, all group members confirm that the report does not include plagiarism.

Summary

The objective of this thesis is to investigate Separate Meter-In Separate Meter-Out, SMISMO, control strategies for a hydraulic cylinder. The thesis is divided into two main parts: a general analysis of hydraulic SMISMO systems, and analysis and control of a given hydraulic SMISMO system.

In the first part of the thesis, a control combination analysis showed that it is possible to control either flow, piston position, piston velocity, or piston acceleration along with pressure highly independently.

This led to an analytical Relative Gain Array, RGA, analysis where cross couplings were studied for parameter variations and different operating conditions. From a simplified RGA analysis with flows as inputs it was found that for low frequencies, the cross couplings depend on the piston area ratio, α, and bulk modulus ratio, γ, and that the suggested pairing of inputs and outputs change when changing the piston position from 0 [%] to 100 [%] of stroke length. For the transition frequency range it was found that whether the diagonal and off-diagonal RGA elements cross, is mostly dependent on the piston position. Furthermore, heavy cross couplings occur at the natural frequency. It was concluded that to ensure low coupling, the piston working range is very limited for low frequencies, and if controlled as SISO, the closed loop bandwidth should be designed such that frequencies above a frequency lower than the natural frequency are filtered out. Instead a decoupling pre-compensator or MIMO control was suggested to avoid heavy cross couplings and be able to increase the bandwidth.

The analytic RGA analysis was extended to include the system with valve openings as inputs. However, due to the complexity of the RGA elements when including the orifice equations, it was only possible to analyse the couplings for low and high frequencies. For low frequencies it was found that the necessary operating pressures to avoid cross couplings are very limited. The two analytical RGA analyses were compared and verified by a numerical RGA analysis, where only a low frequency offset was observed in the comparison. A numerical RGA analysis including the leakage flow, viscous friction, and dead volume showed that the conclusions made with the simplified analytic RGA analysis had an offset at low frequencies and change in resonance peak. At the intermediate frequency range, the results were, however,

similar.

The second part of the thesis focuses on the analysis and control of a given hydraulic SMISMO system. The system was modelled and validated by experimental data. An analysis of the pole locations as a function of operating parameters showed that the dynamic change of the linear model is large and very dependent on the linearisation point. A worst-case linearisation point was found as a trade-off between lowest natural frequency, lowest damping ratio, and highest system couplings. From a Singular Value Decomposition, SVD, it was found that the system gain depends on the direction of the input vector and that the system is ill-conditioned. It was concluded that the strong directionality and significant cross couplings may cause control problems. Based on the analysis of the cross couplings and SVD, it was decided to design MIMO controllers.

First, a MIMO controller using the pole placement, PP, method was designed. The poles were placed such that the natural frequency and damping ratio were increased. During the design process, it was found that the dynamics change significantly for a small change in the pole locations. The velocity and pressure outputs were able to follow the references to some degree however with errors. The load force had a significant effect on the outputs where an increase in errors was seen.

A Linear Quadratic Regulator, LQR, controller with gain scheduling was designed to check whether it was possible to improve the dynamics and reduce steady state errors. The choice of gain scheduling was based on the change in location of the poles when varying the piston position and the fact that small changes in pole locations affected the dynamics significantly. The best response was obtained for pole locations close to the open loop poles, however, the dynamics were not further improved.

Finally, a Linear Quadratic Integral, LQI, controller was designed to reduce steady state errors. Two additional integrator poles were placed closer to the origin and it was possible to move the complex conjugate pole pair further away from the origin with an increased damping ratio. The LQI controller was able to remove steady state errors and reduce overshoot for step responses. Furthermore, the LQI controller was able to follow the reference when the load force was stepped which was not the case for PP and LQR. This was also seen in the frequency response for the singular values of the sensitivity function where the gain at low frequencies is significantly smaller for LQI than for PP and LQR. In regards to measurement noise attenuation, the noise transfer function for LQI had a significant resonance peak, however, the implemented measurement noise did not affect the LQI controller as expected. In conclusion, the system with LQI control proved best results.

Contents

Preface

This master's thesis is written by group MCE4-1022 at the 4^{th} semester of the MSc in Mechatronic Control Engineering at Aalborg University. The thesis is written during the spring semester in the period 3^{rd} of February 2020 to 29^{th} of May 2020. The title of the thesis is "Investigation of Separate Meter-In Separate Meter-Out Control Strategies".

Harvard referencing style is used throughout the thesis where in-text citations are enclosed by square brackets with the name of the author, year published, and page numbers. All citations are listed in the Bibliography with the name of the author, year published, title, ISBN, and, if necessary, a note. URL's are written for websites where the year refers to the year they were read. Sections, figures, equations, and tables are referred to as, e.g. "Section 1.2", where the first number or letter refers to the chapter or appendix, and the second number refers to either the section, figure, equation, or table.

Throughout the thesis matrices and vectors are **bold**. The derivative with respect to time is marked by a dot above the symbol, e.g. $\dot{x}$, and the second derivative by two dots, e.g. $\ddot{x}$. Sub-conclusions and important points are written in *italics*.

The following software have been used during the period:

- MATLAB/Simulink for calculations and simulations
- Microsoft PowerPoint for figures
- Draw.io for block diagrams
- Overleaf for writing and editing the thesis

Nomenclature

Symbol	Description	Unit
α	Area Ratio	[-]
α	Brogan Constant	[-]
α	Air Dissolved in Oil	[%]
β	Bulk Modulus	$[Pa]$
β	Brogan Constant	[-]
γ	Bulk Modulus Ratio	[-]
γ	Condition Number	[-]
ϵ	Position Ratio	[-]
ζ	Damping Ratio	[-]
θ	Pitch Angle	$[rad]$
λ	Relative Gain Array Element	[-]
λ	Eigenvalue	[rad/s]
σ	Singular Value	[-]
τ	Torque	$[N\,m]$
τ	Time Constant	$[s]$
ψ	Angle	$[rad]$
ω	Frequency	$[rad/s]$

Symbol	Description	Unit
A	Area	$[m^2]$
a	Gain	[-]
B	Viscous Damping Coefficient	$[N\,s/m]$
B	Viscous Damping Coefficient	$[N\,m\,s/rad]$
b	Gain	[-]
C_{le}	Leakage Coefficient	$[m^3/(Pa\,s)]$
C	Coefficient	[-]
c	Hyperbolic Tangent Shaping Constant	[-]
F	Force	$[N]$
g	Transfer Function	[-]
H	Length	$[m]$
I	Inertia	$[kg\,m^2]$
k	Gain	[-]
L	Piston Stroke Length	$[m]$
M	Piston Mass	$[kg]$
n	Polytropic Index	[-]
p	Pressure	$[Pa]$
Q	Flow	$[m^3/s]$
r	Length	$[m]$
S	Length	$[m]$
s	Laplace Variable	[-]
T	Gain	[-]
u	Control Input	[-]
V	Volume	$[m^3]$

Symbol	Description
$\mathbf{A}$	System Matrix
$\mathbf{B}$	Input Matrix
$\mathbf{C}$	Output Matrix
$\mathbf{C}_o$	Controllability Matrix
$\mathbf{D}$	Feed Forward Matrix
$\boldsymbol{\Delta}$	Brogan Matrix
$\mathbf{F}$	Pre-compensator Matrix
$\mathbf{G}$	Transfer Function Matrix
$\boldsymbol{\Gamma}$	Brogan Matrix
$\mathbf{K}$	Feedback Gain matrix
$\boldsymbol{\Lambda}$	Relative Gain Array Matrix
$\mathbf{M}$	Scaling Matrix
$\mathbf{P}$	Riccati Solution Matrix
ψ	Eigenvector
$\mathbf{Q}$	State Weight Matrix
$\mathbf{R}$	Input Weight Matrix
$\mathbf{r}$	Reference Vector
$\boldsymbol{\Sigma}$	Singular Value Matrix
$\mathbf{U}$	Left Singular Matrix
$\mathbf{U}$	Brogan Matrix
$\mathbf{u}$	Input Vector
$\mathbf{V}$	Right Singular Matrix
ξ	Brogan Matrix
$\mathbf{x}$	State Vector
$\mathbf{y}$	Output Vector

Abbreviation	Description
LQG	Linear Quadratic Gaussian
LQI	Linear Quadratic Integral
LQR	Linear Quadratic Regulator
MAE	Mean Absolute Error
MIMO	Multiple-Input Multiple-Output
PP	Pole Placement
RGA	Relative Gain Array
RHS	Right Hand Side
SISO	Single-Input Single-Output
SMISMO	Seperate Meter-In Seperate Meter-Out
SVD	Singular Value Decomposition

Chapter 1

Introduction

Traditionally, mechanically linked meter-in meter-out spool valves are used for hydraulic differential cylinders [Hansen et al., 2011a]. The conventional valve offers a variety of control options, e.g. control of piston position, piston velocity, orifice flow, chamber pressure, and piston force. The control options are, however, primarily standalone options due to only one control input being available. Due to a larger focus on energy-saving, it is beneficial to control two states, e.g. flow and pressure. This is possible with a Separate Meter-In Separate Meter-Out, SMISMO, configuration where the valve opening to each chamber is controlled separately [Guangrong et al., 2019]. This utilises the possibility to control an additional variable compared to a mechanically linked meter-in meter-out spool valve [Rath and Zaev, 2017] which increases the functionality of the system and could improve dynamic performance. This thesis will, therefore, investigate suitable control strategies for a hydraulic cylinder using SMISMO.

The thesis is divided into two main parts. The first part contains a general analysis of hydraulic SMISMO systems and can be used as a guideline for a hydraulic cylinder controlled by SMISMO valves. The second part contains an analysis and control of a given hydraulic SMISMO system where the conclusions from the first part form the basis for the second part.

The first part of the thesis will investigate:

- *What are the suitable pairings of control variables for a hydraulic cylinder using SMISMO?*
- *How do operating conditions and parameter variations influence the system couplings?*

These questions will be answered in a general perspective without considering the application. Figure 3.1 is used for the analysis where each relevant system parameter is varied.

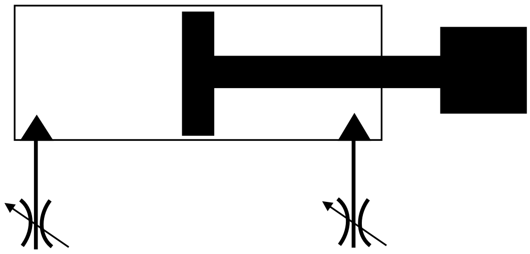

Figure 1.1: Sketch of the differential cylinder used for the analysis.

Several pairings of control variables arise and the variables considered to determine suitable control strategies are: flow in both chambers, piston position, piston velocity, piston acceleration, pressure in both chambers, and piston force. By answering the questions without considering the application, this first part of the thesis can be used as a guide when using SMISMO for a hydraulic cylinder.

The second part of the thesis contains an analysis of a specific hydraulic test setup using SMISMO and will investigate:

- *How can controllers be designed for the system to reduce reference tracking error?*

The reference tracking is evaluated during the transients and in steady state, and the system should be insensitive to parameter variations and robust towards disturbances. The controllers will be designed based on the analysis of suitable pairings and the coupling analysis. The chosen controllers will be tested by simulation where the performance is compared for a chosen reference profile. Noise will be implemented in the simulation since the controllers will not be tested experimentally as there is no access to the laboratory due to the coronavirus pandemic. The comparison is done for the specific system and will depend on the used approach. The conclusion of the recommended controller design can, therefore, change when using SMISMO for other systems.

Part I

General Analysis of Hydraulic SMISMO Systems

Chapter 2

General Dynamic Model

This chapter is the beginning of Part I. In Part I, the following question will be answered first: *What are the suitable pairings of control variables for a hydraulic cylinder using SMISMO?*

A general hydraulic model for a differential cylinder with two orifice openings as inputs is presented in this chapter. The system equations are later used to determine if each control combination is suitable. The model is based on commonly used equations for describing such a system where modelling differences may occur when considering the fluid stiffness, leakage flow, and friction model. The differential hydraulic cylinder is sketched in Figure 2.1 where the subscript 'p' refers to the piston side and 'r' refers to the rod side of the cylinder.

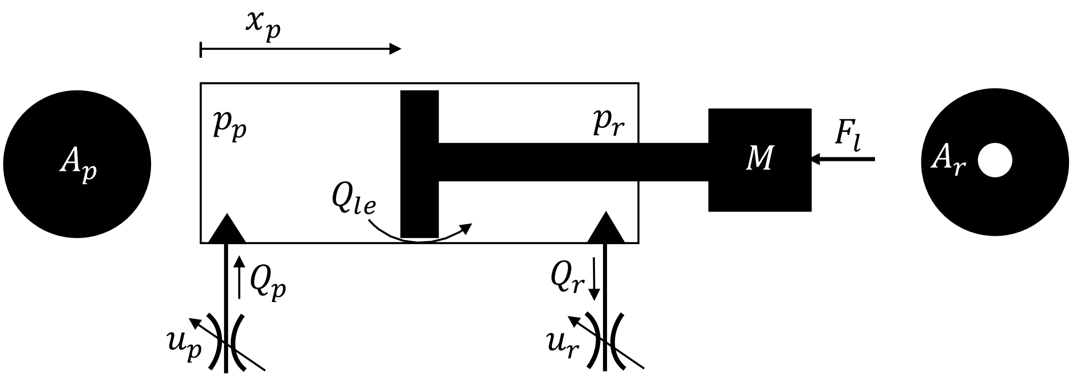

Figure 2.1: Differential cylinder in SMISMO configuration.

The system inputs, u_p and u_r, pressure in each chamber, p_p and p_r, flows, Q_p and

Q_r, leakage flow, Q_{le}, piston areas, A_p and A_r, mass, M, load force, F_l, and piston position, x_p, are defined in Figure 2.1. For a differential cylinder it follows that $A_p > A_r$. The orifices in Figure 2.1 are not modelled, however, the valve openings, u_p and u_r, are considered inputs to the system and will be modelled later.

The continuity equation for each cylinder chamber is expressed in Equations (2.1) and (2.2) where external leakage is neglected[Hansen, 2019, 76-78].

$$Q_p - Q_{le} = A_p\,\dot{x}_p + \frac{V_p}{\beta(p_p)}\,\dot{p}_p \tag{2.1}$$

$$Q_{le} - Q_r = -A_r\,\dot{x}_p + \frac{V_r}{\beta(p_r)}\,\dot{p}_r \tag{2.2}$$

β is the effective bulk modulus which is defined in Equation (2.3)[Hansen, 2019, 16-17], where α is the percentage of air dissolved in the oil, n is the polytropic index which is 1.4 for an adiabatic process, p_0 is the atmospheric pressure, and β_0 is the maximum fluid stiffness.

$$\beta = \frac{(1-\alpha)\,e^{\frac{p_0-p}{\beta_0}} + \alpha\left(\frac{p_0}{p}\right)^{\frac{1}{n}}}{\frac{1-\alpha}{\beta_0}\,e^{\frac{p_0-p}{\beta_0}} + \frac{\alpha}{n\,p_0}\left(\frac{p_0}{p}\right)^{\frac{n+1}{n}}} \tag{2.3}$$

The internal leakage flow is expressed in Equation (2.4) and the volumes in Equations (2.5) and (2.6)[Hansen, 2019, 76-78].

$$Q_{le} = C_{le}\,(p_p - p_r) \tag{2.4}$$

$$V_p = A_p\,x_p + V_{p0} \tag{2.5}$$

$$V_r = A_r\,(L - x_p) + V_{r0} \tag{2.6}$$

C_{le} is the leakage coefficient, L is the cylinder stroke length, V_{p0} is the piston side volume when $x_p = 0$, and V_{r0} is the rod side volume when $x_p = L$, i.e. the dead volumes.

The free body diagram of the cylinder is sketched in Figure 2.2 and the acting forces are expressed in Equation (2.7) using Newton's Second Law of Motion [Hansen, 2019, 78-79].

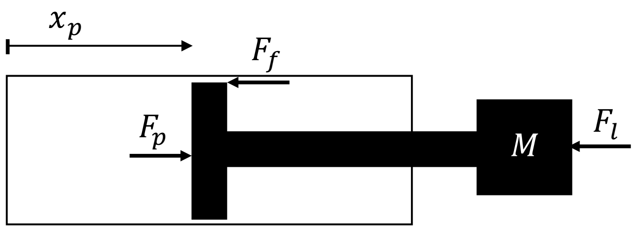

Figure 2.2: Free body diagram of a differential cylinder.

$$\sum F = M\,\ddot{x}_p = F_p - F_f - F_l \tag{2.7}$$

Where F_p is the piston force which is the force contribution from the pressure in each chamber acting on each side of the piston head, F_f is the friction force acting against the direction of movement which arises from the seals between piston and cylinder, and F_l is the load force. The piston- and friction forces are defined in Equations (2.8) and (2.9)[Hansen, 2019, 78-79].

$$F_p = A_p\,p_p - A_r\,p_r \tag{2.8}$$

$$F_f = B\,\dot{x}_p + F_c\,sgn(\dot{x}_p) \tag{2.9}$$

B is the viscous damping coefficient and F_c is the Coulomb friction coefficient. The three non-linear governing differential equations are rewritten in Equations (2.10) to (2.12).

$$\ddot{x}_p = \frac{1}{M}(A_p\,p_p - A_r\,p_r - B\,\dot{x}_p - F_c\,sgn(\dot{x}_p) - F_l) \tag{2.10}$$

$$\dot{p}_p = \frac{\beta(p_p)}{A_p\,x_p + V_{p0}}(Q_p - C_{le}\,(p_p - p_r) - A_p\,\dot{x}_p) \tag{2.11}$$

$$\dot{p}_r = \frac{\beta(p_r)}{A_r\,(L - x_p) + V_{r0}}(C_{le}\,(p_p - p_r) - Q_r + A_r\,\dot{x}_p) \tag{2.12}$$

A general hydraulic model has now been derived and will be used for further analyses. It should be noted that the equations are representative for a physical hydraulic system and the system parameters for a specific test setup will therefore not be validated to retain generality. Instead, the parameters will be varied within physical grounds during analyses and the results should, therefore, apply for systems that are modelled using the corresponding equations.

Chapter 3

Control Combination Analysis

The purpose of the following analysis is to investigate the different control combinations which arise from a SMISMO configuration. All combinations are studied to find out whether they are suitable for control purposes. The suitable control combinations are further analysed to determine whether they can be controlled independently of each other. The hydraulic cylinder used for the analysis was modelled in Chapter 2 and sketched in Figure 3.1.

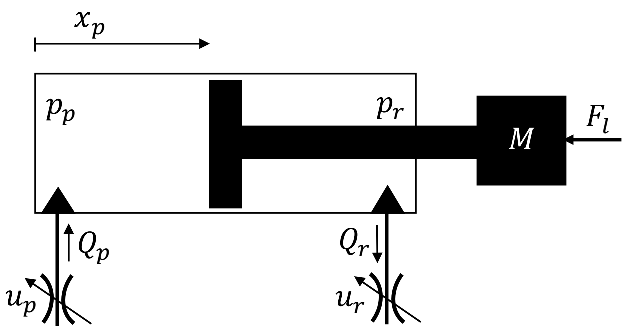

Figure 3.1: Differential cylinder used for analysis.

The governing differential Equations (2.10) to (2.12) are simplified in order to reduce the complexity of the analysis. The frictional forces $F_f = B\,\dot{x}_p + F_c\,sgn(\dot{x}_p)$ are modelled as a part of the load force, F_l, as seen in Equation (3.1). However, the velocity dependency of the load force is considered negligible compared to the size of the load force. The magnitude of the load force is unknown. The leakage flow is neglected, and the volumes V_p and V_r are seen as constants to further simplify the model. The simplified differential equations are shown in Equations (3.1) to (3.3).

$$\ddot{x}_p = \frac{1}{M}(F_p - F_l) \tag{3.1}$$

$$\dot{p}_p = \frac{\beta(p_p)}{V_p}(Q_p - A_p\,\dot{x}_p) \tag{3.2}$$

$$\dot{p}_r = \frac{\beta(p_r)}{V_r}(A_r\,\dot{x}_p - Q_r) \tag{3.3}$$

The piston force, F_p is defined in Equation (3.4).

$$F_p = p_p\,A_p - p_r\,A_r \tag{3.4}$$

At steady state, i.e. constant pressures and velocity, the governing differential equations are simplified as shown in Equations (3.5) to (3.7).

$$0 = p_p A_p - p_r A_r - F_l \tag{3.5}$$

$$0 = Q_p - A_p\,\dot{x}_p \tag{3.6}$$

$$0 = A_r\,\dot{x}_p - Q_r \tag{3.7}$$

The equations have now been simplified to limit the analyses conducted during the first part. After the analyses, the simplifications are evaluated in Section 5.5 by comparison of the simplified equations with the initial equations to determine the effects on the final conclusions.

3.1 Suitable Control Combinations

Each control option will be analysed to determine if the control option is suitable or not. In Table 3.1 all the control combinations are shown, where the states in the vertical axis are controlled with one valve, and the horizontal states are controlled with the other valve. The valve orifices are directly controlled using control inputs u_p and u_r for the piston and rod side valve, respectively. For the bottom row referred to as 'Slave', one valve is opened as a function of the other, which is elaborated later. The specific input and output pairing of the control inputs is not considered in the following analysis, as this is discussed in Chapter 5.

	Q_p	Q_r	x_p	$\dot{x}_p$	$\ddot{x}_p$	p_p	p_r	F_p	Slave
Q_p	×								
Q_r	×	×							
x_p	✓	✓	×						
$\dot{x}_p$	×	×	✓	×					
$\ddot{x}_p$	✓	✓	✓	✓	×				
p_p	✓	✓	✓	✓	✓	×			
p_r	✓	✓	✓	✓	✓	×	×		
F_p	✓	✓	✓	✓	×	×	×	×	
Slave	✓	✓	✓	✓	✓	✓	✓	✓	×

Table 3.1: Output combinations.

The vertical state is parred with the horizontal state and the control suitability for each combination is determined. *If a control combination is not able to achieve steady state, it is not suitable.* The control options marked with a red cross are not suitable, the control options with yellow checkmarks are suitable but the states should be controlled dependent on each other, and control options marked with green checkmarks are suitable and can be controlled highly independent of each other, however, reference limits exist. As an example, controlling F_p and x_p is suitable but cannot be controlled independently of each other as a yellow checkmark is given, whereas, controlling p_r and x_p instead can be done highly independently of each other as a green checkmark is given. All the control combinations that are not suitable are explained first whereafter the suitable control options are explained.

MISO Control

The diagonal of Table 3.1 would require two inputs both controlling one state e.g. MISO. MISO is disregarded, as the possibility to control one state is not the focus of this thesis.

Flows

In this section, the outputs Q_r and Q_p are analysed. The pressure gradients should equal zero in steady state: $0 = Q_p - A_p\,\dot{x}_p$ and $0 = A_r\,\dot{x}_p - Q_r$ which is desired for control purposes. Q_p and Q_r are algebraically connected and therefore strictly dependent on each other. If Q_p and Q_r do not match, it would result in two different velocities, $\dot{x}_p$, and the system will not reach steady state, i.e. $\dot{x}_p = \frac{Q_p}{A_p} \neq \frac{Q_r}{A_r}$. This could be caused by the areas not being modelled correctly or an unmodelled external leakage in e.g. one of the valves, which results in more flow exiting this chamber. *Controlling both flows is therefore not suitable.*

Piston Velocity and Flows

In this section, the outputs $\dot{x}_p$ and Q_p and the outputs $\dot{x}_p$ and Q_r are analysed. In steady state, the pressure gradients equal zero and from Equation (3.5), $\dot{x}_p = \frac{Q_p}{A_p}$ which means the piston velocity, $\dot{x}_p$, and flow, Q_p, are algebraically coupled. $\dot{x}_{p,ref}$ can therefore not be set independently of $Q_{p,ref}$. If $Q_{p,ref}$ is set dependent on the chosen $\dot{x}_{p,ref}$ and A_p or leakage is modelled incorrectly, $Q_{p,ref}$ will result in a velocity different than the wanted $\dot{x}_{p,ref}$ and the system will not be able to reach steady state which is desired for control purposes. *Controlling both the velocity and flow is therefore not suitable.*

Piston Force and Piston Acceleration

In this section, the outputs F_p and $\ddot{x}_p$ are analysed. The relation between F_p and $\ddot{x}_p$ is given by: $\ddot{x}_p = \frac{1}{M}(\overbrace{p_p A_p - p_r A_r}^{F_p} - F_l)$. As the load force, F_l is unknown, a reference for the piston force F_p can not be set to guarantee $\ddot{x}_p = 0$ and thereby reach steady state. *Controlling both the piston force and piston acceleration is therefore not suitable.*

Pressures

In this section, the outputs p_r and p_p are analysed. Controlling the two pressures, and achieving steady state, would require knowledge of the load force as seen by: $0 = p_p A_p - p_r A_r - F_l$. If the pressure references do not match the load force, an acceleration occurs and the system does not reach steady state. *Controlling both pressures is therefore not suitable.*

Piston force and Pressures

In this section, the outputs F_p and p_p and the outputs F_p and p_r are analysed. The piston force, F_p, is defined by $F_p = p_p A_p - p_r A_r$. Due to the unknown load force, F_p can be found from the pressure measurements of p_p and p_r. It follows from the definition of the piston force that if $p_{p,ref}$ and $F_{p,ref}$ are chosen, then p_r is predetermined. The value of p_r does not necessarily result in steady state as the load force is unknown. *Controlling the piston force and pressure is, therefore, comparable to controlling both pressures which is not suitable.*

3.2 Dependent and Independent Control Combinations

It will be analysed if each control combination is able to move the piston in both positive and negative direction with a positive and negative load force for each direction. This result in the four cases shown in Figure 3.2, where the defined positive direction of the velocity and load force is shown in case 2.

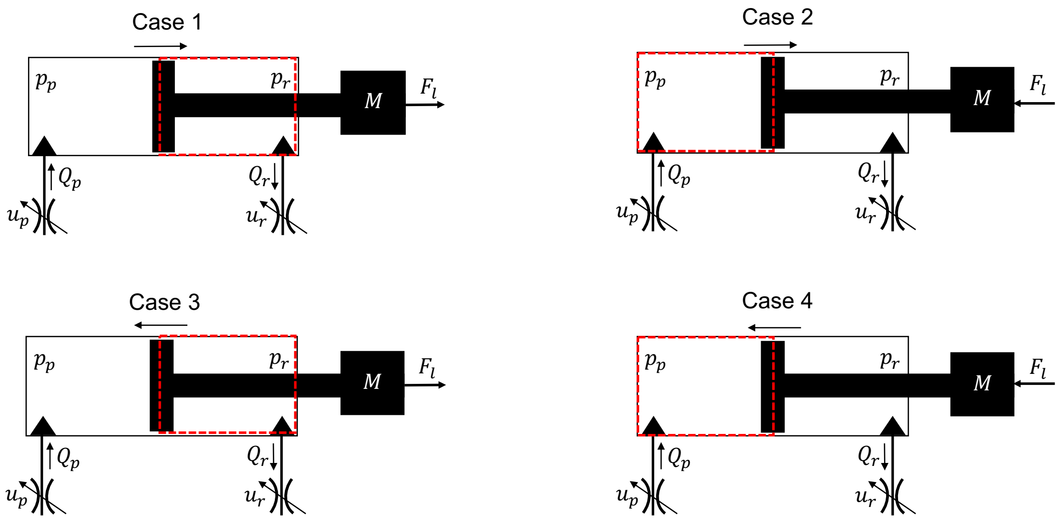

Figure 3.2: Four force and piston direction cases where the load carrying chamber is enclosed by red dashed lines.

The maximum magnitude of the piston force is defined to be larger than the maximum magnitude of the load force. As the areas of the piston are different, the maximum load force is dependent on the direction of the load force. The maximum positive load force, $F_{l,pos}$, is defined as $F_{l,pos} = p_s A_p - p_t A_r$ and the maximum negative load force, $F_{l,neg}$, is defined as $F_{l,neg} = p_t A_p - p_s A_r$. It should be noted that $|F_{l,neg}| < |F_{l,pos}|$ for a differential cylinder.

The control options marked with yellow checkmarks in Table 3.1 where the states must be controlled dependent on each other are explained first and the green checkmarks where the states can be controlled highly independent of each other are explained afterwards.

Piston Position and Flows

In this section, the outputs x_p and Q_p and the outputs x_p and Q_r are analysed. As x_p is the integral of $\dot{x}_p$, and $\dot{x}_p$ is algebraically connected to Q in steady state, x_p and Q can not be controlled independently. As an example, a constant position reference would contradict a velocity reference different from zero.

Instead, it is possible to control the position and flow dependent on each other. The position is the integral of the velocity, which means it is possible to feed back velocity and position in a cascade configuration; the position will then be fed back in the outer loop and the velocity in the inner loop. As flow is algebraically connected to velocity, the flow reference, Q_{ref}, can be generated based on the position error $x_{p,error} = x_{p,ref} - x_p$, i.e $Q_{ref}(x_{p,error})$. *It is possible to control the flow dependent on the position error.*

The argumentation for a cascade configuration is used for all yellow checkmarks except for slave.

Piston Acceleration and Flows

In this section, the outputs $\ddot{x}_p$ and Q_p and the outputs $\ddot{x}_p$ and Q_r are analysed. Q is closely related to $\dot{x}_p$ and $\dot{x}_p$ is the integral of $\ddot{x}_p$. Q and $\ddot{x}_p$ can thereby not be controlled independently.

The same argumentation follows as for piston position and flows. The acceleration reference is calculated based on the flow error, i.e. $\ddot{x}_{p,ref}(Q_{error})$, and controlled in a cascade configuration with acceleration in the inner loop and flow in the outer loop. *It is possible to control the piston acceleration dependent on the flow error.*

Piston Velocity and Position

In this section, the outputs $\dot{x}_p$ and x_p are analysed. The same argumentation follows as for piston position and flows. The velocity reference is calculated based on the position error, i.e. $\dot{x}_{p,ref}(x_{p,error})$, and controlled in a cascade configuration with velocity in the inner loop and position in the outer loop. *It is possible to control the piston velocity dependent on the position error.*

Piston Acceleration and Position

In this section, the outputs $\ddot{x}_p$ and x_p are analysed. The same argumentation follows as for piston position and flows, however, with a double integrator. The acceleration reference is calculated based on the position error, i.e. $\ddot{x}_{p,ref}(x_{p,error})$, and controlled in a cascade configuration with acceleration in the inner loop and position in the outer loop. *It is possible to control the piston acceleration dependent on the position error.*

Piston Acceleration and Velocity

In this section, the outputs $\ddot{x}_p$ and $\dot{x}_p$ are analysed. The same argumentation follows as for piston position and flows. The acceleration reference is calculated based on the velocity error, i.e. $\ddot{x}_{p,ref}(\dot{x}_{p,error})$, and controlled in a cascade configuration with acceleration in the inner loop and velocity in the outer loop. *It is possible to control the piston acceleration dependent on the velocity error.*

Piston Force and Flows

In this section, the outputs F_p and Q_p and the outputs F_p and Q_r are analysed. The piston force is related to piston acceleration: $\ddot{x}_p = \frac{1}{M}(\overbrace{p_p A_p - p_r A_r}^{F_p} - F_l)$, and the flow is related to piston velocity. Due to the unknown load force, F_p can be found from the pressure measurements of p_p and p_r.

To control the piston force and flow, the same argumentation follows as for piston position and flows. The piston force reference is calculated based on the flow error, i.e. $F_{p,ref}(Q_{error})$, and controlled in a cascade configuration with piston force in the inner loop and flow in the outer loop. *It is possible to control the piston force dependent on the flow error.*

Piston Force and Piston Position

In this section, the outputs F_p and x_p are analysed. As F_p is comparable to the piston acceleration, the same argumentation follows as for piston position and flows, however, with a double integrator. The piston force reference is calculated based on the position error, i.e. $F_{p,ref}(x_{p,error})$, and controlled in a cascade configuration with piston force in the inner loop and position in the outer loop. *It is possible to control the piston force dependent on the position error.*

Piston Force and Piston Velocity

In this section, the outputs F_p and $\dot{x}_p$ are analysed. As F_p is comparable to the piston acceleration, the same argumentation follows as for piston position and flows. The piston force reference is calculated based on the velocity error, i.e. $F_{p,ref}(\dot{x}_{p,error})$, and controlled in a cascade configuration with piston force in the inner loop and velocity in the outer loop. *It is possible to control the piston force dependent on the velocity error.*

Slave Control

Slave control can be used when only controlling for one state, where one input is paired with the wanted state and the other input is determined from the area ratio and the opening of the first input: $u_r = u_p \frac{A_r}{A_p}$. Using this relationship between the inputs, the system will reach steady state under the assumption that the valve coefficients and pressure differences across the vales are equal. The slave control method is comparable to using one conventional valve connected to the two chambers, where the valve spool position allows flow to enter one chamber, and exit the other as they are mechanically linked.

Flow: Flow control of either flow is possible and if the area ratio of the piston surface, $\alpha = A_r/A_p$, is modelled incorrectly, then $Q_r \neq Q_p\alpha$. This will however not necessarily result in pressure build-up since an increased pressure will result in an increased flow out of the chamber.

Position: Since the valves are coupled, Q_p and Q_r will be positive at the same time or negative at the same time which will guarantee movement in the wanted direction. A constant velocity is furthermore achieved by keeping the valve opening constant.

Velocity: As for controlling the position with slave, the valves will ensure movement in the wanted direction. The wanted velocity is achieved by adjusting the valve opening.

Acceleration: The same argument applies as for position and velocity.

Pressure and Piston Force: Controlling the pressures and piston force using slave is comparable and possible however limited, as the pressure built up in one chamber is dependent on the opposite chamber pressure, which is not directly controlled. Furthermore, the achievable pressure and piston force are dependent on the load force.

All the combinations that must be controlled depending on each other have been analysed. The states that can be controlled highly independent of each other will be analysed in the following sections.

Pressures and Flows

In this section, the outputs p_p and Q_p, the outputs p_p and Q_r, the outputs p_r and Q_p, and the outputs p_r and Q_r are analysed. The four cases from Figure 3.2 are used for the analysis.

Case 1:

A low pressure reference in the rod side chamber allows runaway of the load, as the unknown load force acts in the same direction as the desired movement, i.e. an overrunning load. Controlling the piston side pressure and rod side flow implies balancing of the load as Q_r is controlled in the load carrying chamber.[Hansen et al., 2011b] $p_{p,ref}$ and Q_{ref} are highly independent of each other, however, when the $p_{p,ref}$ approaches p_s, Q_{ref} becomes limited due to the low pressure difference across the valve.

Case 2:

The load is resistive and controlling the pressure in the load carrying chamber would require the reference to be pump pressure, $p_{p,ref} = p_s$, to guarantee movement in the desired direction due to the load force being unknown. A pressure reference set too low would risk the piston moving in the negative direction. Controlling the flow in either of the chambers is possible, however as for case 1, the flow in the load carrying chamber implies balancing the load. Having a pressure reference in the rod side chamber enables the piston side chamber pressure to adjust according to the load force.

If a control combination for flow and pressure works for case 1 then it also works for case 4 when changing to control the other flow and pressure, respectively. The same is true for cases 2 and 3, only the pressure in the load carrying chamber should be the supply pressure in case 3.

The pressure should be controlled in the non-load carrying chamber. It is recommended to control the flow in the load carrying chamber.

Pressures and Piston Position

In this section, the outputs p_p and x_p and the outputs p_r and x_p are analysed.

Case 1:

The same argumentation follows as for case 1 for controlling pressure and flow. The pressure in the non-load carrying chamber should be controlled, i.e. p_p. p_r, Q_r, and Q_p will thereby adjust according to the chosen $p_{p,ref}$, $x_{p,ref}$, and the load force.

Case 2: The same argumentation follows as for case 2 for controlling pressure and flow. The pressure in the non-load carrying chamber should be controlled, i.e. p_r. p_p, Q_r, and Q_p will thereby adjust according to the chosen $p_{r,ref}$, $x_{p,ref}$, and the load force.

For case 3 and 4, the same augmentation for case 1 and 2 applies. *The pressure should be controlled in the non-load carrying chamber.*

Pressures and Piston Velocity

In this section, the outputs p_p and $\dot{x}_p$ and the outputs p_r and $\dot{x}_p$ are analysed. The same argumentation as for pressure and piston position applies. *The pressure should be controlled in the non-load carrying chamber.*

Pressures and Piston Acceleration

In this section, the outputs p_p and $\ddot{x}_p$ and the outputs p_r and $\ddot{x}_p$ are analysed. The piston acceleration and pressure in each chamber are related as: $\ddot{x}_p = \frac{1}{M}(p_p\, A_p - p_r\, A_r - F_l)$. If $\ddot{x}_p$ is to be controlled, the pressure reference in one chamber can be chosen while the pressure in the other chamber will change depending on $\ddot{x}_{p,ref}$ and the load force. Compared to controlling F_p and $\ddot{x}_p$ which was not suitable, a degree of freedom arises, as the other pressure is not controlled. $\ddot{x}_p$ and pressure can thereby be chosen independently of each other.

Hereafter, the same argumentation as piston position and pressure applies. *The pressure should be controlled in the non-load carrying chamber.*

All the suitable control combinations are found and marked by yellow and green checkmarks in Table 3.1 which answers the question: *What are the possible control strategies for a hydraulic differential cylinder using SMISMO?* The table is repeated below with only green checkmarks where the combinations are numbered.

	Q_p	Q_r	x_p	$\dot{x}_p$	$\ddot{x}_p$
p_p	$\checkmark^1$	$\checkmark^3$	$\checkmark^5$	$\checkmark^7$	$\checkmark^9$
p_r	$\checkmark^2$	$\checkmark^4$	$\checkmark^6$	$\checkmark^8$	$\checkmark^{10}$

Table 3.2: Highly independent control combinations.

The couplings of all the combinations with a green checkmark, where the states can be controlled highly independent, will be analysed to answer the second problem; *How do operating conditions and parameter variations influence the system couplings?*

The couplings between the vertical and horizontal states in Table 3.2 will be analysed using the relative gain array, RGA. This will be done analytically to see how the couplings depend on operating conditions and parameter variations. The conclusion is afterwards numerically validated by using parameters for a SMISMO test setup. State space models are derived in the following section which are used for the RGA analysis.

Chapter 4

Linear State Space Models

Two state space models are derived to analyse the couplings analytically. The first with flows as inputs, i.e. without the non-linear orifice equations, and the second with valve openings as inputs. Both models neglect the leakage flow and viscous friction which is done to simplify the analytic coupling analysis. The load force and the Coulomb friction are modelled as a disturbance and not included in the state space model. The volume dependency of the piston position will furthermore be neglected when deriving the state space models. The volumes will however later be varied by varying the piston position and the change of coupling will be analysed.

The state space models are derived in Section 4.1 and 4.2, and an extended state space model is derived in Section 4.3 which will be used to numerically verify the simplifications made in the analytic coupling analysis.

4.1 Model with Flows as Inputs

A general non-linear state space model is expressed in Equation (4.1)[Goodwin et al., 2000, p. 53], where $\mathbf{x}$ is the state vector, $\mathbf{u}$ is the input vector, and $\mathbf{y}$ is the output vector.

$$\begin{aligned}\dot{\mathbf{x}} &= \mathbf{f}(\mathbf{x}, \mathbf{u}) \\ \mathbf{y} &= \mathbf{h}(\mathbf{x})\end{aligned} \tag{4.1}$$

The state and inputs vectors of the model with flows as inputs are defined in Equation (4.2) where the subscript 'f' refers to flows as inputs.

$$\mathbf{x}_f = \begin{bmatrix} \dot{x}_p & p_p & p_r \end{bmatrix}^T \qquad \mathbf{u}_f = \begin{bmatrix} Q_p & Q_r \end{bmatrix}^T \tag{4.2}$$

The non-linear state space model is expressed in Equation (4.3) by using the simplified differential Equations (3.1) to (3.3). It should be noted that the differential equations are linear in this case as the bulk modulus and volumes are evaluated in a linearisation point.

$$\mathbf{f}_f(\mathbf{x}_f, \mathbf{u}_f) = \begin{bmatrix} \dot{x}_{f,1} \\ \dot{x}_{f,2} \\ \dot{x}_{f,3} \end{bmatrix} = \begin{bmatrix} \frac{1}{M}(p_p\, A_p - p_r\, A_r - F_l) \\ \frac{\beta(p_p^*)}{V_p(x_p^*)}(Q_p - A_p\, \dot{x}_p) \\ \frac{\beta(p_r^*)}{V_r(x_p^*)}(A_r\, \dot{x}_p - Q_r) \end{bmatrix} \tag{4.3}$$

To get a linear state space model, new variables are introduced: $\tilde{\mathbf{x}} = \mathbf{x} - \mathbf{x}^*$, $\tilde{\mathbf{u}} = \mathbf{u} - \mathbf{u}^*$, and $\tilde{\mathbf{y}} = \mathbf{y} - \mathbf{y}^*$. Asterisks, *, denote linearisation points which are found in an equilibrium point by satisfying Equation (4.4).[Hansen, 2019, 150-153]

$$\begin{aligned} \mathbf{0} &= \mathbf{f}(\mathbf{x}^*, \mathbf{u}^*), \\ \mathbf{y}^* &= \mathbf{h}(\mathbf{x}^*) \end{aligned} \tag{4.4}$$

The linear state space model is expressed using Taylor series neglecting higher order terms. The state equation is expressed in Equation (4.5) and the output equation is expressed in Equation (4.6)[Goodwin et al., 2000, p. 52-54].

$$\dot{\tilde{\mathbf{x}}} \approx \underbrace{\left.\frac{\partial\, \mathbf{f}}{\partial\, \mathbf{x}}\right|_{\mathbf{x}^*,\mathbf{u}^*}}_{\mathbf{A}} \tilde{\mathbf{x}} + \underbrace{\left.\frac{\partial\, \mathbf{f}}{\partial\, \mathbf{u}}\right|_{\mathbf{x}^*,\mathbf{u}^*}}_{\mathbf{B}} \tilde{\mathbf{u}} = \mathbf{A}\, \tilde{\mathbf{x}} + \mathbf{B}\, \tilde{\mathbf{u}} \tag{4.5}$$

$$\tilde{\mathbf{y}} \approx \underbrace{\left.\frac{\partial\, \mathbf{h}}{\partial\, \mathbf{x}}\right|_{\mathbf{x}^*,\mathbf{u}^*}}_{\mathbf{C}} \tilde{\mathbf{x}} + \underbrace{\left.\frac{\partial\, \mathbf{h}}{\partial\, \mathbf{u}}\right|_{\mathbf{x}^*,\mathbf{u}^*}}_{\mathbf{D}} \tilde{\mathbf{u}} = \mathbf{C}\, \tilde{\mathbf{x}} + \mathbf{D}\, \tilde{\mathbf{u}} \tag{4.6}$$

where $\mathbf{A}$, $\mathbf{B}$, $\mathbf{C}$, and $\mathbf{D}$ are Jacobian matrices evaluated in the linearisation point. The state equation is expressed in Equation (4.7), whereas the $\mathbf{C}$ matrix is varied for the output equation $\mathbf{y} = \mathbf{C}\mathbf{x}$ for different control combinations.[Philips and Parr, 2013, 84-87] Tildes, $\tilde{}$, are omitted for simplicity.

$$\dot{\mathbf{x}}_f = \underbrace{\begin{bmatrix} 0 & \frac{A_p}{M} & -\frac{A_r}{M} \\ -\frac{\beta_p^* A_p}{V_p^*} & 0 & 0 \\ \frac{\beta_r^* A_r}{V_r^*} & 0 & 0 \end{bmatrix}}_{\mathbf{A}_f} \mathbf{x}_f + \underbrace{\begin{bmatrix} 0 & 0 \\ \frac{\beta_p^*}{V_p^*} & 0 \\ 0 & -\frac{\beta_r^*}{V_r^*} \end{bmatrix}}_{\mathbf{B}_f} \mathbf{u}_f \tag{4.7}$$

Transfer function matrices are found for all control combinations, i.e. **C** matrices, using Equation (4.8).[Philips and Parr, 2013, 104-105]

$$\mathbf{G}(s) = \mathbf{C}\left(s\,\mathbf{I} - \mathbf{A}\right)^{-1}\mathbf{B} \tag{4.8}$$

which yields a 2x2 matrix for a system with two inputs and two outputs. To get piston position, x_p, and piston acceleration, $\ddot{x}_p$, as output, transfer functions with piston velocity, $\dot{x}_p$, as output are found and multiplied by $1/s$ and s, respectively. It should be noted that the first state model is used to find transfer functions for the control combinations $5 - 10$ in Table 3.2 as flows are inputs. The linear model block diagram for flows as inputs is shown in Figure 4.1.

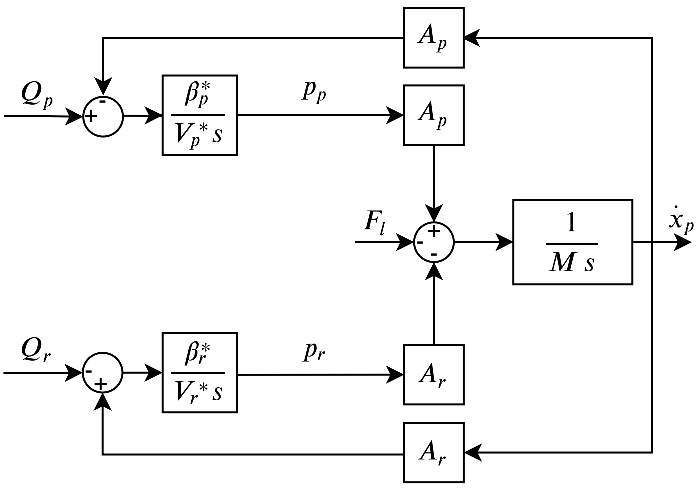

Figure 4.1: Linear model diagram for the model with flows as inputs.

The state space model is modified to have valve openings as inputs in the following section. This further allows the flow to be the output of the state space model.

4.2 Model with Valve Openings as Inputs

The orifice equations are included to get valve openings as inputs. The orifice equations are expressed in Equations (4.9) and (4.10)[Hansen, 2019, p. 92-93].

$$Q_p = \begin{cases} k_v x_{vp} \sqrt{|p_s - p_p|} \frac{(p_s - p_p)}{|p_s - p_p|}, & x_{vp} \geq 0 \\ k_v \, |x_{vp}| \, \sqrt{|p_t - p_p|} \frac{(p_t - p_p)}{|p_t - p_p|}, & x_{vp} < 0 \end{cases} \tag{4.9}$$

$$Q_r = \begin{cases} k_v x_{vr} \sqrt{|p_r - p_t|} \frac{(p_r - p_t)}{|p_r - p_t|}, & x_{vr} \geq 0 \\ k_v \, |x_{vr}| \, \sqrt{|p_r - p_s|} \frac{(p_r - p_s)}{|p_r - p_s|}, & x_{vr} < 0 \end{cases} \tag{4.10}$$

where x_{vp} and x_{vr} are the valve openings, p_s is the supply pressure, and p_t is the tank pressure. It is assumed that the valve coefficient, k_v, is constant. The state vector and new input vector are expressed in Equation (4.11) where the subscript 'v' refers to valve openings as inputs.

$$\mathbf{x}_v = \begin{bmatrix} \dot{x}_p & p_p & p_r \end{bmatrix}^T \qquad \mathbf{u}_v = \begin{bmatrix} x_{vp} & x_{vr} \end{bmatrix}^T \tag{4.11}$$

The non-linear state space model is expressed in Equation (4.12) for positive and negative valve openings, i.e. $\mathbf{f}_{v+}(\mathbf{x}_v, \mathbf{u}_v)$ and $\mathbf{f}_{v-}(\mathbf{x}_v, \mathbf{u}_v)$, respectively.

$$\begin{aligned} \mathbf{f}_{v+}(\mathbf{x}_v, \mathbf{u}_v) &= \begin{bmatrix} \frac{1}{M}(p_p \, A_p - p_r \, A_r - F_l) \\ \frac{\beta(p_p^*)}{V_p(x_p^*)}(k_v x_{vp} \sqrt{|p_s - p_p|} \frac{(p_s - p_p)}{|p_s - p_p|} - A_p \, \dot{x}_p) \\ \frac{\beta(p_r^*)}{V_r(x_p^*)}(A_r \, \dot{x}_p - k_v x_{vr} \sqrt{|p_r - p_t|} \frac{(p_r - p_t)}{|p_r - p_t|}) \end{bmatrix} \\ \mathbf{f}_{v-}(\mathbf{x}_v, \mathbf{u}_v) &= \begin{bmatrix} \frac{1}{M}(p_p \, A_p - p_r \, A_r - F_l) \\ \frac{\beta(p_p^*)}{V_p(x_p^*)}(k_v \, |x_{vp}| \, \sqrt{|p_t - p_p|} \frac{(p_t - p_p)}{|p_t - p_p|} - A_p \, \dot{x}_p) \\ \frac{\beta(p_r^*)}{V_r(x_p^*)}(A_r \, \dot{x}_p - k_v \, |x_{vr}| \, \sqrt{|p_r - p_s|} \frac{(p_r - p_s)}{|p_r - p_s|}) \end{bmatrix} \end{aligned} \tag{4.12}$$

The same approach as in Equations (4.5) and (4.6) is used to derive the linear state space model. It should be noted that the supply and tank pressures are assumed constant. The state equation is shown in Equation (4.13).

$$\dot{\mathbf{x}}_v = \underbrace{\begin{bmatrix} 0 & \frac{A_p}{M} & -\frac{A_r}{M} \\ -\frac{\beta_p^* A_p}{V_p^*} & \frac{\beta_p^*}{V_p^*} k_{Q_p,p_p} & 0 \\ \frac{\beta_r^* A_r}{V_r^*} & 0 & -\frac{\beta_r^*}{V_r^*} k_{Q_r,p_r} \end{bmatrix}}_{\mathbf{A}_v} \mathbf{x}_v + \underbrace{\begin{bmatrix} 0 & 0 \\ \frac{\beta_p^*}{V_p^*} k_{Q_p,x_{vp}} & 0 \\ 0 & -\frac{\beta_r^*}{V_r^*} k_{Q_r,x_{vr}} \end{bmatrix}}_{\mathbf{B}_v} \mathbf{u}_v \quad (4.13)$$

The linearisation coefficients, k, change depending on whether the orifice is connected to supply or tank as shown from Equations (4.14) to (4.17), for $p_p^* < p_s$ and $p_r^* < p_s$.

$$k_{Q_p,x_{vp}} = \begin{cases} k_{vp}\sqrt{p_s - p_p^*} & \text{for} \quad (x_v \geq 0) \\ k_{vp}\sqrt{|p_t - p_p^*|} & \text{for} \quad (x_v < 0) \end{cases} \quad (4.14)$$

$$k_{Q_r,x_{vr}} = \begin{cases} k_{vr}\sqrt{p_r^* - p_t} & \text{for} \quad (x_v \geq 0) \\ k_{vr}\sqrt{|p_r^* - p_s|} & \text{for} \quad (x_v < 0) \end{cases} \quad (4.15)$$

$$k_{Q_p,p_p} = \begin{cases} -\frac{x_{vp}^* k_{vp}}{2\sqrt{p_s - p_p^*}} & \text{for} \quad (x_v \geq 0) \\ \frac{x_{vp}^* k_{vp}}{2\sqrt{|p_t - p_p^*|}} & \text{for} \quad (x_v < 0) \end{cases} \quad (4.16)$$

$$k_{Q_r,p_r} = \begin{cases} \frac{x_{vr}^* k_{vr}}{2\sqrt{p_r^* - p_t}} & \text{for} \quad (x_v \geq 0) \\ -\frac{x_{vr}^* k_{vr}}{2\sqrt{|p_r^* - p_s|}} & \text{for} \quad (x_v < 0) \end{cases} \quad (4.17)$$

Output equations for the four combinations with flows as outputs are expressed in Equation (4.18). The remaining matrices with pressures, position, velocity, and acceleration as outputs are not shown.

$$\begin{aligned} \mathbf{y}_{Q_p,P_p} &= \begin{bmatrix} A_p & 0 & 0 \\ 0 & 1 & 0 \end{bmatrix} \mathbf{x}_v & \mathbf{y}_{Q_p,P_r} &= \begin{bmatrix} A_p & 0 & 0 \\ 0 & 0 & 1 \end{bmatrix} \mathbf{x}_v \\ \mathbf{y}_{Q_r,P_p} &= \begin{bmatrix} A_r & 0 & 0 \\ 0 & 1 & 0 \end{bmatrix} \mathbf{x}_v & \mathbf{y}_{Q_r,P_r} &= \begin{bmatrix} A_r & 0 & 0 \\ 0 & 0 & 1 \end{bmatrix} \mathbf{x}_v \end{aligned} \quad (4.18)$$

The state space model with flows as outputs are found in steady state according to Equation 4.18. The compression flow is thereby neglected.

The transfer function matrices, $\mathbf{G}_v$, for each output matrix, $\mathbf{C}$, is found by Equation (4.8). It should be noted that the state model described in this section is used to find transfer functions for all control combinations in Table 3.2 with valve openings as inputs. The linear model block diagram for valves as inputs is shown in Figure 4.2.

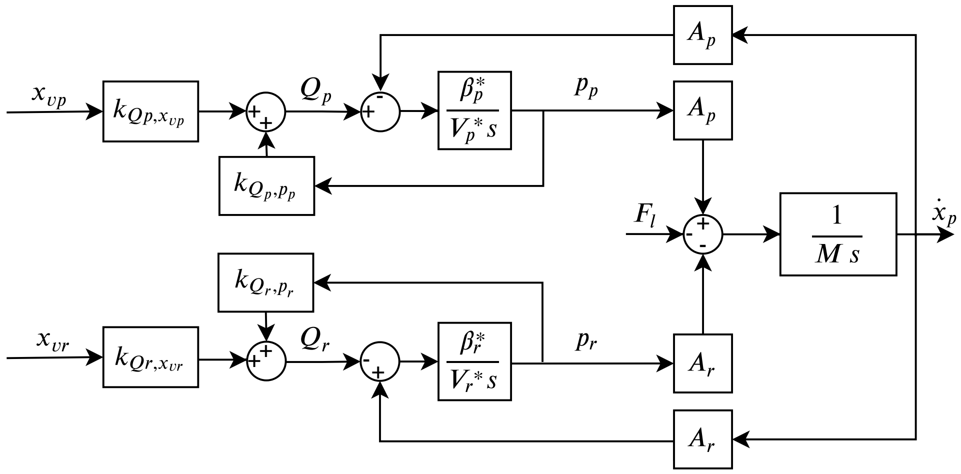

Figure 4.2: Linear model diagram for the model with valve openings as inputs.

4.3 Extended Model with Valve Openings as Inputs

To validate the analytic RGA analysis, a numerical comparison is made with an extended state space model which is derived in this section. It includes the leakage flow and viscous friction, and the piston position is included as a state.

The state vector and input vector are shown in Equation (4.19) where 'v' in the subscript 'v, e' stands for valve as input and 'e' stands for extended state space model. The subscripts are used to distinguish between the three state space models.

$$\mathbf{x}_{v,e} = \begin{bmatrix} x_p & \dot{x}_p & p_p & p_r \end{bmatrix}^T \qquad \mathbf{u}_{v,e} = \begin{bmatrix} x_{vp} & x_{vr} \end{bmatrix}^T \tag{4.19}$$

The non-linear state space model is expressed in Equation (4.20) for positive and negative valve openings, i.e. $\mathbf{f}_{v,e+}(\mathbf{x}_{v,e}, \mathbf{u}_{v,e})$ and $\mathbf{f}_{v,e-}(\mathbf{x}_{v,e}, \mathbf{u}_{v,e})$, respectively.

$$
\mathbf{f}_{v,e+}(\mathbf{x}_{v,e}, \mathbf{u}_{v,e}) = \begin{bmatrix} \dot{x}_p \\ \frac{1}{M}(p_p\, A_p - p_r\, A_r - B\, \dot{x}_p - F_c\, sgn(\dot{x}_p) - F_l) \\ \frac{\beta(p_p)}{V_{p0}+x_p A_p}(k_v x_{vp}\sqrt{|p_s - p_p|}\frac{(p_s-p_p)}{|p_s-p_p|} - C_{le}(p_p - p_r) - A_p\, \dot{x}_p) \\ \frac{\beta(p_r)}{V_{r0}+(L-x_p)A_r}(C_{le}(p_p - p_r) - k_v x_{vr}\sqrt{|p_r - p_t|}\frac{(p_r-p_t)}{|p_r-p_t|} + A_r\, \dot{x}_p) \end{bmatrix}
$$

$$
\mathbf{f}_{v,e-}(\mathbf{x}_{v,e}, \mathbf{u}_{v,e}) = \begin{bmatrix} \dot{x}_p \\ \frac{1}{M}(p_p\, A_p - p_r\, A_r - B\, \dot{x}_p - F_c\, sgn(\dot{x}_p) - F_l) \\ \frac{\beta(p_p)}{V_{p0}+x_p A_p}(k_v\, |x_{vp}|\, \sqrt{|p_t - p_p|}\frac{(p_t-p_p)}{|p_t-p_p|} - C_{le}(p_p - p_r) - A_p\, \dot{x}_p) \\ \frac{\beta(p_r)}{V_{r0}+(L-x_p)A_r}(C_{le}(p_p - p_r) - k_v\, |x_{vr}|\, \sqrt{|p_r - p_s|}\frac{(p_r-p_s)}{|p_r-p_s|} + A_r\, \dot{x}_p) \end{bmatrix} \tag{4.20}
$$

The state equations are shown in Equation (4.21) where the Coulomb friction and load force are seen as disturbances.

$$
\dot{\mathbf{x}}_{v,e} = \underbrace{\begin{bmatrix} 0 & 1 & 0 & 0 \\ 0 & -\frac{B}{M} & \frac{A_p}{M} & -\frac{A_r}{M} \\ k_{\dot{p}_p x_p} & k_{\dot{p}_p \dot{x}_p} & k_{\dot{p}_p p_p} & k_{\dot{p}_p p_r} \\ k_{\dot{p}_r x_p} & k_{\dot{p}_r \dot{x}_p} & k_{\dot{p}_r p_p} & k_{\dot{p}_r p_r} \end{bmatrix}}_{\mathbf{A}_{v,e}} \mathbf{x}_{v,e} + \underbrace{\begin{bmatrix} 0 & 0 \\ 0 & 0 \\ k_{\dot{p}_p x v p} & 0 \\ 0 & k_{\dot{p}_r x v r} \end{bmatrix}}_{\mathbf{B}_{v,e}} \mathbf{u}_{v,e} \tag{4.21}
$$

The extended linear model block diagram is shown in Figure 4.3.

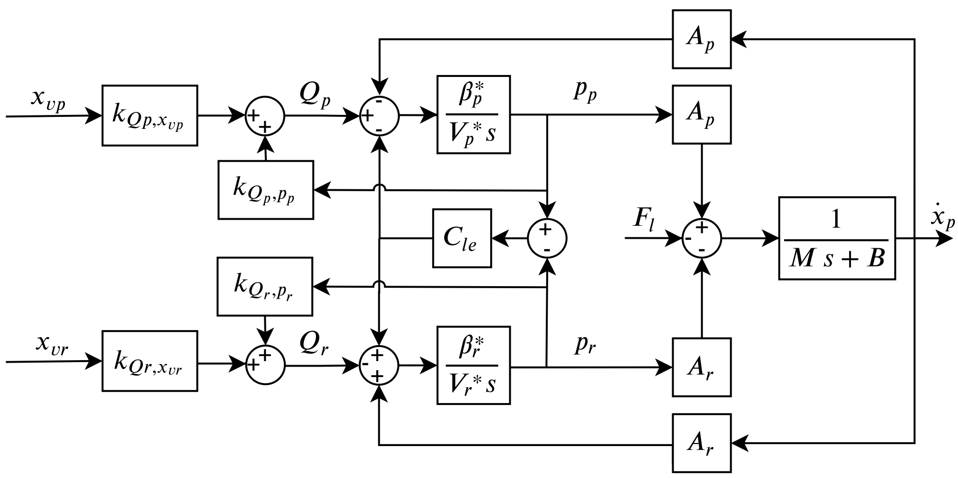

Figure 4.3: Linear model diagram for the extended model.

The transfer function matrix, $\mathbf{G}_{v,e}$, for each output matrix, $\mathbf{C}$, is found by Equation (4.8). The transfer function matrices for each state space model are used to find the cross couplings between the two inputs and two outputs using the Relative Gain Array, RGA, which is described in Chapter 5.

Chapter 5

Relative Gain Array

For a general Multiple-Input Multiple-Output, MIMO, system, multiple outputs may be controlled simultaneously using multiple inputs. System couplings occur in such a system when one arbitrary input interacts with more than one output. The system couplings are analysed with a relative gain array, RGA, analysis in this chapter. A general MIMO system with two inputs, $u(s)$, and two outputs, $y(s)$, is shown in Equations (5.1) and (5.2) where $g(s)$ are entries in the transfer function matrix.

$$y_1(s) = g_{11}(s)\, u_1(s) + g_{12}(s)\, u_2(s) \tag{5.1}$$

$$y_2(s) = g_{21}(s)\, u_1(s) + g_{22}(s)\, u_2(s) \tag{5.2}$$

The cross couplings are illustrated in Figure 5.1 which shows the direct interaction between each input and the two outputs.

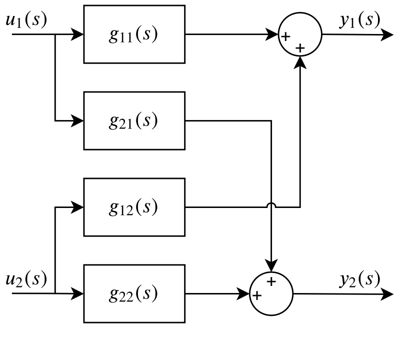

Figure 5.1: MIMO system coupling.

If desired to control $y_1(s)$ using control input $u_1(s)$ two extreme cases can be stated, one is open loop control where $u_2(s) = 0$. This is shown in Equation (5.3) by setting $u_2(s) = 0$ in Equation (5.1).[Skogestad and Postlethwaite, 2005, p. 82-85]

$$u_2(s) = 0: \quad y_1(s) = g_{11}(s)\, u_1(s) \tag{5.3}$$

The other extreme case is perfect closed loop control of the other loop, which implies $y_2(s) = 0$ for a regulator problem as the reference is zero. This yields Equation (5.4) when applied in Equation (5.2).

$$y_2(s) = 0: \quad g_{21}(s)\, u_1(s) + g_{22}(s)\, u_2(s) = 0 \quad \Rightarrow \quad u_2(s) = -\frac{g_{21}(s)}{g_{22}(s)}\, u_1(s) \tag{5.4}$$

which shows the interaction of the two control inputs. Inserting $u_2(s)$ into Equation (5.1) yields Equation (5.5).

$$y_1(s) = \underbrace{\left(g_{11}(s) - \frac{g_{21}(s)}{g_{22}(s)} g_{12}(s)\right)}_{\hat{g}_{11}(s)} u_1(s) \tag{5.5}$$

A relative gain can be defined between the two extreme cases which is shown in Equation (5.6)[Skogestad and Postlethwaite, 2005, p. 84].

$$\frac{g_{11}(s)}{\hat{g}_{11}(s)} = \frac{g_{11}(s)}{g_{11}(s) - \frac{g_{21}(s)}{g_{22}(s)} g_{12}(s)} = \frac{1}{1 - \frac{g_{12}(s)\, g_{21}(s)}{g_{11}(s)\, g_{22}(s)}} = \lambda_{11}(s) \tag{5.6}$$

where $\lambda_{11}(s)$ is the RGA element. The RGA elements for a 2x2 transfer function matrix are calculated in Equation (5.7) where $'\times'$ denotes element-by-element multiplication[Skogestad and Postlethwaite, 2005, p. 82-83].

$$RGA(\mathbf{G}(s)) = \Lambda(\mathbf{G}(s)) \triangleq \mathbf{G}(s) \times \left(\mathbf{G}(s)^{-1}\right)^T \tag{5.7}$$

$$\Lambda(\mathbf{G}(s)) = \begin{bmatrix} \lambda_{11}(s) & \lambda_{12}(s) \\ \lambda_{21}(s) & \lambda_{22}(s) \end{bmatrix} = \begin{bmatrix} \lambda_{11}(s) & 1 - \lambda_{11}(s) \\ 1 - \lambda_{11}(s) & \lambda_{11}(s) \end{bmatrix} \tag{5.8}$$

In Equation (5.8), for a 2x2 transfer function matrix, if $\lambda_{11} = 1$ the MIMO system is perfectly decoupled and can be considered two SISO systems. An RGA element of unit value means the magnitudes of $g_{11}(s)$ and $\hat{g}_{11}(s)$ are equal which can be interpreted as $g_{12}(s) = 0$, and thereby input $u_2(s)$ having no influence on $y_1(s)$ when

$y_1(s)$ is controlled by $u_1(s)$. The same applies for $y_2(s)$ controlled by $u_2(s)$, where $g_{21}(s) = 0$ meaning the input $u_1(s)$ having no influence on $y_2(s)$. The proper input-output SISO pairing would in this case be to control $y_1(s)$ with $u_1(s)$ and $y_2(s)$ with $u_2(s)$. Figure 5.2 depicts the two possible input-output pairing possibilities, a diagonal pairing or an off-diagonal pairing.

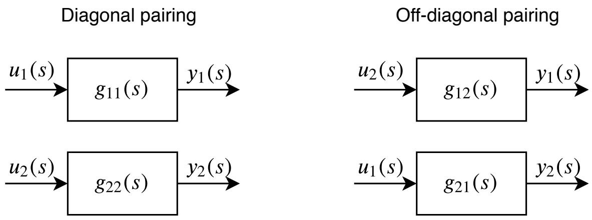

Figure 5.2: SISO systems for a 2x2 transfer function matrix.

In a SISO perspective, for a diagonal pairing, the transfer functions $g_{12}(s)$ and $g_{21}(s)$ can be neglected as these have close to none or no influence on the outputs. For an off-diagonal pairing, the transfer functions $g_{11}(s)$ and $g_{22}(s)$ can be neglected. The RGA analysis is consequently used to find the degree of coupling or even conclude whether the MIMO system is decoupled and can be regarded as a combination of SISO systems.

When calculating the RGA element, it is recommended to rearrange the transfer function matrix $\mathbf{G(s)}$ as either Equation (5.9) or (5.10) to satisfy the following two pairing rules [Skogestad and Postlethwaite, 2005, p. 85]:

1. "Prefer pairings such that the rearranged system, with the selected pairings along the diagonal, has an RGA matrix close to identity at frequencies around the closed-loop bandwidth."
2. "Avoid (if possible) pairing on negative steady state RGA elements."

$$\begin{bmatrix} y_1(s) \\ y_2(s) \end{bmatrix} = \begin{bmatrix} g_{11}(s) & g_{12}(s) \\ g_{21}(s) & g_{22}(s) \end{bmatrix} \begin{bmatrix} u_1(s) \\ u_2(s) \end{bmatrix} \tag{5.9}$$

$$\begin{bmatrix} y_2(s) \\ y_1(s) \end{bmatrix} = \begin{bmatrix} g_{21}(s) & g_{22}(s) \\ g_{11}(s) & g_{12}(s) \end{bmatrix} \begin{bmatrix} u_1(s) \\ u_2(s) \end{bmatrix} \tag{5.10}$$

Pairing rule 1 recommends that if $\mathbf{G}(s)$ is arranged as Equation (5.9), then $|g_{12}(j\omega_b)\, g_{21}(j\omega_b)| < |g_{11}(j\omega_b)\, g_{22}(j\omega_b)|$, which results in an RGA matrix close to identity at the closed-loop bandwidth, ω_b. The relation between the transfer functions and the RGA matrix is seen in Equations (5.6) to (5.8). Pairing rule 2 recommends that if $\mathbf{G}(s)$ is arranged as Equation (5.9), $|g_{12}(0)\, g_{21}(0)| < |g_{11}(0)\, g_{22}(0)|$, which results in positive steady state RGA elements, $0 \leq \lambda_{11}(0) \leq 1$. It should be noted that the inequality signs between the transfer functions are opposite for the arrangement in Equation (5.10).

A set of important properties of the RGA are listed below[Skogestad and Postlethwaite, 2005, p. 88]:

- The rows and columns of the RGA matrix sum to 1
- The RGA elements are independent of the system input-output scaling
- The RGA element is equal to 1 if the transfer function matrix is upper or lower triangular

It follows from the last property that RGA is a measure of two-way interaction[Skogestad and Postlethwaite, 2005, p. 88-89]. That means the relation between $g_{12}(s)$ and $g_{11}(s)$ and the relation between $g_{21}(s)$ and $g_{22}(s)$ are not analysed separately.

Range of the RGA Element

The values that the RGA element, $\lambda_{11}(s)$, can take are analysed to make it easier to determine how heavy the cross couplings are for different values of $\lambda_{11}(s)$. The possible values of $\lambda_{11}(s)$ are found by analysing the relation between $g_{12}(s)g_{21}(s)$ and $g_{11}(s)g_{22}(s)$. The RGA element, λ_{11}, is plotted in Figure 5.3 as a function of $g_{12}g_{21}/g_{11}g_{22} = g_r$ to find the range of the RGA element.

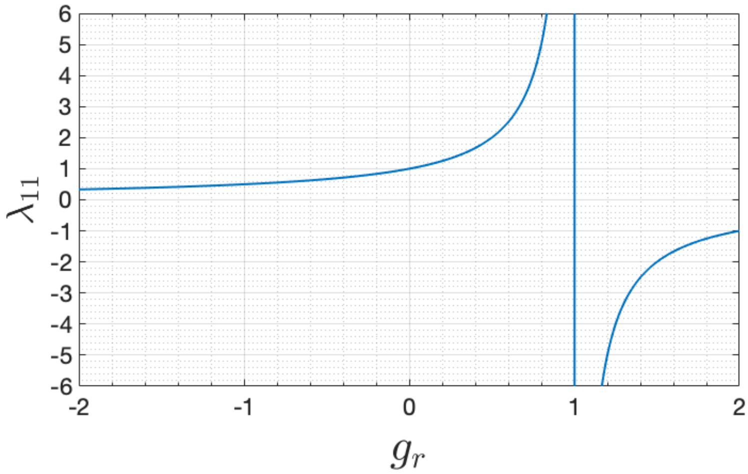

Figure 5.3: λ_{11} as a function of the transfer function ratio.

λ_{11} ranges from $-\infty$ to ∞ but is limited to -6 and 6 in Figure 5.3. The cross couplings are most significant at $\lambda_{11} = 0.5$ and $\lambda_{11} = \infty$ which is where $|g_{12}(s)\, g_{21}(s)| = |g_{11}(s)\, g_{22}(s)|$. If $|g_{12}(s)\, g_{21}(s)| < |g_{11}(s)\, g_{22}(s)|$ and the pairings are arranged as Equation (5.9), it follows that:

$$|g_{12}(s)\, g_{21}(s)| < |g_{11}(s)\, g_{22}(s)| \Leftrightarrow \frac{|g_{12}(s)\, g_{21}(s)|}{|g_{11}(s)\, g_{22}(s)|} < 1 \Leftrightarrow -1 < g_r(s) < 1 \tag{5.11}$$

Equation (5.11) shows that for $|g_{12}(s)\, g_{21}(s)| < |g_{11}(s)\, g_{22}(s)|$ then $g_r(s)$ ranges from -1 and 1. It is seen in Figure 5.3 that λ_{11} varies from 0.5 to ∞ in that range. When $g_r(s) < -1$ or $g_r(s) > 1$ then $|g_{12}(s)\, g_{21}(s)| > |g_{11}(s)\, g_{22}(s)|$ and λ_{11} varies from $-\infty$ to 0.5. As seen in Figure 5.3, λ_{11} is strictly non-linear which makes it harder to determine the degree of coupling for different values of λ_{11}. As an example, the change in coupling is the same for $\lambda_{11} = 0.5$ to $\lambda_{11} = 1$ and for $\lambda_{11} = 1$ to $\lambda_{11} = \infty$. A certain change in λ_{11} between 0.5 and 1 will thereby have a greater effect on the coupling than the same change when $\lambda_{11} > 1$. In the following section, the limitations of the RGA element is analysed.

RGA Limitations

A limitation of the RGA analysis occurs for RGA elements having a real and imaginary part. To accommodate the imaginary part which arises from substituting s by $j\omega$, the absolute value of the RGA element can be computed. However, the absolute value of the RGA element can result in misinterpretation of the system couplings as shown in Figure 5.4. The gray domain shows values satisfying $|g_{12}(s)\, g_{21}(s)| < |g_{11}(s)\, g_{22}(s)|$ and for λ_{11}'s outside this domain, the diagonal and off-diagonal elements of the transfer function matrix should be swapped, i.e. either Equation (5.9) or Equation (5.10).

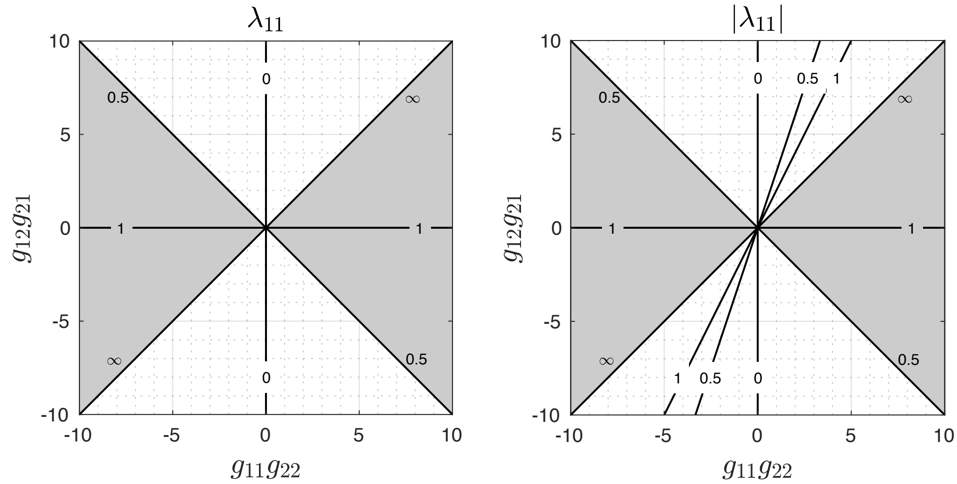

Figure 5.4: The value and absolute value of the RGA element. The grey domain shows values satisfying: $|g_{12}(s)\, g_{21}(s)| < |g_{11}(s)\, g_{22}(s)|$.

The contours of Figure 5.4 show the value, left plot, and the absolute value, right plot, of the diagonal RGA element as a function of the real part of $g_{12}\, g_{21}$ and $g_{11}\, g_{22}$ with no imaginary part. For RGA elements of -1, the corresponding absolute value of 1 can be misinterpreted as perfectly decoupled even though it is coupled and for RGA elements of -0.5, the corresponding absolute value of 0.5 can be misinterpreted as heavily coupled. This happens if the sign of $g_{12}\, g_{21}$ and $g_{11}\, g_{22}$ are equal which is in the first and third quadrant of the right plot in Figure 5.4. It is difficult to determine the sign of the transfer functions as the change in phase as frequency increases can change the sign of the real and imaginary part of λ_{11}. Furthermore, the sign convention when modelling the physical system may change the sign of the transfer functions. The absolute function is not reversible which makes it hard to determine the coupling by looking at $|\lambda_{11}|$.

In conclusion, if the RGA element contains no imaginary part, it is not recommended to compute the absolute value. If the RGA element contains an imaginary part, calculating the absolute value is a possibility, but it can be misleading as the sign of λ_{11} cannot be determined.

5.1 Relative Gain Notation

The notation used throughout the following sections will be defined in this section. The output combinations where the states can be controlled highly independently found in Chapter 3 are repeated in the table below.

	Q_p	Q_r	x_p	$\dot{x}_p$	$\ddot{x}_p$
p_p	✓[1]	✓[3]	✓[5]	✓[7]	✓[9]
p_r	✓[2]	✓[4]	✓[6]	✓[8]	✓[10]

Table 5.1: Highly independent control combinations.

State space models were derived with flows and valve openings as inputs in Section 4.1 and Section 4.2, respectively. From Table 5.1 it is seen that transfer functions for combinations $5 - 10$ can be found for both flows and valve openings as inputs, whereas transfer functions for combinations $1 - 4$ are found for valve openings as inputs.

The relations between transfer functions with x_{vp} as input and five of the outputs from Table 5.1 are shown in Equation (5.12). The same relations are valid for x_{vr}, Q_p, and Q_r as inputs instead of x_{vp}.

$$
\begin{aligned}
\frac{x_p(s)}{x_{vp}(s)} &= g_{x_p x_{vp}}(s) \\
\frac{\dot{x}_p(s)}{x_{vp}(s)} &= g_{\dot{x}_p x_{vp}}(s) = g_{x_p x_{vp}}(s)\, s \\
\frac{\ddot{x}_p(s)}{x_{vp}(s)} &= g_{\ddot{x}_p x_{vp}}(s) = g_{x_p x_{vp}}(s)\, s^2 \\
\frac{Q_p(s)}{x_{vp}(s)} &= g_{Q_p x_{vp}}(s) = g_{x_p x_{vp}}(s)\, A_p\, s \\
\frac{Q_r(s)}{x_{vp}(s)} &= g_{Q_r x_{vp}}(s) = g_{x_p x_{vp}}(s)\, A_r\, s
\end{aligned}
\tag{5.12}
$$

In Equation (5.12) the transfer function $g_{x_p x_{vp}}(s)$ is marked with red to show how it is related to the other transfer functions, where it is seen that they are closely related. The transfer function matrix where $u_1 = x_{vp}$, $u_2 = x_{vr}$, $y_1 = p_p$, and $y_2 = \dot{x}_p$ is found using Equation (4.8) and the structure is shown in Equation (5.13).

$$\begin{bmatrix} p_p(s) \\ \dot{x}_p(s) \end{bmatrix} = \begin{bmatrix} g_{p_p x_{vp}}(s) & g_{p_p x_{vr}}(s) \\ g_{\dot{x}_p x_{vp}}(s) & g_{\dot{x}_p x_{vr}}(s) \end{bmatrix} \begin{bmatrix} x_{vp}(s) \\ x_{vr}(s) \end{bmatrix} = \begin{bmatrix} g_{p_p x_{vp}}(s) & g_{p_p x_{vr}}(s) \\ s\, g_{x_p x_{vp}}(s) & s\, g_{x_p x_{vr}}(s) \end{bmatrix} \begin{bmatrix} x_{vp}(s) \\ x_{vr}(s) \end{bmatrix} \tag{5.13}$$

The relative gain for $y_1 = p_p$ and $y_2 = \dot{x}_p$, $\lambda_{p_p \dot{x}_p}$, is found using Equation (5.6) and expressed in Equation (5.14). The relative gain is a function of frequency, however, (s) is omitted for simplicity.

$$\lambda_{p_p \dot{x}_p} = \frac{1}{1 - \frac{g_{p_p Q_r}(s)\, g_{\dot{x}_p Q_p}(s)}{g_{p_p Q_p}(s)\, g_{\dot{x}_p Q_r}(s)}} = \frac{1}{1 - \frac{g_{p_p Q_r}(s)\, g_{x_p Q_p}(s)}{g_{p_p Q_p}(s)\, g_{x_p Q_r}(s)} \frac{s}{s}} = \lambda_{p_p x_p} \tag{5.14}$$

It is seen in Equation (5.14) that s is present in both the numerator and denominator and cancels out. That means the relative gain for p_p and $\dot{x}_p$ as outputs is equal to the relative gain for p_p and x_p as outputs. The same is valid for acceleration as output where 's^2' cancels out, and for each of the flows as output where either '$A_p\, s$' or '$A_r\, s$' cancel out due to the relations in Equation (5.12).

That means the relative gains are equal when piston side pressure is the first output and either piston position, velocity, acceleration or one of the flows is the other output when valve openings are inputs. The same is valid for rod side pressure instead of piston side pressure. The same is also valid for flows as inputs. That gives four different relative gains; two for valve openings as inputs and two for flows as inputs.

Valve openings as inputs:

- Piston side pressure and one of the other outputs
- Rod side pressure and one of the other outputs

Flows as inputs:

- Piston side pressure and one of the other outputs
- Rod side pressure and one of the other outputs

The relative gains are further divided into diagonal and off-diagonal pairing. The relative gains are denoted such that the superscript refers to either the diagonal, i.e. λ^d, or off-diagonal, i.e. λ^o. That means whether the pairing is on the diagonal or the off-diagonal of the transfer function matrix. *The transfer function matrices are always paired such that the first output is either p_p or p_r and the second output is either x_p, $\dot{x}_p$, $\ddot{x}_p$, Q_p, or Q_r.* An example is given below:

$$\begin{bmatrix} p_p(s) \\ x_p(s) \end{bmatrix} = \begin{bmatrix} g_{p_p,x_{vp}}(s) & g_{p_p,x_{vr}}(s) \\ g_{x_p,x_{vp}}(s) & g_{x_p,x_{vr}}(s) \end{bmatrix} \begin{bmatrix} x_{vp}(s) \\ x_{vr}(s) \end{bmatrix} \tag{5.15}$$

Where the diagonal pairing is p_p/x_{vp} and x_p/x_{vr}. *The RGA analysis is based on the diagonal pairing of the transfer function matrix, and y_1 and y_2 are swapped if desired to pair the off-diagonal.*

The subscript of the relative gains refers to the subscript of the pressure and the inputs, where p is piston side pressure, r is the rod side pressure, f is for flows as inputs, and v is for valve openings as inputs. An example of piston side pressure and one of the other outputs where flows are inputs is 'p, f'. The relative gains when pairing the diagonal are shown in Table 5.2.

<table>
<tr><td rowspan="2">$u_1 = Q_p$
$u_2 = Q_r$</td><td>p_p</td><td colspan="2">-</td><td colspan="3">$\lambda^d_{p,f}$</td></tr>
<tr><td>p_r</td><td colspan="2">-</td><td colspan="3">$\lambda^d_{r,f}$</td></tr>
<tr><td rowspan="2">$u_1 = x_{vp}$
$u_2 = x_{vr}$</td><td>p_p</td><td colspan="5">$\lambda^d_{p,v}$</td></tr>
<tr><td>p_r</td><td colspan="5">$\lambda^d_{r,v}$</td></tr>
<tr><td></td><td>y_1 / y_2</td><td>Q_p</td><td>Q_r</td><td>x_p</td><td>$\dot{x}_p$</td><td>$\ddot{x}_p$</td></tr>
</table>

Table 5.2: Relative gains when pairing the diagonal.

The relative gains when pairing the off-diagonal are shown in Table 5.3.

<table>
<tr><td rowspan="2">$u_1 = Q_p$
$u_2 = Q_r$</td><td>p_p</td><td colspan="2">-</td><td colspan="3">$\lambda^o_{p,f}$</td></tr>
<tr><td>p_r</td><td colspan="2">-</td><td colspan="3">$\lambda^o_{r,f}$</td></tr>
<tr><td rowspan="2">$u_1 = x_{vp}$
$u_2 = x_{vr}$</td><td>p_p</td><td colspan="5">$\lambda^o_{p,v}$</td></tr>
<tr><td>p_r</td><td colspan="5">$\lambda^o_{r,v}$</td></tr>
<tr><td></td><td>y_2 / y_1</td><td>Q_p</td><td>Q_r</td><td>x_p</td><td>$\dot{x}_p$</td><td>$\ddot{x}_p$</td></tr>
</table>

Table 5.3: Relative gains when pairing the off-diagonal.

In Tables 5.2 and 5.3, the first two rows are when flows are inputs and the following two rows are when valve openings are inputs. Rows marked with grey are for piston side pressure as output and the remaining rows are for rod side pressure as output. Columns refer to the other output with the corresponding output written in the bottom row. It should be noted that for diagonal pairing in Table 5.2 the first output is one of the pressures, and for off-diagonal pairing in Table 5.3 the second output is one of the pressures, i.e. the outputs are swapped.

The subscript, 'e', is further added when using the extended state space model which was derived in Section 4.3. An example is $\lambda^d_{r,v,e}$ where the first output is rod side pressure and the inputs are valve openings.

The cross couplings will be analysed for the systems with flows as inputs and with valve openings as inputs in Section 5.2 and Section 5.3, respectively.

5.2 Couplings with Flows as Inputs

The cross couplings with flows as inputs are analysed in this section. The analysis is based on piston side pressure as one of the outputs throughout the section and the conclusions for the rod side pressure as one of the outputs is written by the end of the section. The system inputs are piston and rod side flows, Q_p and Q_r.

The relative gain, $\lambda^d_{p,f}$, is found by the approach described in Equation (5.6) and expressed in Equation (5.16).

$$\lambda^d_{p,f} = \frac{V_p\,V_r\,M\,s^2 + A_r^2\,\beta_r\,V_p}{V_p\,V_r\,M\,s^2 + A_r^2\,\beta_r\,V_p + A_p^2\,\beta_p\,V_r} \tag{5.16}$$

The expression for $\lambda^d_{p,f}$ is derived in Appendix B.1. The relative gain, $\lambda^o_{p,f}$, when pairing the off-diagonal is expressed in Equation (5.17), where it should be noted that $\lambda^o_{p,f} = 1 - \lambda^d_{p,f}$.

$$\lambda^o_{p,f} = \frac{A_p^2\,\beta_p\,V_r}{V_p\,V_r\,M\,s^2 + A_r^2\,\beta_r\,V_p + A_p^2\,\beta_p\,V_r} \tag{5.17}$$

The relative gain, $\lambda^d_{p,f}$, from Equation (5.16) is rewritten to the inequality expressed in Equation (5.18), which should be satisfied to get the gain as close to 1 as possible, since $\lambda^d_{p,f} = 1$ for a perfectly decoupled system.

$$\begin{aligned}
&|A_p^2\,\beta_p\,V_r| \ll |V_p\,V_r\,M\,s^2 + A_r^2\,\beta_r\,V_p| \\
&\Updownarrow \\
&|A_p^2\,\beta_p| \ll \left|V_p\,M\,s^2 + A_r^2\,\beta_r\,\frac{V_p}{V_r}\right|
\end{aligned} \tag{5.18}$$

The volumes, $V_p = x_p\,A_p$ and $V_r = (L - x_p)\,A_r$, are substituted into Equation (5.18), where the dead volumes, V_{p0} and V_{r0}, are neglected for simplicity. These are included in the numerical RGA analysis in Section 5.5 to check whether they have an impact on the couplings.

$$
\begin{aligned}
\lambda^d_{p,f} \approx 1: \qquad & |A_p^2\,\beta_p| \ll \left| x_p\,A_p\,M\,s^2 + A_r^2\,\beta_r\,\frac{x_p\,A_p}{(L-x_p)\,A_r}\right| \\
& \Updownarrow \\
& 1 \ll \left| \frac{x_p\,M}{A_p\,\beta_p}\,s^2 + \frac{\beta_r}{\beta_p}\,\frac{A_r}{A_p}\,\frac{x_p}{L-x_p}\right|
\end{aligned}
\tag{5.19}
$$

The inequality is opposite if the off-diagonal is paired instead as shown in Equation (5.20).

$$
\begin{aligned}
\lambda^o_{p,f} \approx 1: \qquad & |A_p^2\,\beta_p| \gg \left| x_p\,A_p\,M\,s^2 + A_r^2\,\beta_r\,\frac{x_p\,A_p}{(L-x_p)\,A_r}\right| \\
& \Updownarrow \\
& 1 \gg \left| \frac{x_p\,M}{A_p\,\beta_p}\,s^2 + \frac{\beta_r}{\beta_p}\,\frac{A_r}{A_p}\,\frac{x_p}{L-x_p}\right|
\end{aligned}
\tag{5.20}
$$

The relative gains in Equations (5.19) and (5.20) are evaluated in relevant frequencies throughout the section.

5.2.1 Low Frequency Range

The relative gains are evaluated in the low frequency range by letting $s \to 0$. The simplified expressions are shown in Equations (5.21) and (5.22), where $\gamma = \beta_r/\beta_p$, $\alpha = A_r/A_p$, and $\epsilon = x_p/(L-x_p)$.

$$
\lambda^d_{p,f} \approx 1: \qquad 1 \ll \left| \frac{\beta_r}{\beta_p}\,\frac{A_r}{A_p}\,\frac{x_p}{L-x_p}\right| = |\gamma\,\alpha\,\epsilon| \tag{5.21}
$$

$$
\lambda^o_{p,f} \approx 1: \qquad 1 \gg \left| \frac{\beta_r}{\beta_p}\,\frac{A_r}{A_p}\,\frac{x_p}{L-x_p}\right| = |\gamma\,\alpha\,\epsilon| \tag{5.22}
$$

One parameter at a time is varied and the effect on the relative gain is studied. As $x_p \to L$, ϵ increases which means the right hand side, RHS, of Equations (5.21) and (5.22) increases. If instead $x_p \to 0$, ϵ decreases and the RHS decreases. The bulk modulus is related to pressure: as p_p increases, β_p increases, and as p_r increases,

β_r increases. If the bulk modulus ratio, γ, increases, the RHS of Equations (5.21) and (5.22) increases. If instead γ decreases, the RHS decreases. Finally, the area relation, α, is varied. As α increases, the RHS increases and as α decreases, the RHS decreases.

Based on the above observations for low frequencies, couplings are less significant for the diagonal pairing when $p_r > p_p$, $x_p \to L$, and $A_r/A_p = 1$, and couplings are less significant for the off-diagonal pairing when $p_r < p_p$, $x_p \to 0$, and A_r/A_p is as low as possible. It is, however, not obvious from Equations (5.21) and (5.22) which impact the pressures have on the couplings compared to piston position and area ratio. How each of the variables of Equation (5.21) affects the couplings compared to each other is analysed by choosing ranges of values for each variable.

It is decided to set a limit on the effective bulk modulus to 50 [%] of the oil bulk modulus to keep a certain oil stiffness. The effective bulk modulus is limited to 7000 [bar] for an oil bulk modulus of 14000 [bar] which is 50 [%][Pedersen et al., 2010, p. 148]. The range of the bulk modulus ratio, γ, is shown in Equation (5.23).

$$0.5 \leq \gamma \leq 2 \tag{5.23}$$

The area ratio, α, is varied from 0.4 to 1 such that the analysis is valid for both differential and symmetric cylinders. The range is based on data from a hydraulic cylinder supplier where the area ratios range from 0.5 to 0.88[TAON, 2020]. The range of the area ratio is shown in Equation (5.24).

$$0.4 \leq \alpha \leq 1 \tag{5.24}$$

The piston position is varied from 5 [%] to 95 [%] of full stroke length where the range of the ratio, ϵ, is shown in Equation (5.25). That corresponds to a dead volume of 5 [%] in each end of the cylinder.

$$0.05 \leq \epsilon \leq 19 \tag{5.25}$$

Two contour plots are shown in Figure 5.5 where the bulk modulus ratio, γ, is varied on the x-axis and the piston position, x_p, is varied from 5 [%] to 95 [%] of stroke length on the y-axis. The contour levels show the value of the RHS of Equations (5.21) and (5.22). The left plot is for $\alpha = 0.4$ and the right plot is for $\alpha = 1$, which are the chosen lower and upper limits for the area ratio.

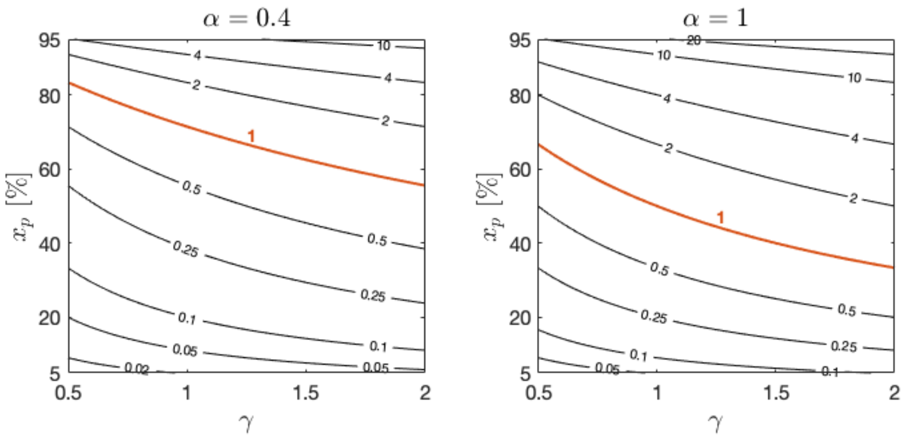

Figure 5.5: The contour lines are the values of the RHS of Equations (5.21) and (5.22). At the red line the RHS equals 1.

Figure 5.5 is used to determine for which combinations of x_p, γ, and α that will result in RHS of Equations (5.21) and (5.22) significantly larger or less than 1. Equation (5.21) is satisfied for large values of the contour levels above the red line and the inputs and outputs must be parred through the diagonal. Equation (5.22) is satisfied for small values of the contour levels below the red line and the inputs and outputs must be parred through the off-diagonal. The higher or lower the values of the contour levels are compared to 1, the less the cross couplings.

A factor of minimum 4 between the RHS and LHS of Equations (5.21) and (5.22) is arbitrarily chosen to keep the cross couplings low. A factor of 4 corresponds to $\lambda = 0.8$ which is deemed close enough to 1 for the cross couplings to be less significant. This suggests a diagonal pairing for contour values greater than 4 and an off-diagonal pairing for values below 0.25. This factor is used throughout the section to determine when each pairing should be used. For off-diagonal pairing, the piston position should be kept below approximately 30 [%] of the cylinder stroke length when $\alpha = 0.4$ and as α increases to 1, the piston position should be kept below approximately 15 [%] of the cylinder stroke length. For diagonal pairing, the piston position should be kept at 95 [%] of the cylinder stroke length when $\alpha = 0.4$ and as α increases to 1, the piston position should be kept above approximately 90 [%] of the cylinder stroke length.

Figure 5.5 shows that coupling at low frequencies is more dependent on x_p than γ and α. By changing x_p from 5[%] to 95[%], the parring of inputs and outputs must change which is true for any combination of α and γ. This is not true for changing α or γ from minimum to maximum for any combination with x_p. *It is concluded that for low frequencies the parring of inputs and outputs must change for any combination of α and γ when varying x_p from 5[%] to 95[%].*

5.2.2 Transition Frequency Range

The low frequency range has now been analysed and the transition region is studied in this section. The frequency dependent inequalities are repeated in Equations (5.26) and (5.27) where s is substituted by $j\omega$.

$$\lambda^d_{p,f} \approx 1: \qquad 1 \ll \left| -\frac{x_p\, M}{A_p\, \beta_p}\, \omega^2 + \frac{\beta_r}{\beta_p}\, \frac{A_r}{A_p}\, \frac{x_p}{(L - x_p)} \right| \tag{5.26}$$

$$\lambda^o_{p,f} \approx 1: \qquad 1 \gg \left| -\frac{x_p\, M}{A_p\, \beta_p}\, \omega^2 + \frac{\beta_r}{\beta_p}\, \frac{A_r}{A_p}\, \frac{x_p}{(L - x_p)} \right| \tag{5.27}$$

As the frequency, ω, increases from 0, the absolute value of the RHS of Equations (5.26) and (5.27) decrease until a certain frequency, ω_w, where the RHS equals 0 as seen in Equation (5.28).

$$-\frac{x_p\, M}{A_p\, \beta_p}\, \omega_w^2 + \frac{\beta_r}{\beta_p}\, \frac{A_r}{A_p}\, \frac{x_p}{(L - x_p)} = 0 \tag{5.28}$$

For the frequency, ω_w, Equation (5.27) is satisfied and $\lambda^o_{p,f} = 1$ which means the system is fully decoupled when pairing the off-diagonal. The frequency is expressed in Equation (5.29).

$$\omega_w = \sqrt{\frac{\beta_r}{\beta_p}\, \frac{A_r}{A_p}\, \frac{x_p}{(L - x_p)}\, \frac{A_p\, \beta_p}{x_p\, M}} = \sqrt{\frac{A_r\, \beta_r}{M\,(L - x_p)}} \tag{5.29}$$

The frequency, ω_w, is compared to the natural frequency of the system to check whether they are related. The natural frequency, ω_n, is found by evaluating one of the transfer functions.

$$g_{x_p Q_p}(s) = \frac{A_p\, \beta_p\, V_r}{s\,(M\, V_p\, V_r\, s^2 + A_p^2\, \beta_p\, V_r + A_r^2\, \beta_r\, V_p)} \tag{5.30}$$

The transfer function, $g_{x_p Q_p}(s)$, consists of an integrator and a second order system from which the natural frequency is found and expressed in Equation (5.31). The volumes are substituted and the derivation of all frequencies of interest can be found in Appendix B.1.1.

$$\omega_n = \sqrt{\frac{A_p^2\,\beta_p\,V_r + A_r^2\,\beta_r\,V_p}{M\,V_p\,V_r}} = \sqrt{\frac{A_p\,\beta_p}{M\,x_p} + \omega_w^2} \tag{5.31}$$

It is then possible to express the frequency ω_w as a function of ω_n as shown in Equation (5.32).

$$\omega_w = \sqrt{\omega_n^2 - \frac{A_p\,\beta_p}{M\,x_p}} \tag{5.32}$$

It is seen from Equation (5.32) that the frequency ω_w depends on ω_n. As β_r and A_r increase, both frequencies increase, and as β_p and A_p increase, ω_n increases whereas ω_w is unaffected.

It is desired to work in the frequency range up to the natural frequency and from Equation (5.32) it is seen that ω_n is larger than ω_w. *It is concluded that $\lambda_{p,f}^o = 1$ at the frequency ω_w which is lower than the natural frequency.*

5.2.3 Coupled Frequencies and High Frequencies

The frequencies, ω_c and ω_p, at which the cross couplings are most significant is when $\lambda_{p,f}^d = 0.5$ and $\lambda_{p,f}^d \to \infty$. ω_c is found by setting $\lambda_{p,f}^d$ equal to a constant K which is substituted by 0.5 afterwards. It should be noted that $\lambda_{p,f}^d$ and $\lambda_{p,f}^o$ cross, i.e. $\lambda_{p,f}^d = \lambda_{p,f}^o = 0.5$, at the frequency ω_c.

$$\begin{aligned}\lambda_{p,f}^d &= \frac{-V_p\,V_r\,M\,\omega_c^2 + A_r^2\,\beta_r\,V_p}{-V_p\,V_r\,M\,\omega_c^2 + A_r^2\,\beta_r\,V_p + A_p^2\,\beta_p\,V_r} = K \\ &\Updownarrow \\ \omega_c &= \sqrt{\frac{K\,A_p^2\,\beta_p\,V_r + (K-1)\,A_r^2\,\beta_r\,V_p}{(K-1)\,V_p\,V_r\,M}}\end{aligned} \tag{5.33}$$

The constant K is then substituted by 0.5. It should be noted that the frequency has to be real and positive, and for that reason, only positive solutions are shown in Equation (5.34). For the frequency to be real, what is inside the square root in Equation (5.34) has to be positive. The derivation can be found in Appendix B.1.1.

$$\omega_c = \sqrt{\frac{0.5\,A_p^2\,\beta_p\,V_r - 0.5\,A_r^2\,\beta_r\,V_p}{-0.5\,V_p\,V_r\,M}} = \sqrt{\frac{A_r\,\beta_r}{M\,(L-x_p)} - \frac{A_p\,\beta_p}{M\,x_p}} \tag{5.34}$$

All parameters in Equation (5.34) are positive. There is a positive and a negative fraction in Equation (5.34), which means ω_c is only real if the following is satisfied:

$$\frac{A_p\,\beta_p}{x_p\,M} \leq \frac{A_r\,\beta_r}{(L - x_p)\,M} \qquad \Rightarrow \qquad 1 \leq \alpha\gamma\epsilon \tag{5.35}$$

To find the frequency ω_p at which $\lambda^d_{p,f}$ peaks, i.e. $\lambda^d_{p,f} \to \infty$, the relative gain is reformulated in Equation (5.36) and s is substituted by $j\,\omega_p$.

$$\lambda^d_{p,f} = \frac{1}{1 + \frac{A_p^2\,\beta_p\,V_r}{V_p\,V_r\,M\,s^2 + A_r^2\,\beta_r\,V_p}} = \frac{1}{1 + \frac{A_p^2\,\beta_p\,V_r}{-V_p\,V_r\,M\,\omega_p^2 + A_r^2\,\beta_r\,V_p}} \tag{5.36}$$

It is seen that the denominator in Equation (5.36) should equal 0 for $\lambda^d_{p,f} \to \infty$ which happens when:

$$\frac{A_p^2\,\beta_p\,V_r}{-V_p\,V_r\,M\,\omega_p^2 + A_r^2\,\beta_r\,V_p} = -1 \tag{5.37}$$

The positive frequency, ω_p, at which that happens is found in Equation (5.38).

$$\omega_p = \sqrt{\frac{A_p^2\,\beta_p\,V_r + A_r^2\,\beta_r\,V_p}{V_p\,V_r\,M}} = \sqrt{\frac{A_p\,\beta_p}{M\,x_p} + \frac{A_r\,\beta_r}{M\,(L - x_p)}} = \omega_n \tag{5.38}$$

It is seen from Equation (5.38) that the frequency ω_p is equal to the frequency ω_n. The same is valid for the peak of $\lambda^o_{p,f}$ which is derived in Equation (B.11).

It is concluded that heavy cross couplings occur at the frequency ω_c expressed in Equation (5.34) if Equation (5.35) is satisfied. Furthermore, heavy cross couplings occur at the natural frequency, ω_n, where $\lambda^d_{p,f} \to \infty$. Finally, it should be noted that $\lambda^d_{p,f} \to 1$ and $\lambda^o_{p,f} \to 0$ as $s \to \infty$, i.e. when the frequency approaches infinity.

5.2.4 Conclusion for Piston Side Pressure

The cross couplings when the piston side pressure is one of the outputs were analysed by evaluating the relative gain, $\lambda^d_{p,f}$ at several frequencies. It is found that all frequencies are a combination of the two terms, T_1 and T_2, as shown in Equation

(5.39). It should be noted that ω_c is only defined for $T_2 \leq T_1$ which was stated in Equation (5.35).

$$T_1 = \frac{A_r\,\beta_r}{M\,(L - x_p)}, \qquad T_2 = \frac{A_p\,\beta_p}{M\,x_p}$$

$$\begin{aligned} \omega_c &= \sqrt{T_1 - T_2} \qquad \mathit{for} \qquad T_2 \leq T_1 \Rightarrow 1 \leq \alpha\gamma\epsilon \\ \omega_w &= \sqrt{T_1} \\ \omega_p &= \sqrt{T_1 + T_2} = \omega_n \end{aligned} \tag{5.39}$$

From Equation (5.39) it is seen that $\omega_c < \omega_w < \omega_p$. The known values of $\lambda^d_{p,f}$ and $\lambda^o_{p,f}$ are shown in Figure 5.6 for each of the frequencies starting from the lowest frequency to the left. The distances between the points in Figure 5.6 are arbitrary.

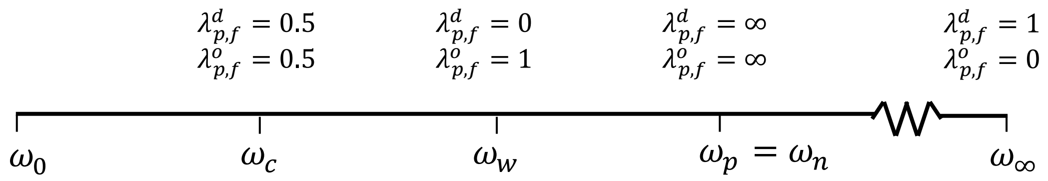

Figure 5.6: Values of $\lambda^d_{p,f}$ and $\lambda^o_{p,f}$ for each frequency.

The above analyses, summed in Figure 5.6, showed that $\lambda^o_{p,f} = 1$ at a frequency, ω_w, i.e. there are no cross couplings when pairing the off-diagonal. To keep the cross couplings low for frequencies below ω_w when pairing the off-diagonal, the piston position should be kept below approximately 30 [%] of the cylinder stroke length when $\alpha = 0.4$ and as α increases to 1, the piston position should be kept below approximately 15 [%] of the cylinder stroke length. This is based on minimum a factor of 4 in Figure 5.5. These piston positions result in $|\alpha\gamma\epsilon| < 1$ which means $\lambda^d_{p,f}$ and $\lambda^o_{p,f}$ do not cross at ω_c due to the inequality stated in Equation (5.35). Instead, the cross couplings become significant at frequency ω_p. In order to avoid working at the frequency ω_p, SISO controllers should be designed such that the closed loop bandwidth is below ω_p.

It is concluded, that to keep the cross couplings low when pairing the off-diagonal, the piston working range is very limited. Furthermore, controllers should be designed such that the bandwidth limits the frequency range to avoid cross couplings. Instead, it is suggested to design a decoupling pre-compensator or MIMO controllers to be able to use the full piston working range and to be able to design a closed loop system with a higher bandwidth.

5.2.5 Conclusion for Rod Side Pressure

The relative gain, $\lambda^d_{r,f}$, when the rod side pressure is one of the outputs is expressed in Equation (5.40) for diagonal pairing.

$$\lambda^d_{r,f} = \frac{A_r^2\,\beta_r\,V_p}{V_p\,V_r\,M\,s^2 + A_p^2\,\beta_p\,V_r + A_r^2\,\beta_r\,V_p} \tag{5.40}$$

The relative gain, $\lambda^o_{r,f}$, when pairing the off-diagonal is expressed in Equation (5.41).

$$\lambda^o_{r,f} = \frac{V_p\,V_r\,M\,s^2 + A_p^2\,\beta_p\,V_r}{V_p\,V_r\,M\,s^2 + A_p^2\,\beta_p\,V_r + A_r^2\,\beta_r\,V_p} \tag{5.41}$$

The cross couplings when rod side pressure is one of the outputs are analysed at several frequencies. All calculations can be found in Appendix B.2. It is found that all frequencies again are a combination of the two terms, T_1 and T_2, as shown in Equation (5.42). It should be noted that ω_c is only defined for $T_1 \leq T_2$ which is stated in Equation (B.27).

$$T_1 = \frac{A_r\,\beta_r}{M\,(L - x_p)}, \qquad T_2 = \frac{A_p\,\beta_p}{M\,x_p}$$

$$\begin{aligned} \omega_c &= \sqrt{T_2 - T_1} \qquad \mathit{for} \qquad T_2 \geq T_1 \Rightarrow 1 \geq \alpha\gamma\epsilon \\ \omega_w &= \sqrt{T_2} \\ \omega_p &= \sqrt{T_2 + T_1} = \omega_n \end{aligned} \tag{5.42}$$

From Equation (5.42) it is seen that $\omega_c < \omega_w < \omega_p$. The known values of $\lambda^d_{r,f}$ and $\lambda^o_{r,f}$ are shown in Figure 5.7 for each of the frequencies starting from the lowest frequency to the left.

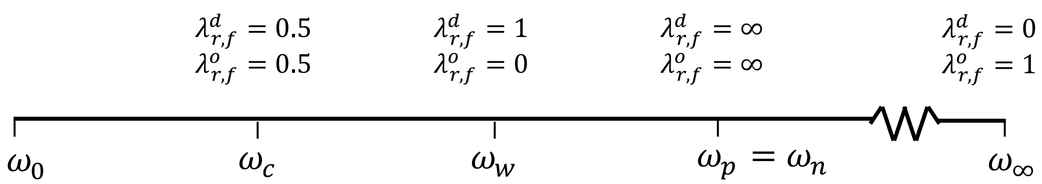

Figure 5.7: Values of $\lambda^d_{r,f}$ and $\lambda^o_{r,f}$ for each frequency.

The analyses showed that $\lambda^d_{r,f} = 1$ at a frequency, ω_w, i.e. there are no cross couplings when pairing the diagonal. To keep the cross couplings low for frequencies below ω_w when pairing the diagonal, the piston position should be kept at 95 [%] of the cylinder stroke length when $\alpha = 0.4$ and as α increases to 1, the piston position should be kept above approximately 90 [%] of the cylinder stroke length. This is based on minimum a factor of 4 in Figure 5.5. These piston positions result in $|\alpha\gamma\epsilon| > 1$ which means $\lambda^d_{r,f}$ and $\lambda^o_{r,f}$ do not cross at ω_c due to the inequality stated in Equation (B.27). However, the working range is very limited and for $\alpha = 0.4$ the piston cannot move without the cross couplings becoming significant.

It is concluded that to keep the cross couplings low when pairing the diagonal, the piston working range is very limited. Instead, it is suggested to design a decoupling pre-compensator or MIMO controllers to be able to use the full piston working range.

5.3 Couplings with Valve Openings as Inputs

In this section, the couplings are analysed for all control combinations in Table 3.2 with valve openings as input. The analysis is initially based on the piston side pressure. The system inputs are piston and rod side valve openings, x_{vp} and x_{rp}.

The RGA-element for the diagonal pairing is shown in Equation (5.43). The expression is derived in Appendix B.3.

$$\lambda_{p,v}^{d} = -\frac{\left(\beta_p k_{Q_p,p_p} - V_p s\right)\left(\beta_r M k_{Q_r,p_r} s + M\, V_r s^2 + \beta_r {A_r}^2\right)}{{A_p}^2 \beta_p \left(\beta_r k_{Q_r,p_r} + V_r s\right) - \left(\beta_p k_{Q_p,p_p} - V_p s\right)\left(\beta_r M k_{Q_r,p_r} s + M\, V_r s^2 + \beta_r {A_r}^2\right)} \tag{5.43}$$

where $\lambda_{p,v}^{d} = 1 - \lambda_{p,v}^{o}$. It should be noted that the absolute value is calculated since the relative gains with valve openings as inputs contain an imaginary part when evaluated at a frequency.

The coupling analysis is limited to the low and high frequency range since it was not possible to analyse Equation (5.43) for intermediate frequencies due to the complexity of the analytical expression of the relative gain.

5.3.1 Low Frequency Range

For low frequencies, the expression for the RGA element is rewritten as shown in Equation (5.44) as $s \to 0$ and it should be noted that for low frequencies, $\lambda_{p,v}^{d} = \lambda_{r,v}^{d}$.

$$\lambda_{p,v}^{d} = -\frac{\alpha^2\, k_{Q_p,p_p}}{k_{Q_r,p_r} - \alpha^2\, k_{Q_p,p_p}} \tag{5.44}$$

where, for the diagonal pairing the inequality shown in Equation (5.45) must hold true for $|\lambda_{Q_p p_p}| \approx 1$.

$$\left|k_{Q_p,p_p}\, \alpha^2\right| \gg |k_{Q_r,p_r}| \tag{5.45}$$

It should be noted that the analysis becomes independent of volumes and thereby also piston position. This was not the case when analysing the coupling with flows as inputs in the low frequency range. Furthermore, it is assumed that if one cylinder chamber is connected to the pump, the other is connected to tank i.e. the sign of the valve opening, x_v, for each valve is equal which is the case in steady state. The linearisation coefficients of the orifice equation are dependent on the flow direction and the low frequency analysis is therefore divided into positive and negative flows.

Positive Flows

Inserting linearisation coefficients from Equations (4.16) and (4.17) for positive flow into Equation (5.45) yields Equation (5.46) which must hold true in the case of a diagonal pairing.

$$\left|\lambda_{p,v}^{d}\right| \approx 1: \quad 1 \gg \frac{1}{\alpha^2}\frac{x_{vr}^*}{x_{vp}^*}\frac{k_{vr}}{k_{vp}}\frac{\sqrt{|p_s - p_p^*|}}{\sqrt{|p_r^* - p_t|}} \tag{5.46}$$

Where the asterisk denotes linearisation points. From the steady state flow equations, the valve ratio is defined as shown in Equation (5.47). The steady state equations are used since the coupling at low frequencies is analysed.

$$\begin{aligned} Q_r &= Q_p\,\alpha \\ k_{vr}\,x_{vr}\sqrt{|p_r - p_t|} &= k_{vp}\,x_{vp}\sqrt{|p_s - p_p|}\,\alpha \\ &\Updownarrow \\ \frac{x_{vr}}{x_{vp}} &= \alpha\frac{k_{vp}}{k_{vr}}\frac{\sqrt{|p_s - p_p|}}{\sqrt{|p_r - p_t|}} \end{aligned} \tag{5.47}$$

Substituting Equation (5.47) into Equation (5.46) yields Equation (5.48).

$$\left|\lambda_{p,v}^{d}\right| \approx 1: \quad 1 \gg \frac{1}{\alpha}\frac{\left|p_s - p_p^*\right|}{|p_r^* - p_t|} \tag{5.48}$$

As seen in the inequality in Equation (5.48), for a diagonal pairing the RHS must be strictly lower than 1. Furthermore, the analysis becomes independent of the valve coefficient. The RHS of Equation (5.48) is computed and shown as black contour levels depending on p_p, p_r, and α. The black contours showing the couplings are initially explained, followed by an explanation of the coloured contours showing steady state requirements.

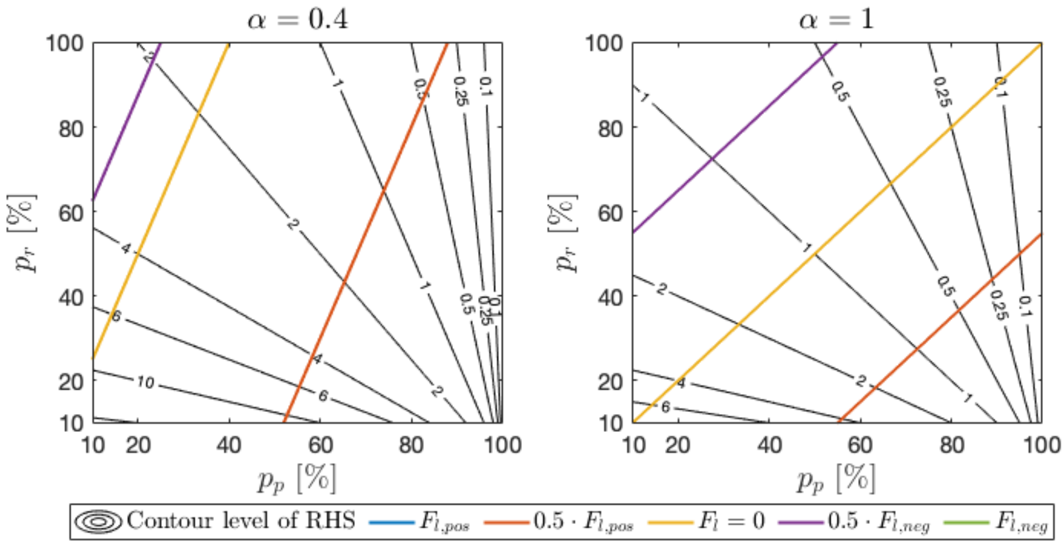

Figure 5.8: Contour levels of the RHS of Equation (5.48).

The pressures have been limited between 10 [%] and 100 [%] of the supply pressure as operating at pressures below 10 [%] of supply pressure reduces the oil stiffness significantly. For $\alpha = 0.4$, it is seen that for high p_p, the inequality in Equation (5.48) is satisfied as the contours are strictly lower than 1 i.e. diagonal pairing is less coupled than the off-diagonal pairing when operating in this pressure range. If the contours are strictly greater than 1 which is the case in the lower pressure range, the cross couplings when pairing the off-diagonal are less significant. For $\alpha = 1$ the domain in which the contours are strictly greater than 1 is more limited, however, the domain for contours strictly lower than 1 becomes larger. This is due to the contours rotating counterclockwise about the lower right corner as α is increased from 0.4 to 1. The operating range where the system can be regarded as decoupled is in general very restricted, regardless of α.

Figure 5.8 is valid for steady state, thus Equation (5.49) must be satisfied where frictional forces are neglected.

$$F_l = p_p\, A_p - p_r\, A_r \tag{5.49}$$

Defining the maximum load forces as Equation (5.50) by assuming the minimum system pressure as 10 [%] of the supply pressure to maintain a certain oil stiffness.

$$\begin{aligned} F_{l,neg} &= 0.1\, p_s\, A_p - p_s\, A_r \\ F_{l,pos} &= p_s\, A_p - 0.1\, p_s\, A_r \end{aligned} \tag{5.50}$$

Where $|F_{l,pos}| > |F_{l,neg}|$ when $\alpha < 1$ as the piston side pressure force contributes a larger pressure force than the rod side when the two chamber pressures are equal. It should be noted that $F_{l,neg}$ is negative according to the load force convention presented in Chapter 3 as the rod side chamber becomes load carrying. This is shown in Figure 5.9 where $F_{l,neg}$ and $F_{l,pos}$ are positive in the direction of the arrows.

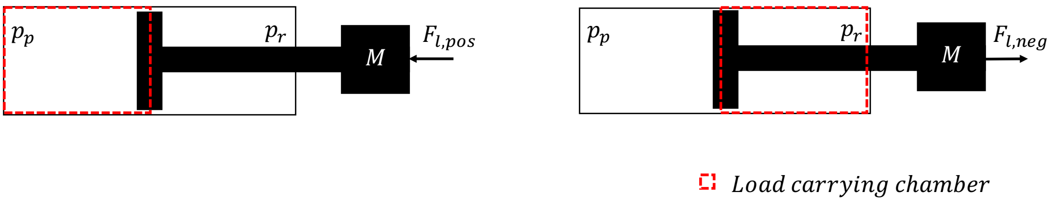

Figure 5.9: Load force definition.

This definition of the load force ensures at least one combination of the pressures p_p and p_r which equals the load force. By varying the load force in the interval $F_{l,neg}$ to $F_{l,pos}$, the values of p_p and p_r for satisfying Equation (5.49) are shown by the colored contours in Figure 5.8. The contours describe p_r as a function of p_p, α, F_l, and A_r as shown in Equation (5.51).

$$p_r = p_p \frac{1}{\alpha} - \frac{F_l}{A_r}, \qquad F_{l,neg} \leq F_l \leq F_{l,pos} \tag{5.51}$$

The load force contours are however independent of A_r as the load force is calculated using A_r. The pressures p_p and p_r are constrained between the green contour where $F_l = F_{l,neg}$ which is tangent to the upper left corner of the figure and the blue contour where $F_l = F_{l,pos}$ which is tangent to the lower right corner hence the green and blue contours are not visible. A load force contour shows the pressure combinations to achieve steady state, for the given load force.

The restriction in pressure operating range from the RHS of Equation (5.48) previously mentioned, also restricts the system load force if steady state is to be reached. This can be seen in Figure 5.8 where $\alpha = 0.4$. For a diagonal pairing i.e. contours below 0.25, the load force of the system is restricted to approximately $F_l > 0.5\,F_{l,pos}$. For an off-diagonal pairing i.e. contours above 4, the load force should be $0.4\,F_{l,neg} < F_l < 0.75\,F_{l,pos}$ to reach steady state for the decoupled operating conditions. For $\alpha = 1$ and a diagonal pairing, the load force is restricted as $F_l > 0.25\,F_{l,neg}$. For an off-diagonal pairing, the load force should satisfy $0.2\,F_{l,neg} < F_l < 0.5\,F_{l,pos}$.

The friction effects of the piston have not been shown in Figure 5.8. As a result of friction, the maximum load force would become numerically smaller, and the contours would be squeezed towards the yellow contour where $F_l = 0$.

If the supply pressure is over-dimensioned compared to the load force then the pressure working area is reduced as shown in Appendix B.3.1 and the above conclusions about the pressure working area will change.

Negative Flows

Substituting the linearisation coefficients for negative flow into Equation (5.45) yields Equation (5.52) which must hold true for the case of a diagonal pairing.

$$\left|\lambda_{p,v}^{d}\right| \approx 1 : \quad 1 \gg \frac{1}{\alpha^2}\frac{x_{vr}^*}{x_{vp}^*}\frac{k_{vr}}{k_{vp}}\frac{\sqrt{|p_t - p_p^*|}}{\sqrt{|p_r^* - p_s|}} \tag{5.52}$$

As for the positive flow, a valve opening ratio is defined as shown in Equation (5.53).

$$\begin{aligned} Q_r &= Q_p\,\alpha \\ k_{vr}\,x_{vr}\sqrt{|p_r - p_s|} &= k_{vp}\,x_{vp}\sqrt{|p_t - p_p|}\,\alpha \\ &\Updownarrow \\ \frac{x_{vr}}{x_{vp}} &= \alpha\frac{k_{vp}}{k_{vr}}\frac{\sqrt{|p_t - p_p|}}{\sqrt{|p_r - p_s|}} \end{aligned} \tag{5.53}$$

Where, substituting Equation (5.53) into Equation (5.52) yields Equation (5.54).

$$\left|\lambda_{p,v}^{d}\right| \approx 1 : \quad 1 \gg \frac{1}{\alpha}\frac{\left|p_t - p_p^*\right|}{\left|p_r^* - p_s\right|} \tag{5.54}$$

Figure 5.10 is equivalent to Figure 5.8, the black contour levels are however shown for the RHS of Equation (5.54).

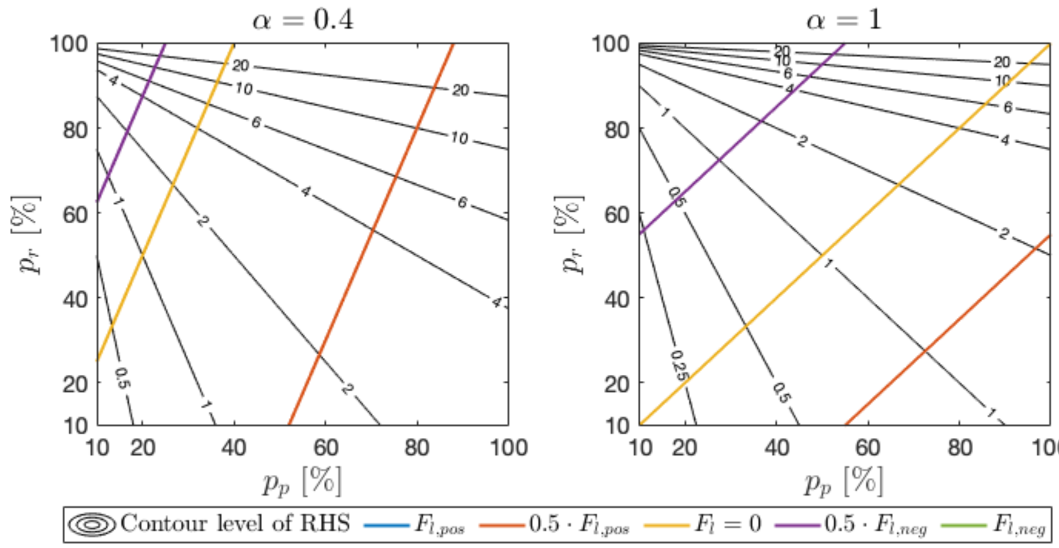

Figure 5.10: Contour plot showing the value of the right hand side, RHS, of Equation (5.54).

The load force contours are equivalent to the load force contours for the positive flow. For $\alpha = 0.4$, a diagonal pairing is not possible as the threshold contour value of 0.25 is outside the operating range. For an off-diagonal pairing, only p_r needs to be in the higher pressure range, and steady state is only achievable for $F_l < 0.75\,F_{l,pos}$.

For $\alpha = 1$, the operating pressures should be kept low and the load force, $0.5\,F_{l,neg} < F_l < 0.1\,F_{l,pos}$ for a diagonal pairing. For an off-diagonal pairing, only p_r should be in the higher pressure range and the load force $F_l < 0.25\,F_{l,pos}$.

As α is increased from 0.4 to 1 the contours rotate clockwise around the upper left corner where the diagonal pairing range increases and the off-diagonal range decreases correspondingly.

In conclusion to the steady state analysis, the necessary operating pressures to avoid cross couplings are very limited. Furthermore, if the system is dimensioned according to Equation (5.50)*, due to the system couplings, steady state can not be reached for all load forces if the decoupled operating conditions are to be maintained.*

The conclusions for lower frequencies are summarised in Table 5.4.

α	Q	p	F_l
0.4	>0	High p_p	$F_l > 0.5\, F_{l,pos}$
		Low p_p and p_r	$0.4\, F_{l,neg} < F_l < 0.75\, F_{l,pos}$
	<0	Not Possible	Not Possible
		High p_r	$F_l < 0.75\, F_{l,pos}$
1	>0	High p_p	$F_l > 0.25\, F_{l,neg}$
		Low p_p and p_r	$0.2\, F_{l,neg} < F_l < 0.5\, F_{l,pos}$
	<0	Low p_p and p_r	$0.5\, F_{l,neg} < F_l < 0.1\, F_{l,pos}$
		High p_r	$F_l < 0.25\, F_{l,pos}$

Table 5.4: Summarised conclusions for the low frequency range for valve openings as inputs. Grey rows are diagonal restrictions and white rows are off-diagonal restrictions.

The table should be read from left to right, i.e. initially choosing an area ratio, α, followed by a flow direction, which leads to the restrictions for either diagonal or off-diagonal pairing. It should be noted that the table values are approximations and the values are based on the definition of load force. The results would, therefore, depend on how the supply pressure is dimensioned compared to the load force. If α is between 0.4 and 1 then the restrictions on the pressures will be in between.

5.3.2 High Frequency Range

The high frequency range is investigated by taking the expression for $\lambda^d_{p,v}$ shown in Equation (5.43) and substituting $s = j\,\omega$. For the diagonal pairing the expression in Equation (5.55) must hold true.

$$\lambda^d_{p,v} = \frac{k_1 + k_2\,\omega^2 + j(k_3\,\omega + k_4\,\omega^3)}{k_1 + k_2\,\omega^2 + j(k_3\,\omega + k_4\,\omega^3) + (k_5 + j\,k_6\,\omega)} \approx 1 \tag{5.55}$$

$$\begin{aligned}
k_1 &= -A_r^2\,\beta_p\,\beta_r\,k_{Q_p p_p}\\
k_2 &= \beta_p\,k_{Q_p p_p}\,V_r\,M - \beta_r\,k_{Q_r p_r}\,V_p\,M\\
k_3 &= A_r^2\,\beta_r\,V_p\, - \beta_p\,\beta_r\,k_{Q_p p_p}\,k_{Q_r p_r}\,M)\\
k_4 &= -V_p\,V_r\,M\\
k_5 &= A_p^2\,\beta_p\,\beta_r\,k_{Q_r,p_r}\\
k_6 &= A_p^2\,\beta_p\,V_r
\end{aligned}$$

As the frequency is cubed in the numerator and denominator in Equation (5.55), the expression goes to 1 as the frequency goes towards infinity. This is shown in Equation (5.56).

$$\begin{aligned}
\lim_{\omega\to\infty} \lambda^d_{p,v}(\omega) &= 1\\
\lim_{\omega\to\infty} \lambda^o_{p,v}(\omega) &= 0
\end{aligned} \tag{5.56}$$

This suggests that for larger frequencies, the diagonal pairing is recommended.

The RGA-element for rod side pressure as one of the outputs is shown in Equation (5.57).

$$\lambda^d_{r,v} = -\frac{A_r^2\,\beta_r\,(\beta_p k_{Q_p,p_p} - V_p s)}{(\beta_r k_{Q_r,p_r} + V_r s)\left(-\beta_p M k_{Q_p,p_p} s + M\,V_p s^2 + {A_p}^2 \beta_p\right) - A_r^2\,\beta_r\,(\beta_p k_{Q_p,p_p} - V_p s)} \tag{5.57}$$

The high frequency range is investigated for $\lambda^d_{r,v}$ where the expression in Equation (5.58) must hold true for a diagonal pairing.

$$\lambda^{d}_{r,v} = \frac{k_1 + j\,k_2\,\omega}{k_1 + j\,k_2\,\omega + k_3 + k_4\,\omega^2 + j(k_5\,\omega + k_6\,\omega^3)} \approx 1 \tag{5.58}$$

$$\begin{aligned}
k_1 &= A_r^2\,\beta_p\,\beta_r\,k_{Q_p p_p} \\
k_2 &= A_r^2\,\beta_r\,V_p \\
k_3 &= A_p^2\,\beta_p\,\beta_r\,k_{Q_r,p_r} \\
k_4 &= -\beta_r\,M\,V_p\,k_{Q_r,p_r} + \beta_p\,M\,V_r\,k_{Q_p,p_p} \\
k_5 &= -\beta_p\,\beta_r\,M\,k_{Q_p p_p}\,k_{Q_r,p_r} + A_p^2\,\beta_p\,V_r \\
k_6 &= -M\,V_p\,V_r
\end{aligned}$$

Letting the frequency go towards infinity, the denominator becomes larger as the frequency is cubed. This is shown in Equation (5.59).

$$\begin{aligned}
\lim_{\omega\to\infty} \lambda^{d}_{r,v}(\omega) &= 0 \\
\lim_{\omega\to\infty} \lambda^{o}_{r,v}(\omega) &= 1
\end{aligned} \tag{5.59}$$

This suggests that for larger frequencies, the off-diagonal pairing is recommended.

The known values of $\lambda^{d}_{p,v}$ and $\lambda^{o}_{p,v}$ are shown in Figure 5.11.

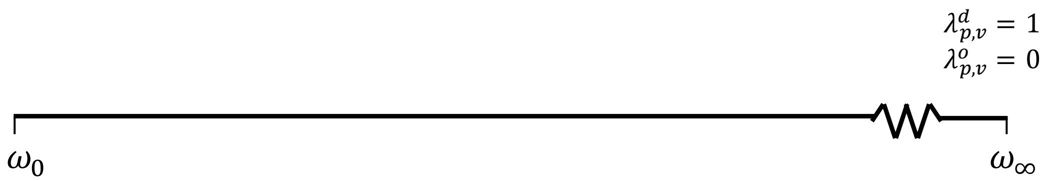

Figure 5.11: Values of $\lambda^{d}_{p,v}$ and $\lambda^{o}_{p,v}$ for each frequency.

The known values of $\lambda^{d}_{r,v}$ and $\lambda^{o}_{r,v}$ are shown in Figure 5.12.

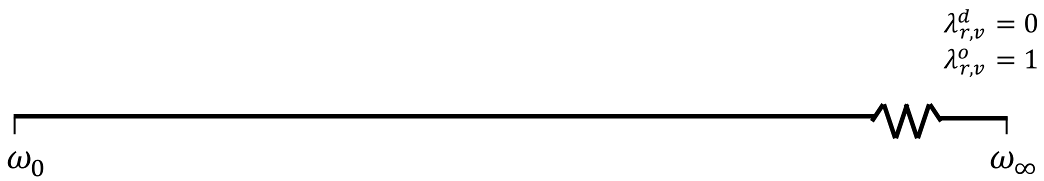

Figure 5.12: Values of $\lambda^{d}_{r,v}$ and $\lambda^{o}_{r,v}$ for each frequency.

5.4 Comparison of Flows and Valve Openings as Inputs

The relative gain when pairing one of the pressures with either piston position, velocity, or acceleration was analysed in Section 5.2 with flows as inputs. The relative gain when pairing one of the pressures with either flow, piston position, velocity, or acceleration was analysed in Section 5.3 with valve openings as inputs. These conclusions are compared in this section to clarify the difference when changing the inputs. It should be noted that it was only possible to evaluate the relative gain with valve openings as inputs for low and high frequencies, i.e. $s \to 0$ and $s \to \infty$.

Low Frequency Range

At low frequencies, $\lambda^d_{p,v}$ does not depend on the piston position whereas $\lambda^d_{p,f}$ is highly dependent on piston position. The relative gains are repeated in Equations (5.60) and (5.61) where the relation between them is seen.

$$\lambda^d_{p,f} = \frac{V_p\, V_r\, M\, s^2 + A_r^2\, \beta_r\, V_p}{V_p\, V_r\, M\, s^2 + A_r^2\, \beta_r\, V_p + A_p^2\, \beta_p\, V_r} = \frac{n_{x_p p_p}}{d_{x_p p_p}} \tag{5.60}$$

$$\lambda^d_{p,v} = \frac{C_1 + n_{x_p p_p}\, s}{C_1 + C_2 + d_{x_p p_p}\, s} \tag{5.61}$$

where C_1, C_2 and C_3 are independent of piston position. The numerator and denominator for $\lambda^d_{p,f}$ recur in $\lambda^d_{p,v}$ but are multiplied by s. That means there is a relation between them but at low frequencies $s \to 0$ the terms become neglectable for $\lambda^d_{p,v}$ and that is the reason why $\lambda^d_{p,v}$ is independent of piston position for low frequencies.

High Frequency Range

For high frequencies, the conclusions in Equations (5.62) and (5.63) were found for flows and valve openings as inputs respectively.

$$\lim_{\omega\to\infty} \lambda^d_{p,f}(\omega) = 1 \qquad \text{and} \qquad \lim_{\omega\to\infty} \lambda^o_{r,f}(\omega) = 1 \tag{5.62}$$

$$\lim_{\omega\to\infty} \lambda^d_{p,v}(\omega) = 1 \qquad \text{and} \qquad \lim_{\omega\to\infty} \lambda^o_{r,v}(\omega) = 1 \tag{5.63}$$

By comparing the conclusions in Equations (5.62) and (5.63), it is seen that the relative gains are equal for high frequencies independent of whether flows or valve openings are inputs.

$$\lim_{\omega\to\infty} \lambda^d_{p,v}(\omega) = \lim_{\omega\to\infty} \lambda^d_{p,f}(\omega) = 1$$
$$\lim_{\omega\to\infty} \lambda^o_{r,v}(\omega) = \lim_{\omega\to\infty} \lambda^o_{r,f}(\omega) = 1 \tag{5.64}$$

5.4.1 Final Conclusions

It is concluded that there is a relation between the cross couplings when using flows as inputs compared to valve openings as inputs. The conclusions from Section 5.2 when flows are inputs are listed below:

- Piston side pressure and either position, velocity or acceleration as outputs: off-diagonal pairing should be used. However, the piston working range and frequency range are very limited so a decoupling pre-compensator or MIMO controllers are suggested.
- Rod side pressure and either position, velocity or acceleration as outputs: diagonal pairing should be used. However, the piston working range and frequency range are very limited so a decoupling pre-compensator or MIMO controllers are suggested.

It is not possible to conclude which pairing to use when valve openings are inputs since the couplings are only analysed at $s \to 0$ and $s \to \infty$. In the following section, the numerical RGA is calculated to verify the conclusions made in this section and to check which impact it has on the couplings to use valve openings as inputs for the entire frequency range.

5.5 Numerical RGA

The coupling has now been analysed analytically for the state space models with flows and valve openings as inputs. The RGA element is found numerically to verify the analytic conclusions. The analytic conclusions were limited to certain frequencies whereas a numerical RGA analysis will show the coupling for the full frequency range. Finally, the assumptions of neglecting leakage, viscous friction and dead volumes are analysed numerically with the extended state space model described in Section 4.3.

For this thesis, the numerical RGA analysis is, however, only analysed for a single differential cylinder using SMISMO. The cylinder analysed is the main cylinder seen in Figure 7.1 in Chapter 7 which will be described later. For this numerical analysis, the main cylinder is analysed separately from the bearing and the load cylinder where only the mass of the main piston is included. The used parameters for the main cylinder are validated in Section 7.3. Even though the leakage flow in the main cylinder is non-existent, for this numerical comparison, the leakage coefficient was arbitrarily chosen to $C_{le} = 1 \cdot 10^{-13}$ to see how the leakage flow changes the RGA element.

In Figure 5.13, $\lambda^d_{p,f}$ and $\lambda^o_{p,f}$ are compared for $x_p = 5$ [%] and $x_p = 95$ [%] of stroke length. Figure 5.14 is the corresponding zoomed view at the frequencies ω_c, ω_w, and ω_n.

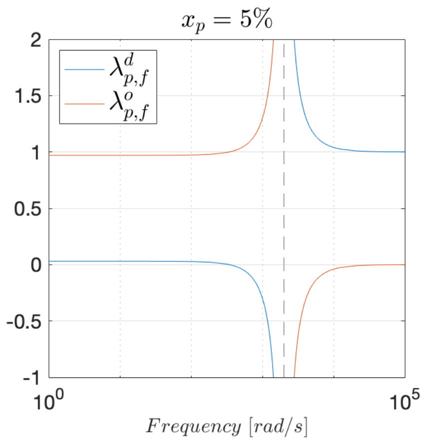

Figure 5.13: RGA elements for flows as inputs at $x_p = 5$ [%] and $x_p = 95$ [%].

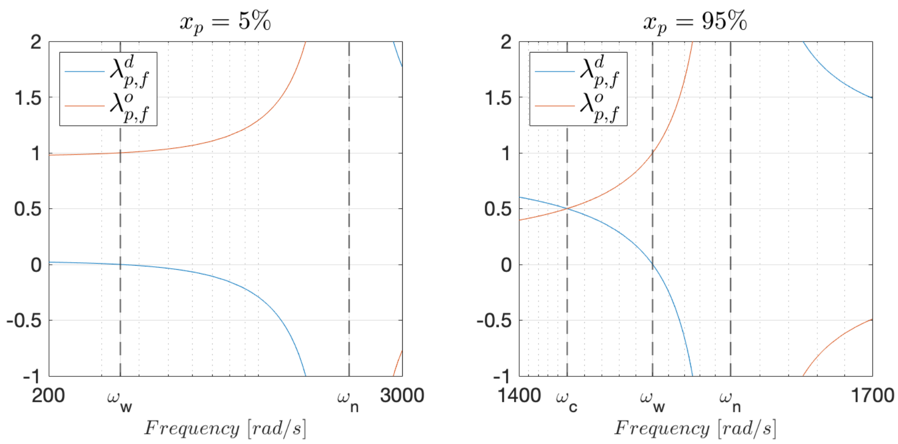

Figure 5.14: Zoomed view at the frequencies of interest.

The figures confirm that the recommended pairing at low frequencies depends on x_p which was realised by Figure 5.5. The conclusions at the different frequencies ω_c, ω_w, ω_p, and ω_∞ are confirmed. For $x_p = 5$ [%] Equation (5.35) is not satisfied and $\lambda^d_{p,f}$ and $\lambda^o_{p,f}$ do not cross. For $x_p = 95$ [%], Equation (5.35) is satisfied and $\lambda^d_{p,f} = \lambda^o_{p,f}$ at w_c, which is seen in Figure 5.14.

The relative gains are compared for the three state space models from Section 4 to analyse the effects of including the non-linear orifice equations, viscous friction, leakage, and dead volumes on the couplings. $\lambda^d_{p,f}$ is with flows as inputs, $\lambda^d_{p,v}$ with valve openings as inputs, and $\lambda^d_{p,v,e}$ is for the extended model with valve openings as inputs. To compare $\lambda^d_{p,f}$ with $\lambda^d_{p,v}$ and $\lambda^d_{p,v,e}$, the absolute values are computed, since $\lambda^d_{p,v}$ and $\lambda^d_{p,v,e}$ have an imaginary part. The comparison is shown in Figure 5.15.

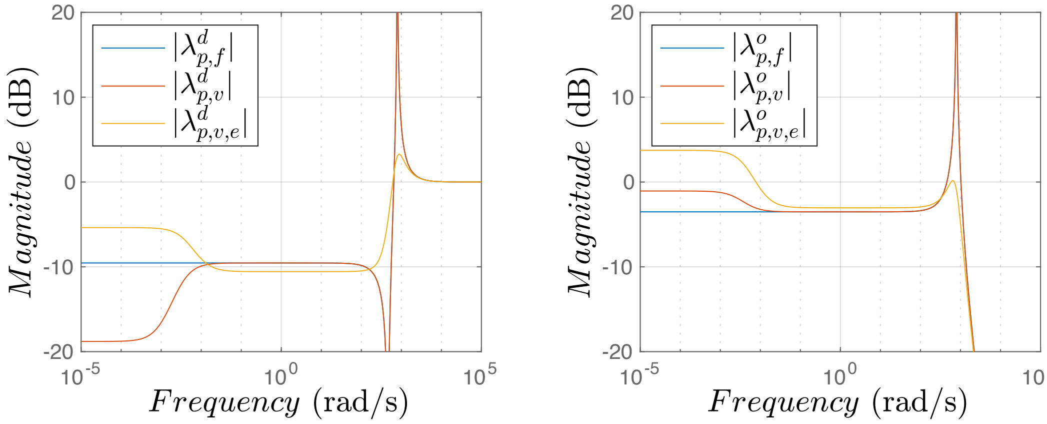

Figure 5.15: Numerical RGA element when pairing p_p and x_p for all three state space models.

It must be pointed out, that the absolute value of the RGA element can be misleading as described in Section 5. The RGA element plot is valid for all input-output pairings which include p_p. The same is true for the RGA elements of the extended model. $|\lambda|$ is shown in decibel to clarify the difference, where 0 [dB] equals a unity gain. By comparing $|\lambda^o_{p,f}|$ and $|\lambda^o_{p,v}|$, the RGA elements are identical for all frequencies except for low frequencies. This conclusion agrees with the analytic analysis. It was, however, only possible to compare them analytically at $\omega = 0$ and $\omega \to \infty$ in Section 5.4.

When comparing with $|\lambda^o_{p,v,e}|$, the RGA element at low frequencies is further changed due to the included leakage flow. The included viscous friction changes the RGA element around the natural frequency ω_n. The included dead volume does slightly change the RGA element at frequencies from approximately 10^{-2} to 10^{2} [rad/s], but it does not change any conclusions of recommended pairing. The RGA element is mostly changed in the low frequency range when analysing the coupling with the three different state space models. The recommended pairing for all three models is, however, the same; at frequencies below the natural frequency, the off-diagonal pairing $|\lambda_p^o|$ is closest to 1, while above, pairing through the diagonal, $|\lambda_p^d|$ is closer to 1. It is further seen in Figure 5.15 that the coupling of $|\lambda_{v,e}|$ at intermediate frequencies between 10^{-2} and 10^2 can be estimated fairly precise with the low frequency coupling of $|\lambda_f|$ from Equations (5.21) and (5.22).

The conclusions of the analytical RGA analysis when flows are inputs are useful for determining the couplings when valve openings are inputs as well. Furthermore, the analytic conclusions are valid even though the leakage flow, viscous friction, and dead volumes were neglected.

The numerical analysis for pairing p_r and x_p is shown in Figure 5.16.

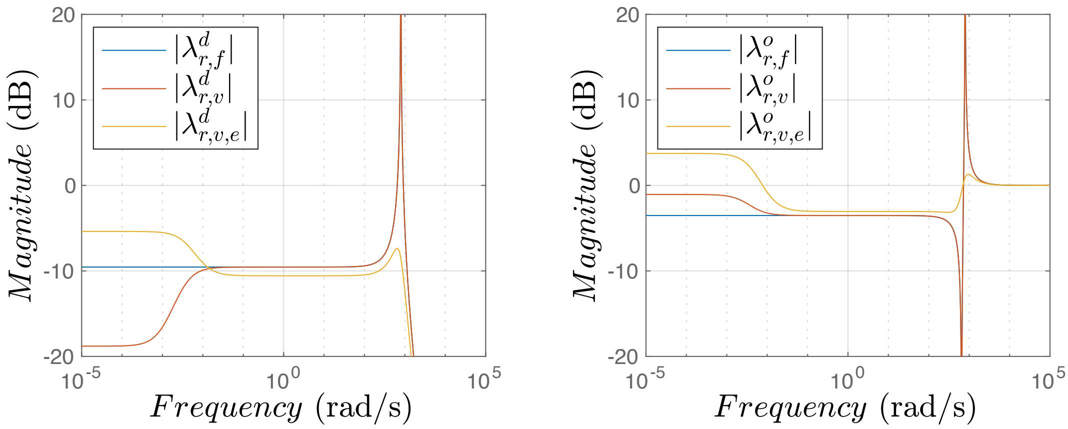

Figure 5.16: Numerical RGA element when pairing p_r and x_p for all three state space models.

The numerical conclusions follow the analytical conclusions in the same way as the pairing of p_p and x_p. The same tendency when comparing the three models is seen.

Lastly, it is numerically confirmed that at low frequencies, the RGA element with valve openings as inputs is independent of piston position as seen in Equation (5.48) as the low frequency coupling did not change when changing the piston position. With flows as inputs it is heavily dependent on the piston position as seen in Equation (5.21).

Chapter 6

Conclusion

The focus of this thesis is Investigation of Separate Meter-In Separate Meter-Out Control Strategies. The first part contains a general analysis of hydraulic SMISMO systems and the following questions have been answered during Part I:

1. *What are the suitable pairings of control variables for a hydraulic cylinder using SMISMO?*
2. *How do operating conditions and parameter variations influence the system couplings?*

To answer the first question, a general dynamic model of a hydraulic cylinder in SMISMO configuration was derived followed by a control combination analysis. The analysis considered several control combinations and these were found to be either not suitable, suitable but dependent, or suitable and highly independent. To answer the second question, the highly independent control combinations were analysed in an RGA analysis to determine how operating conditions and parameter variations affect the couplings of the system.

Suitable Pairings

The suitable pairings were found to be either dependent or highly independent. Pairings which were not suitable were algebraically coupled where steady state was not achievable. The dependent pairings were not algebraically connected, however, the references could not be set independently. The dependent control variables could be implemented in a cascade control structure with the reference for the inner loop depending on the error of the outer loop. In Table 6.1, the non-suitable pairings of control variables are marked with red crosses, the dependent pairings with yellow checkmarks, and the highly independent pairings with green checkmarks.

Q_p	×								
Q_r	×	×							
x_p	✓	✓	×						
$\dot{x}_p$	×	×	✓	×					
$\ddot{x}_p$	✓	✓	✓	✓	×				
p_p	✓	✓	✓	✓	✓	×			
p_r	✓	✓	✓	✓	✓	×	×		
F_p	✓	✓	✓	✓	×	×	×	×	
Slave	✓	✓	✓	✓	✓	✓	✓	✓	×
	Q_p	Q_r	x_p	$\dot{x}_p$	$\ddot{x}_p$	p_p	p_r	F_p	Slave

Table 6.1: Not suitable, dependent, and highly independent control combinations.

The highly independent variables are not algebraically connected and the references can be set independently of each other, however, limits exist. The highly independent control combinations are evaluated for four cases, i.e. for positive and negative load forces along with positive and negative velocities. All highly independent combinations contain the pressure, where the pressure must be controlled in the non-load carrying chamber.

System Couplings

Based on Table 6.1, only the system couplings for highly independent control combinations were investigated. An analytic RGA analysis was conducted to generalise the coupling analysis. The leakage flow, viscous friction, and dead volumes were neglected to simplify the analytic expressions of the couplings. The simplifications made for the analytical analysis were numerically verified where the leakage flow, viscous friction, and dead volumes were included. It was found that similarities occurred for intermediate frequencies, the natural frequency, and higher frequency. The low frequency couplings did, however, vary between the numerical and analytic analysis as the included leakage flow changed the low frequency coupling. The analytic expression of the low frequency coupling, when analysed with a state space model with flows as inputs, did not change when the frequency increased from low frequencies up to and including intermediate frequencies, which is below the natural frequency. At the intermediate frequencies, the couplings of the numerical and analytic model were similar. The couplings at intermediate frequencies can thereby, with low error, be found from the low-frequency analytic equation containing the piston position, bulk modulus, and piston area ratio. The analytic analysis further showed that the couplings at intermediate frequencies were mostly dependent on the piston position.

Both the analytic and numerical coupling analysis showed significant couplings at the natural frequency. At higher frequencies, when controlling the piston or rod side pressure along with either position, velocity, acceleration or flow and the frequency $\omega \to \infty$, the couplings are minimal and independent of operating conditions and parameters.

Part II

Analysis and Control of a Hydraulic SMISMO System

Chapter 7

Dynamic Model

This chapter is the beginning of Part II. In Part II the following question will be answered: *How can controllers be designed for the system to reduce reference tracking error?*

In this chapter, the experimental setup and simulation model is presented. The experimental setup consists of two hydraulic cylinders which are connected to a bearing allowing rotational movement around its centre point by translational movement of the cylinder pistons. The setup is normally used for pitch control of a wind turbine blade, however, as one of the cylinders is controlled by SMISMO valves, the setup is used in this thesis. The cylinder pistons are mechanically linked as seen in Figure 7.1 and assumed rigid.

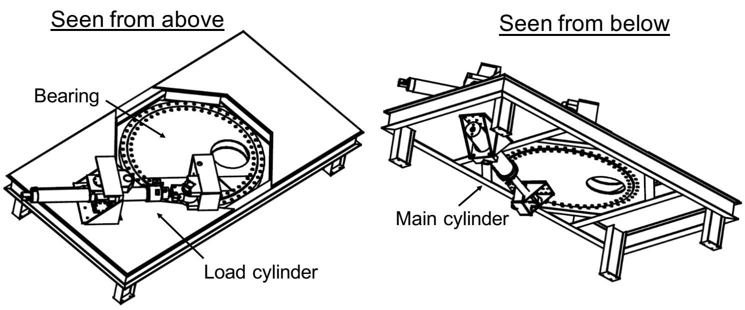

Figure 7.1: Mechanical diagram of the test setup [Hoberg et al., 2019].

A simple diagram of the dynamic model is shown in Figure 7.2 where the inputs are valve openings: x_{vmp}, x_{vmr}, and x_{vl}, and the output is piston position of the main cylinder, x_m. The subscript 'm' refers to the main cylinder and the subscript 'l'

refers to the load cylinder.

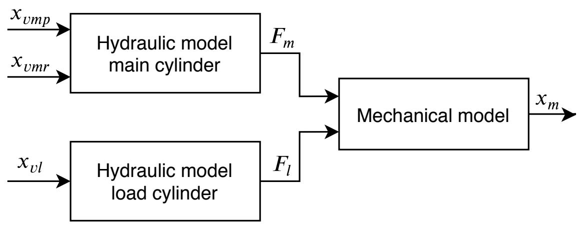

Figure 7.2: Dynamic model diagram.

The hydraulic models are derived in the next section.

7.1 Hydraulic Model

The hydraulic diagram is shown in Figure 7.3 without the mechanical connection between the cylinders. The directions of the valve openings are defined as in which direction the valves are moved, e.g. when $x_{vmp} > 0$ the piston side chamber is connected to the pump and when $x_{vmp} < 0$ the piston side chamber is connected to the tank.

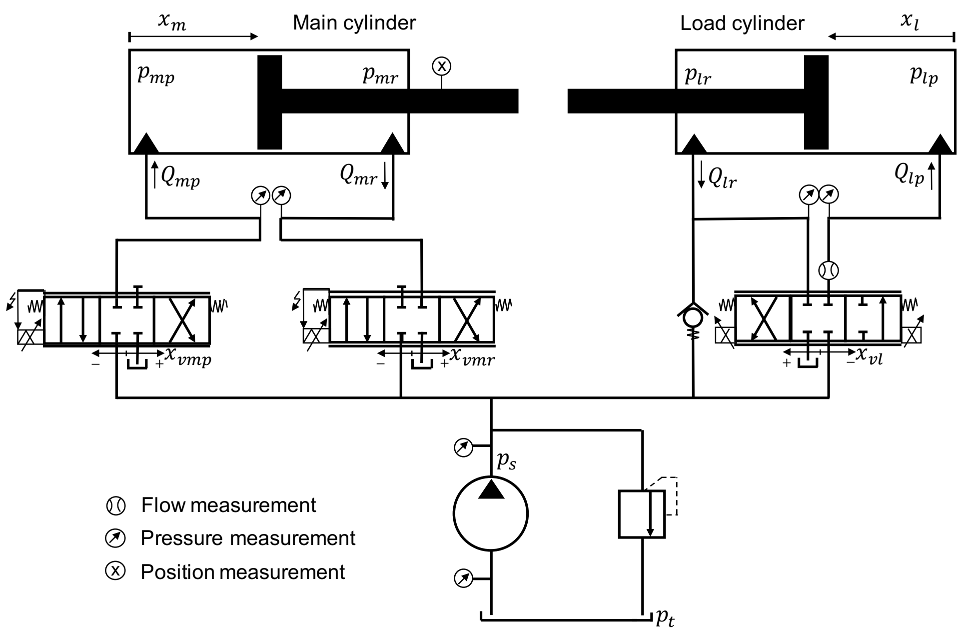

Figure 7.3: Hydraulic diagram of the test setup.

As seen in Figure 7.3, the main cylinder has a SMISMO valve configuration and is used to test the suitable control combinations previously analysed. The load cylinder is used for controlling the force acting on the main cylinder. The two valves controlling the main cylinder are 4/3 direct drive valves manufactured by *Moog*[Moog, 2020]. The valve controlling the load cylinder is a 4/3 flow regenerative valve manufactured by *Bosch Rexroth*[Rexroth, 2020]. The flow can only exit the rod side chamber of the load cylinder if the pressure drop across the check valve, i.e. from the rod side chamber to supply pressure, exceeds p_{cv}. The valve responses are estimated in Appendix C.1.

The flow through the valves are modelled by orifice equations. The valves connected to the main cylinder are modelled in Equations (7.1) and (7.2)[Hansen, 2019, p. 92-93]. The pressures and flows are defined in Figure 7.3.

$$Q_{mp} = \begin{cases} k_{vm}\, x_{vmp} \sqrt{|p_s - p_{mp}|}\, \frac{(p_s - p_{mp})}{|p_s - p_{mp}|}, & x_{vmp} \geq 0 \\ k_{vm}\, |x_{vmp}| \sqrt{|p_t - p_{mp}|}\, \frac{(p_t - p_{mp})}{|p_t - p_{mp}|}, & x_{vmp} < 0 \end{cases} \tag{7.1}$$

$$Q_{mr} = \begin{cases} k_{vm}\, x_{vmr} \sqrt{|p_{mr} - p_t|}\, \frac{(p_{mr} - p_t)}{|p_{mr} - p_t|}, & x_{vmr} \geq 0 \\ k_{vm}\, |x_{vmr}| \sqrt{|p_{mr} - p_s|}\, \frac{(p_{mr} - p_s)}{|p_{mr} - p_s|}, & x_{vmr} < 0 \end{cases} \tag{7.2}$$

The valve connected to the load cylinder is modelled in Equations (7.3) and (7.4).

$$Q_{lp} = \begin{cases} k_{vl}\, x_{vl} \sqrt{|p_s - p_{lp}|}\, \frac{(p_s - p_{lp})}{|p_s - p_{lp}|}, & x_{vl} \geq 0 \\ k_{vl}\, |x_{vl}| \sqrt{|p_t - p_{lp}|}\, \frac{(p_t - p_{lp})}{|p_t - p_{lp}|}, & x_{vl} < 0 \end{cases} \tag{7.3}$$

$$Q_{lr} = \begin{cases} k_{cv}\,(p_{lr} - p_s), & x_{vl} \geq 0,\ p_{lr} - p_s \geq p_{cv} \\ 0, & x_{vl} \geq 0,\ p_{lr} - p_s < p_{cv} \\ k_{vl}\, |x_{vl}| \sqrt{|p_{lr} - p_s|}\, \frac{(p_{lr} - p_s)}{|p_{lr} - p_s|}, & x_{vl} < 0 \end{cases} \tag{7.4}$$

The check valve is modelled as a spring-loaded check valve; p_{cv} is the pressure difference to overcome the spring force, and k_{cv} is the check valve flow coefficient. The valve openings x_{vmp}, x_{vmr}, and x_{vl} are normalised values between -1 and 1, and the coefficients k_{vm} and k_{vl} are defined in Equation (7.5)[Hansen, 2019, p. 93].

$$k_{vi} = \frac{Q_{nom,i}}{\sqrt{\Delta p_{nom,i}}}, \qquad i = m, l \tag{7.5}$$

The dynamics of the pressures in the cylinder chambers are modelled by the continuity equations. The pressure dynamics in the main cylinder are expressed in Equation (7.6)[Hansen, 2019, p. 77].

$$\begin{aligned} \dot{p}_{mp} &= \frac{\beta(p_{mp})}{V_{mp0} + A_{mp}\, x_m} (Q_{mp} - A_{mp}\, \dot{x}_m) \\ \dot{p}_{mr} &= \frac{\beta(p_{mr})}{V_{mr0} + A_{mr}\, (L_m - x_m)} (A_{mr}\, \dot{x}_m - Q_{mr}) \end{aligned} \tag{7.6}$$

The pressure dynamics in the load cylinder are expressed in Equation (7.7).

$$\begin{aligned} \dot{p}_{lp} &= \frac{\beta(p_{lp})}{V_{lp0} + A_{lp}\, x_m} (Q_{lp} - A_{lp}\, \dot{x}_m) \\ \dot{p}_{lr} &= \frac{\beta(p_{lr})}{V_{lr0} + A_{lr}\, (L_m - x_m)} (A_{lr}\, \dot{x}_m - Q_{lr}) \end{aligned} \tag{7.7}$$

The internal leakage flows in the cylinders are assumed negligible due to cylinder seals. V_{mp0}, V_{mr0}, V_{lp0}, and V_{lr0} are dead volumes which have been calculated based on lengths and diameters of the connected hoses. The bulk modulus, β, is expressed in Equation (7.8), where α is the percentage of air dissolved in the oil, n is the polytropic index which is 1.4 for an adiabatic process, p_0 is the atmospheric pressure, and β_0 is the maximum fluid stiffness[Hansen, 2019, 16-17].

$$\beta = \frac{(1-\alpha)\, e^{\frac{p_0 - p}{\beta_0}} + \alpha \left(\frac{p_0}{p}\right)^{\frac{1}{n}}}{\frac{1-\alpha}{\beta_0}\, e^{\frac{p_0 - p}{\beta_0}} + \frac{\alpha}{n\, p_0} \left(\frac{p_0}{p}\right)^{\frac{n+1}{n}}} \tag{7.8}$$

The forces caused by the pressures in the chambers of the hydraulic cylinders are expressed in Equation (7.9).

$$\begin{aligned} F_m &= \underbrace{p_{mp}\, A_{mp}}_{F_{mp}} - \underbrace{p_{mr}\, A_{mr}}_{F_{mr}} \\ F_l &= \underbrace{p_{lp}\, A_{lp}}_{F_{lp}} - \underbrace{p_{lr}\, A_{lr}}_{F_{lr}} \end{aligned} \tag{7.9}$$

The frictional forces in the cylinders are included in the mechanical model in the following section.

7.2 Mechanical Model

The mechanical connection between the cylinders is sketched in Figure 7.4. The left figure shows forces and torques, and the right figure shows angles, lengths, and centres of mass. Parameters in blue are variables while parameters in red are constants.

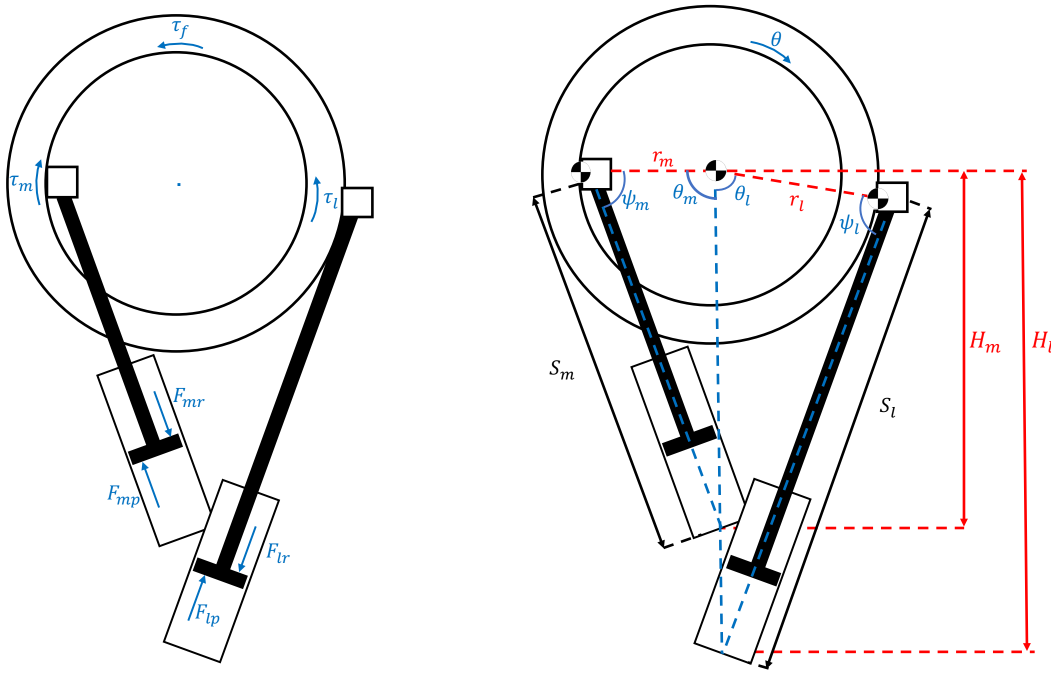

Figure 7.4: Diagram of the test setup.

The cylinder and bearing constants are listed in Table 7.1 where I is the moment of inertia of the bearing, M_m and M_l are the masses of the pistons, and L_m and L_l are stroke lengths for the main and load cylinder, respectively. A_{mp} and A_{mr} are piston areas in the main cylinder seen from the piston and rod side chambers, respectively, and A_{lp} and A_{lr} are piston areas in the load cylinder seen from the piston and rod side chambers, respectively.

Main cylinder			Load cylinder			Bearing		
Parameter	Value	Unit	Parameter	Value	Unit	Parameter	Value	Unit
M_m	80	$[kg]$	M_l	104	$[kg]$	I	380	$[kg\, m^2]$
L_m	0.7956	$[m]$	L_l	1.308	$[m]$	θ_{tot}	155.35	$[^o]$
A_{mp}	0.0154	$[m^2]$	A_{lp}	0.0154	$[m^2]$	$\theta_{m,max}$	118.03	$[^o]$
A_{mr}	0.0090	$[m^2]$	A_{lr}	0.0090	$[m^2]$	$\theta_{m,min}$	31.87	$[^o]$
r_m	0.583	$[m]$	r_l	0.9847	$[m]$	$\theta_{l,max}$	123.49	$[^o]$
H_m	1.415	$[m]$	H_l	1.855	$[m]$	$\theta_{l,min}$	37.324	$[^o]$
$S_{m,min}$	0.97	$[m]$	$S_{l,min}$	1.227	$[m]$			
$S_{m,max}$	1.766	$[m]$	$S_{l,max}$	2.535	$[m]$			

Table 7.1: Constants for the mechanical model[Vedel et al., 2019].

It should be noted that $S_m = S_{m,min} + x_m$ and $S_l = S_{l,min} + x_l$, where x_m and x_l are the piston positions as defined in Figure 7.3. From the law of cosines, $S_{m,max}$ is found from $S_{l,min}$, and $S_{l,max}$ is found from $S_{m,min}$. The stroke lengths are thereby $L_m = S_{m,max} - S_{m,min}$ and $L_l = S_{l,max} - S_{l,min}$. The minimum and maximum values of the bearing angles θ_m and θ_l are found from Equations (C.4) and (C.11) in Appendix C.3 at $x_m = 0$ and $x_m = L_m$. One of the pistons will thereby reach maximum stroke length when the other reach minimum stroke length. The calculated stroke length L_m has been confirmed from experimental data.

The torques caused by the forces from the hydraulic cylinders are expressed in Equation (7.10).

$$\begin{aligned} \tau_m &= F_m\, sin(\psi_m)\, r_m \\ \tau_l &= F_l\, sin(\psi_l)\, r_l \end{aligned} \tag{7.10}$$

Frictional forces in the hydraulic cylinders are modelled as part of the friction torque in the bearing which is expressed in Equation (7.11).[Hansen, 2019, p. 155]

$$\tau_f = \tau_c\, tanh(\dot{\theta}\, c) + B\, \dot{\theta}, \qquad \dot{\theta} \neq 0 \tag{7.11}$$

The friction torque is modelled as a combination of Coulomb and viscous friction. The discontinuous Coulomb friction is modelled by a continuous hyperbolic tangent function to avoid numerical complications, where the hyperbolic tangent function approaches the sign function as $c \rightarrow \infty$. A sketch of the friction torque as a function of angular velocity is shown in Figure 7.5.

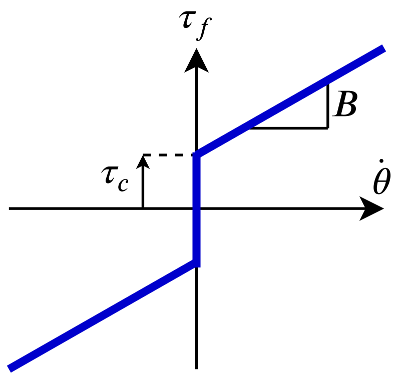

Figure 7.5: Friction model.

Newton's Second Law of Motion is expressed for the bearing in Equation (7.12).

$$\ddot{\theta}\, I_{eq} = \tau_m - \tau_l - \tau_f \tag{7.12}$$

The moment of inertia is expressed in Equation (7.13)[Meriam and Kraige, 2013, p. 642]. It should be noted that the exact positions of the centre of masses for the two pistons are not known, however, the lengths to the centre of masses are assumed to be approximately r_m and r_l regardless of the piston position.

$$I_{eq} = I + M_m\, r_m^2 + M_l\, r_l^2 \tag{7.13}$$

The mechanical model in Equation (7.12) is defined in joint space. To express the model in actuator space, i.e. seen from the main cylinder, algebraic equations describing the relation between angles and piston positions are derived. The derivation can be found in Appendix C.3.

The mechanical model is expressed in actuator space in Equation (7.14).

$$\ddot{x}_m = \frac{1}{I_{eq}\, G_m}\left(F_m\, G_{m1} - (B\, G_m + I_{eq}\, G_n\, \dot{x}_m)\, \dot{x}_m - tanh(\dot{x}_m\, c)\, \tau_C - F_l\, G_{l1}\right) \tag{7.14}$$

It should be noted that G_m, G_n, G_{m1}, and G_{l1} are all functions of the main piston position, x_m. Expressions for G_m, G_n, G_{m1}, and G_{l1} can be found in Equation (C.13) in Appendix C.3.

7.3 Model Validation

The non-linear dynamic simulation model previously presented is validated against experimental data in this section. The soft system parameters are varied on physical grounds, to properly mimic the physical system response where the emphasis is put on capturing the dynamics.

The oil bulk modulus β_0, air content in the fluid α, Coulomb and viscous friction coefficients, τ_c and B, are varied during validation due to high uncertainties. The proportional valve coefficients, k_{vm} and k_{vl}, are less uncertain and are varied close to the given datasheet values. The check valve coefficient, k_{cv}, and the check valve crack pressure, p_{cv}, are varied close to validated values from a previous student project [Vedel et al., 2019]. The dead volume in each chamber V_{mp0}, V_{mr0}, V_{lp0}, and V_{lr0}, is calculated based on hose dimensions. The uncertainty is therefore low and the dead volumes are not changed.

The validated parameters are shown in Table 7.2

Parameter	Value	Unit	Parameter	Value	Unit
B	$45 \cdot 10^3$	$[Nms/rad]$	α	5	$[\%]$
τ_c	200	$[Nm]$	β_0	$11.2 \cdot 10^3$	$[bar]$
p_{cv}	0.5	$[bar]$	V_{mp0}	$2.5 \cdot 10^{-4}$	$[m^3]$
k_{vl}	$3 \cdot 10^{-7}$	$[m^3/(sPa^{0.5})]$	V_{mr0}	$8.5 \cdot 10^{-4}$	$[m^3]$
k_{vm}	$2.6 \cdot 10^{-7}$	$[m^3/(sPa^{0.5})]$	V_{lp0}	$11 \cdot 10^{-4}$	$[m^3]$
k_{cv}	$1.9 \cdot 10^{-10}$	$[m^3/(sPa)]$	V_{lr0}	$7.1 \cdot 10^{-4}$	$[m^3]$

Table 7.2: Validated system parameters found from experimental tests.

The system dynamics are excited manually in open loop using the servo valves. The valve opening references are logged and used as input to the simulation, as no measurements of the actual openings are available. The actual spool position is modelled with the second order approximation as described in Appendix C.1. The measured pump pressure is used in the simulation model while the tank pressure is assumed constant as it is not measured. The pump pressure varies up to 25 $[bar]$ during the tested steps.

The validation is done with three tests where each valve is stepped while the two other valves are kept constant. The piston position and pressures from the tests are then compared with the simulation. The valve for the main cylinder connected to the piston side, x_{vmp}, is stepped in Figure 7.6, the valve for the main cylinder connected to the rod side, x_{vmr}, is stepped in Figure 7.7, and the valve for the load cylinder, x_{vl}, is stepped in Figure 7.8. All steps occur at $t = 0$ [s]. For Figure 7.6, the pump pressure and flows are also shown, however, it should be noted that only simulated flows are shown as these were not measured in the experimental tests.

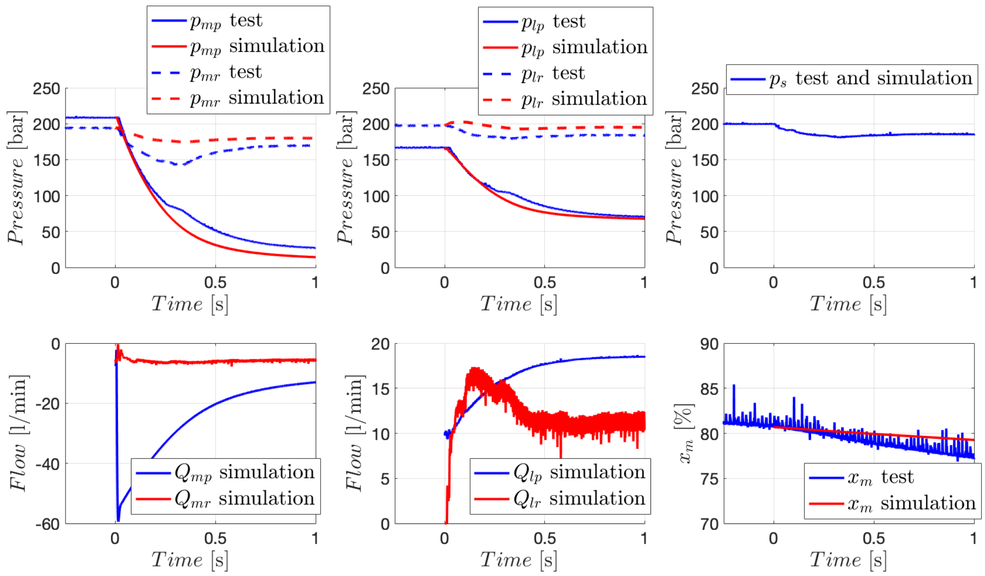

Figure 7.6: Stepping x_{vmp} from 50 [%] to -80 [%] at $t = 0[s]$.

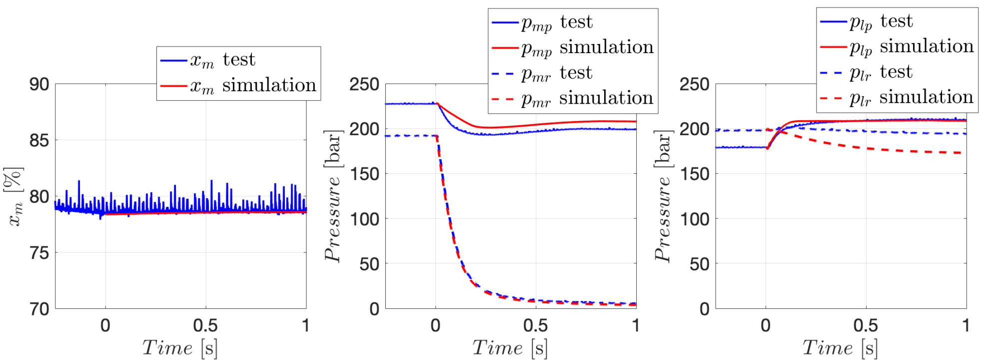

Figure 7.7: Stepping x_{vmr} from -40 [%] to 40 [%] at $t = 0[s]$.

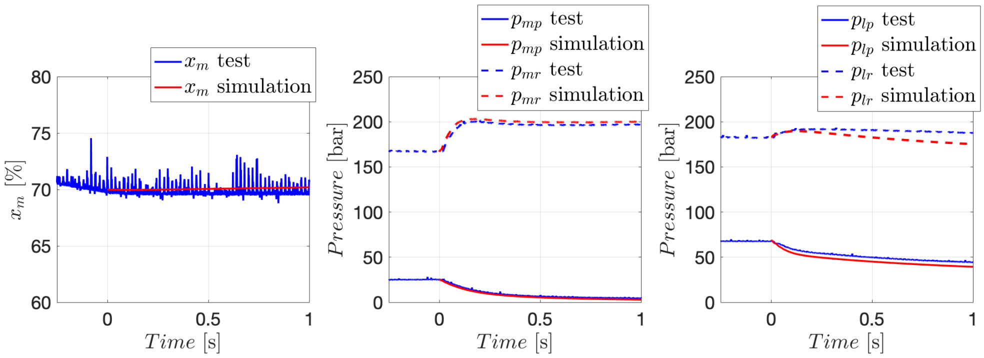

Figure 7.8: Stepping x_{vl} from 30 [%] to -10 [%] at $t = 0[s]$.

The valve dynamics are not obvious in the figures due to a faster bandwidth compared to the pressure and position dynamics. For all three comparisons, it can be seen how in general the tendency of the simulated response compared to experimental response is similar.

During the validation the parameters from Table 7.2 were varied and it was found that the parameters τ_c and B had limited influence on the responses.

The validation is made with data from a previous student project since there was no access to the laboratory[Vedel et al., 2019]. Ideally, the dynamics should be validated for more piston positions. Furthermore, the relation between the initial pitch angle and piston position are not known exactly. The actual torque and simulated torque will thereby differ. Validation errors could also be caused by deviations in the measured pressures and piston position due to sensor offsets, inaccuracy, and noise. However, these effects are not expected to change the results considerably. The model is derived for control design and testing purposes where the emphasis is put on capturing the system dynamics. As the frequency, damping ratio and natural gain are captured within acceptable margins, the simulation model is considered validated.

Chapter 8

Analysis of Dynamic Model

This chapter contains a linear analysis of the non-linear dynamic model presented in the previous chapter. The analysis is made for the main cylinder, as this is where the SMISMO control strategy is tested. Control for the load cylinder will not be designed since there is no access to the test facilities. Based on the coupling analysis in Chapter 5 there is no significant benefit in choosing either of the analysed control combinations in Table 3.2. *It is therefore chosen to design controllers for piston velocity, $\dot{x}_m$, and the other state to be controlled is either piston side pressure, p_{mp}, or rod side pressure, p_{mr}.*

8.1 Linear Model

The non-linear dynamic model of the main cylinder derived in Equations (7.6) and (7.14) is linearised in order to analyse the system and be able to design linear controllers. The state and input vectors are expressed in Equation (8.1).

$$\mathbf{x} = \begin{bmatrix} \dot{x}_m & p_{mp} & p_{mr} \end{bmatrix}^T \qquad \mathbf{u} = \begin{bmatrix} x_{vmp} & x_{vmr} \end{bmatrix}^T \tag{8.1}$$

It should be noted that the dynamics of the load cylinder are not included and the load force from the load cylinder, F_l, is seen as a disturbance to the linear model. Furthermore, the piston position is not included as a state as described by the end of this section.

The same approach as described in Equations (4.5) and (4.6) is used to derive the linear state space model. The state equation is shown in Equation (8.2).

$$\dot{\mathbf{x}} = \underbrace{\begin{bmatrix} a_{11} & a_{12} & a_{13} \\ a_{21} & a_{22} & 0 \\ a_{31} & 0 & a_{33} \end{bmatrix}}_{\mathbf{A}} \mathbf{x} + \underbrace{\begin{bmatrix} 0 & 0 \\ b_{21} & 0 \\ 0 & b_{32} \end{bmatrix}}_{\mathbf{B}} \mathbf{u} \tag{8.2}$$

The output matrices are determined based on the chosen pairing which is analysed in Section 8.2.1. The linearisation coefficients in the **A** and **B** matrices depend on the linearisation point. The choice of linearisation points is described in Section 8.2. The linear model is validated in Appendix C.5.

The piston position is removed as a state to simplify the analysis by reducing the order of the linear model. To check whether removing piston position as a state affects the dynamics, the state space model is compared to a fourth order state space model where piston position is included as a state. The coefficients varying as a function of the piston position are the volumes, G_m, G_n, G_{m1}, and G_{l1}. The transfer functions are found for $y_1 = p_{mp}$ and $y_2 = \dot{x}_m$, and $u_1 = x_{vmp}$ and $u_2 = x_{vmr}$. The elements of the transfer function matrix without piston position as a state are denoted $g_{11}(s)$, $g_{12}(s)$, $g_{21}(s)$, and $g_{22}(s)$, while the elements of the transfer function matrix with piston position as a state are denoted $h_{11}(s)$, $h_{12}(s)$, $h_{21}(s)$, and $h_{22}(s)$.

The dynamics of the two models are compared for several linearisations points. The bode diagrams are compared to check the difference between gains, phases, damping ratios, and natural frequencies. The bode diagrams for the four elements of each transfer functions matrix are shown in Figure 8.1. Both models are linearised in an equilibrium point, i.e. $\dot{x}_m = 0$, and the other linearisation points are arbitrarily chosen.

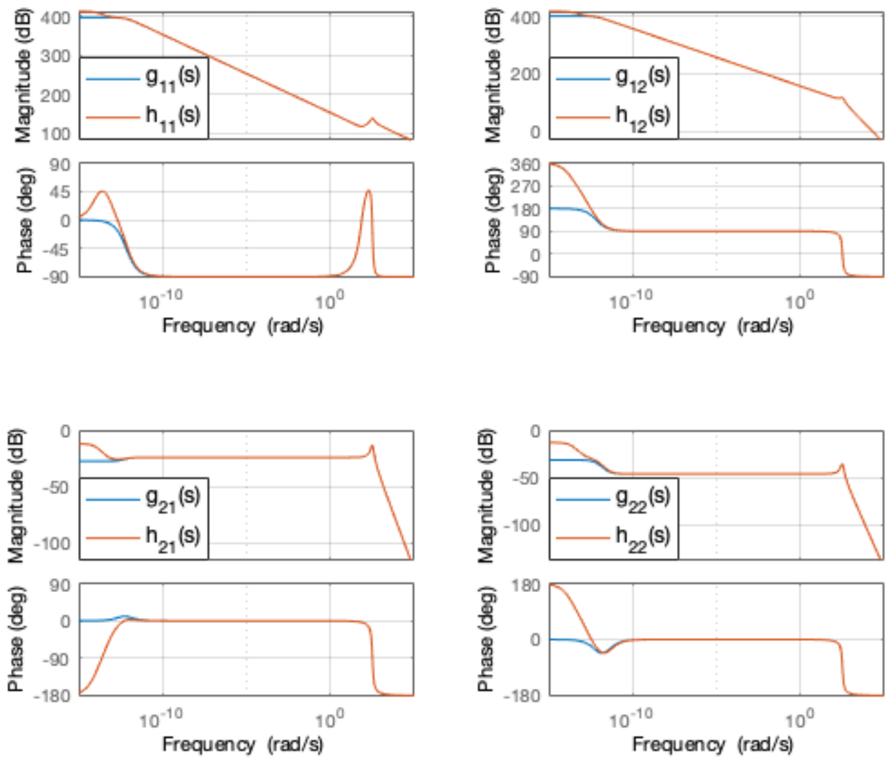

Figure 8.1: Comparison of transfer functions.

In Figure 8.1, it is seen that the transfer functions for the two models are on top for frequencies greater than approximately 10^{-12} [rad/s]. When compared for piston velocities different from zero the same conclusions were seen, where deviations between the third and fourth order models occurred for frequencies up to maximum 10^{-2} [rad/s].

That means the gains and phases are equal above that frequency, and that the damping ratios and natural frequencies are equal. The bode diagrams are plotted for several linearisation points and p_{mr} as output and the same tendency is seen. *It is concluded that the change in parameters varying as a function of the piston position, i.e. the volumes, G_m, G_n, G_{m1}, and G_{l1}, is assumed minimal in the vicinity of the linearisation point. The piston position is therefore not included as a state in the linear model and the system order is reduced.*

8.2 Linearisation Point Analysis

A preliminary control design is proposed in which one linearisation point is chosen based on a worst-case scenario and a linear controller is designed based on the linear model. If controllers are designed such that they perform well under worst-case conditions, then it is expected that they perform well or even better under better conditions. The considered worst-case criteria are: lowest system damping ratio, lowest natural frequency, and system couplings. The choice of linearisation thus becomes a combination between the considered criteria and a trade-off between how much each criterion is weighted. The designed controller is then assumed to ensure system stability in the whole operating domain as this is the most conservative case.

To determine a worst-case scenario, the system stability and dynamics are investigated by calculating the eigenvalues of the system matrix. As the linear model response depends on the chosen operating points, these are varied to determine their influence on system dynamics to conclude on the dynamic change. To linearise the non-linear model, six dependent operating points must be found; piston position, x_m^*, piston velocity, $\dot{x}_m^*$, piston side pressure, p_{mp}^*, rod side pressure, p_{mr}^*, piston side valve opening, x_{vmp}^*, and rod side valve opening, x_{vmr}^*. The three dynamic equations for the system are solved in steady state; Newton's Second Law from Equation (7.14) and two continuity equations from Equation (7.6) i.e. where $\ddot{x}_m = 0$, $\dot{p}_{mp} = 0$, and $\dot{p}_{mr} = 0$. Three operating points should, therefore, be chosen and the remaining three are calculated using the steady state equations.

The system is modelled as a third order system containing two complex poles and one real pole. Figure 8.2 shows the natural frequency and damping ratio of the system poles as a function of the normalised piston position when linearised for three different piston velocities. It should be noted that the complex conjugate poles are far from the origin compared to the real pole.

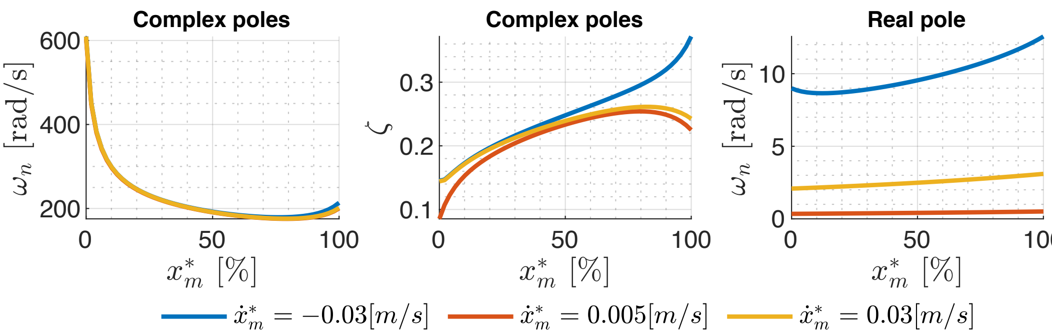

Figure 8.2: Natural frequency and damping ratio of poles for the whole piston stroke length. The arbitrarily chosen linearisation point is $p_{mp}^* = 100$ [bar].

The natural frequency of the complex poles is high for lower piston positions and decreases as the piston position is increased where it is close to constant for stroke lengths above 25 [%]. The damping ratio of the complex poles is lowest for lower piston positions and increases as the piston position increases.

The natural frequency of the real pole increases slightly as the piston position increases and decreases as the magnitude of the velocity linearisation point decreases. The natural frequency of the real pole is lower than the complex poles as it is closer to the origin. The tendency of Figure 8.2 is the same when linearised for various piston side pressures.

A sweep of piston side pressure is shown in Figure 8.3.

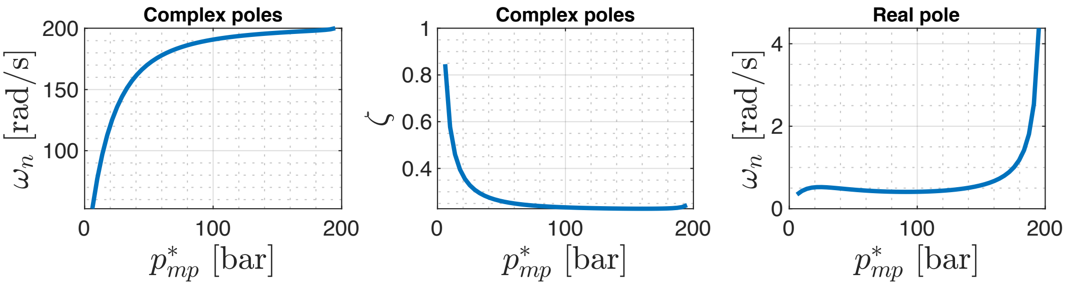

Figure 8.3: Natural frequency and damping ratio of poles when sweeping for all values of p^*_{mp}. The arbitrarily chosen linearisation points are $x^*_m = 50$ [%] and $\dot{x}^*_m = 0.005$ [m/s].

The frequency is increasing and the damping ratio decreasing of the complex poles as the pressure is increased. The natural frequency of the real pole is low in most of the pressure range and increases as the pressure approaches supply pressure. The same tendency is seen when linearised for other piston positions and velocities.

In conclusion, the dynamic change of the linear model is large and very dependent on the chosen linearisation point which is evident from Figures 8.2 and 8.3. The validity of the linear model is therefore limited when considering different operating points.

According to Figure 8.3, p^*_{mp} is chosen as 50 [bar] which is a compromise between low natural frequency and damping ratio. The steady state pressure is then calculated for p^*_{mr}.

The corresponding piston position is calculated based on the coupling analysis presented in Chapter 5 where most coupling occurs. It was concluded from Figure 5.15 that the couplings in the intermediate frequency range can be predicted by calculating the couplings at low frequencies using Equation (5.16) where flows are inputs. Equation (5.21) presented in Chapter 5 where the most coupling occurs is solved for piston position and written in Equation (8.3).

$$\left| \frac{\beta(p_{mr}^*)}{\beta(p_{mp}^*)} \frac{A_{mr}}{A_{mp}} \frac{x_m^*}{L_m - x_m^*} \right| = 1 \rightarrow x_m^* = \frac{\beta(p_{mp}^*)\, A_{mp}\, L_m}{\beta(p_{mp}^*)\, A_{mp} + \beta(p_{mr}^*)\, A_{mr}} \tag{8.3}$$

Based on the chosen pressures, the effective bulk modulus is calculated to find the corresponding piston position where the couplings are most significant. The corresponding piston position calculated becomes 57.5 [%] of stroke length. As a compromise between the calculated piston position and a lower damping ratio for lower piston positions in Figure 8.2, the linearisation point of the piston position is chosen to be 50 [%].

As the piston is expected to follow a trajectory, a piston velocity different from zero is chosen. A small positive piston velocity is arbitrarily chosen as 0.005 [m/s] based on the natural frequency of the real pole in Figure 8.2 which becomes slower when the piston velocity approaches 0 [m/s]. The piston is also expected to move in negative directions, which contradicts the positive velocity linearisation point.

The rod side pressure, piston side valve opening, and rod side valve opening linearisation points are reevaluated for the chosen piston position, velocity, and piston side pressure to get the exact linearisation points in equilibrium. The final linearisation points are shown in Table 8.1.

$x_m^*\,[\%]$	$\dot{x}_m^*\,[m/s]$	$p_{mp}^*\,[bar]$	$p_{mr}^*\,[bar]$	$x_{vmp}^*\,[\%]$	$x_{vmr}^*\,[\%]$
50	0.005	49	83	8	6

Table 8.1: Worst case linearisation points.

The resulting poles are shown in Figure 8.4.

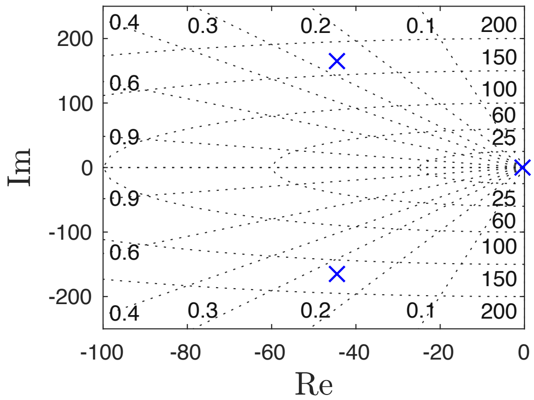

Figure 8.4: The linear model poles when linearising for the worst case scenario linearisation points in Table 8.1

8.2.1 RGA Analysis

In this section, an RGA analysis of the worst-case linearisation point from the previous section is conducted. The pressure is initially chosen as the first output and the velocity as the second as in the RGA analysis in Chapter 5. The RGA element for pairing p_{mp} and $\dot{x}_m$, and for pairing p_{mr} and $\dot{x}_m$ is seen in Figure 8.5.

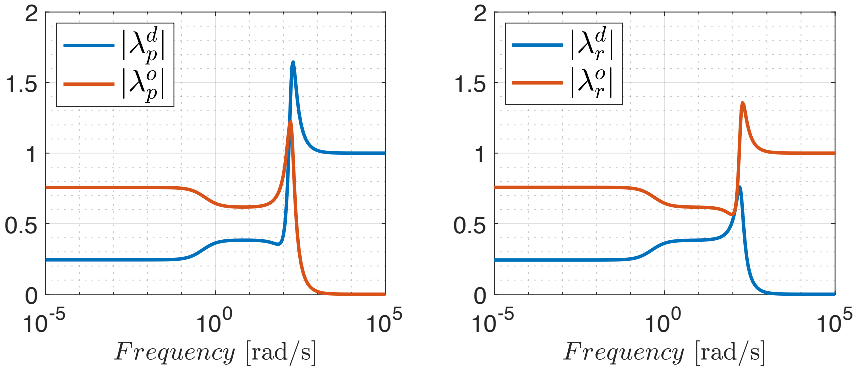

Figure 8.5: RGA elements for the chosen linearisation point.

λ_p^d and λ_p^o refer to the RGA elements with p_{mp} for diagonal and off-diagonal pairing, respectively. λ_r^d and λ_r^o refer to the RGA elements with p_{mr} for diagonal and off-diagonal pairing, respectively. The coupling is significant at intermediate frequencies around 10 [rad/s] as the linearisation point was chosen close to the piston position and pressures resulting in most coupling. It is chosen to pair for the RGA element closest to 1 at frequencies below the natural frequency. Since the off-diagonal is closest to 1 at frequencies below the natural frequency when pairing with either p_{mp} or p_{mr}, the chosen output vectors become:

$$\mathbf{y}_p = [\dot{x}_m \;\; p_{mp}]^T \tag{8.4}$$
$$\mathbf{y}_r = [\dot{x}_m \;\; p_{mr}]^T \tag{8.5}$$

8.2.2 Scaled State Space Model

A scaled model is needed for the singular value decomposition analysis in Section 8.3 since the singular values depend on the scaling. In Equation (8.6), the scaled transfer function matrices, $\mathbf{G}_{p,s}$ and $\mathbf{G}_{r,s}$, are presented [Skogestad and Postlethwaite, 2005, 5-6].

$$\begin{aligned}
\mathbf{G}_{p,s} &= \mathbf{M}_{py}^{-1}\mathbf{G}_p\mathbf{M}_u \\
\mathbf{G}_{r,s} &= \mathbf{M}_{ry}^{-1}\mathbf{G}_r\mathbf{M}_u
\end{aligned} \tag{8.6}$$

$\mathbf{G}_p$ and $\mathbf{G}_r$ are the unscaled transfer function matrices. $\mathbf{M}_{py}$, $\mathbf{M}_{ry}$, and $\mathbf{M}_u$ are the diagonal scaling matrices shown in Equations (8.7) and (8.8) which contain the largest allowed control outputs, $\dot{x}_{m,max}$, $p_{mp,max}$, and $p_{mr,max}$, and the largest system inputs, $x_{vmp,max}$ and $x_{vmr,max}$.

$$\mathbf{M}_{py} = \begin{bmatrix} \dot{x}_{m,max} & 0 \\ 0 & p_{mp,max} \end{bmatrix} \qquad \mathbf{M}_{ry} = \begin{bmatrix} \dot{x}_{m,max} & 0 \\ 0 & p_{mr,max} \end{bmatrix} \tag{8.7}$$

$$\mathbf{M}_u = \begin{bmatrix} x_{vmp,max} & 0 \\ 0 & x_{vmr,max} \end{bmatrix} = \mathbf{I} \tag{8.8}$$

The maximum piston- and rod side pressures are chosen to be the pump pressure. The maximum velocity is calculated based on the orifice and continuity equations in steady state. The valve is fully opened, and the pressure drop across the valve is the difference between maximum and minimum system pressures. For the piston side flow, the calculation of maximum velocity is shown in Equation (8.9) where the compression flow is assumed negligible.

$$\begin{aligned}
Q_{mp,max} &= k_{vm}\sqrt{p_s - p_{mp}}, \qquad p_{mp} = p_t \\
\dot{x}_{m,max} &= \frac{Q_{mp,max}}{A_{mp}}
\end{aligned} \tag{8.9}$$

The maximum velocity in steady state is limited by the piston side flow since $A_{mp} > A_{mr}$. The maximum parameters are shown in Table 8.2.

Parameter	**Value**	**Unit**
$p_{mp,max}$	200	[bar]
$p_{mr,max}$	200	[bar]
$\dot{x}_{m,max}$	0.0744	[m/s]

Table 8.2: Maximum values used to normalise the state space model.

8.3 Singular Value Decomposition

The variation of the system gain is analysed in this section using Singular Value Decomposition, SVD. The gain of a MIMO system can be calculated using the 2-norm as shown in Equation (8.10).

$$\frac{||y(\omega)||_2}{||u(\omega)||_2} = \frac{||G_s(j\omega)\, u(\omega)||_2}{||u(\omega)||_2} \tag{8.10}$$

The gain is independent of the input magnitude, $||u(j\omega)||_2$, but it depends on the frequency, ω, and the direction of the input vector[Skogestad and Postlethwaite, 2005, p. 73]. The minimum and maximum gains when varying the direction of the input vector are the minimum and maximum singular values, i.e. $\underline{\sigma}$ and $\overline{\sigma}$, respectively. The scaled transfer function matrix, $\mathbf{G}_s$, can be decomposed using singular value decomposition as shown in Equation (8.11) where ^{H} denotes the complex conjugate transpose[Skogestad and Postlethwaite, 2005, p. 76].

$$\mathbf{G}_s = \mathbf{U}\,\mathbf{\Sigma}\,\mathbf{V}^H \tag{8.11}$$

where $\mathbf{\Sigma}$ is a matrix containing non-negative singular values, σ, along its main diagonal, and $\mathbf{U}$ and $\mathbf{V}$ are unitary matrices of output and input singular vectors, respectively[Skogestad and Postlethwaite, 2005, p. 76]. The minimum and maximum singular values are expressed in Equation (8.12), where λ_{min} and λ_{max} are the minimum and maximum eigenvalues, respectively[Skogestad and Postlethwaite, 2005, p. 76].

$$\underline{\sigma} = \sqrt{\lambda_{min}(\mathbf{G}_s^H \mathbf{G}_s)}, \qquad \overline{\sigma} = \sqrt{\lambda_{max}(\mathbf{G}_s^H \mathbf{G}_s)} \tag{8.12}$$

The condition number, γ, is defined as the ratio between the maximum and minimum singular values as shown in Equation (8.13)[Skogestad and Postlethwaite, 2005, p. 82].

$$\gamma = \frac{\overline{\sigma}}{\underline{\sigma}} \tag{8.13}$$

A large condition number indicates that the directional dependency is strong and the system is said to be ill-conditioned. The scaled transfer function matrix described in

Section 8.2.2 is used to calculate the singular values as the condition number depends on the scaling of the system[Skogestad and Postlethwaite, 2005, p. 82].

The minimum and maximum singular values for the system are plotted in Figure 8.6. $\overline{\sigma}_p$ and $\underline{\sigma}_p$ are maximum and minimum singular values when the outputs are $y_1 = \dot{x}_m$ and $y_2 = p_p$, and $\overline{\sigma}_r$ and $\underline{\sigma}_r$ are maximum and minimum singular values when the outputs are $y_1 = \dot{x}_m$ and $y_2 = p_r$.

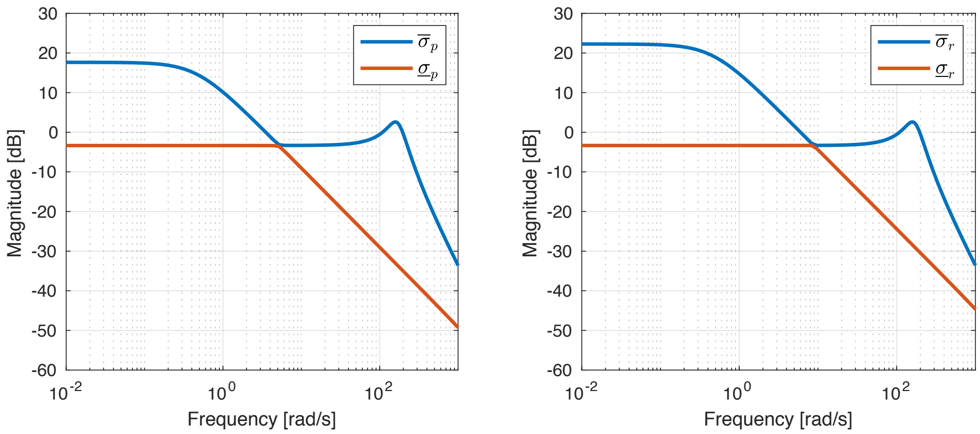

Figure 8.6: Minimum and maximum singular values. The left plot is for p_p as second output, and the right plot is for p_r as second output.

It is seen in Figure 8.6 that for low frequencies $\overline{\sigma}_p \gg \underline{\sigma}_p$ and $\overline{\sigma}_r \gg \underline{\sigma}_r$. As the frequency increases, both set of minimum and maximum singular values approach each other up to a frequency around $5-9$ [rad/s] where the maximum and minimum singular values are closest. The ratios between the maximum and minimum singular values increase as the frequency further increases up to the point where $\overline{\sigma}_p$ and $\overline{\sigma}_r$ peak. The condition numbers, γ_p and γ_r, are plotted in Figure 8.7.

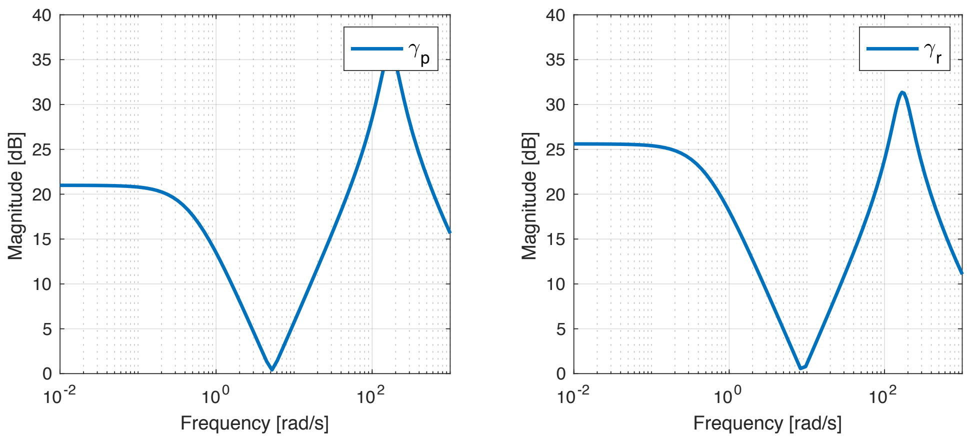

Figure 8.7: Condition numbers. The left plot is for p_p as second output, and the right plot is for p_r as second output.

The same tendency is seen for the condition numbers as for the maximum and minimum singular values. At low frequencies, both condition numbers are approximately constant and start to decrease as the frequency increases. γ_p approaches 1 around 5 [rad/s] and γ_r approaches 1 around 9 [rad/s]. Both condition numbers increase as the frequency further increases and peak at around 180 [rad/s]. That means the system has a strong directionality as the system gain varies with the direction of the input vector. A large condition number may indicate control problems, however, a small value of $\underline{\sigma}$ is generally not desirable which is not necessarily the case for a large value of $\overline{\sigma}$. Both condition numbers are large and $\underline{\sigma}_p$ and $\underline{\sigma}_r$ are small at a frequency around 180 [rad/s] which is also close to the frequency at which the RGA elements peak as shown in Figure 8.5. This may indicate control problems[Skogestad and Postlethwaite, 2005, p. 82]. *It is concluded that as the couplings are significant around the natural frequency and the system is ill-conditioned, a decoupling pre-compensator or MIMO controllers should be designed.*

Chapter 9

Control

In this chapter, the controllers are designed based on the analysis of the dynamic model. The control objective is presented in the first section followed by the control strategy.

9.1 Control Objective

Characteristics for control systems are stability, disturbance rejection, sensitivity, steady state error, transient response, and closed loop frequency response [Philips and Parr, 2013, p. 175]. In regards to stability, the closed loop poles are placed in the left half s-plane and the system is considered stable if the reference tracking error does not blow up. The controller must, furthermore, maintain system stability when disturbances from, e.g. the load force, are applied. In regards to sensitivity, it is important to analyse the sensitivity of the control system to parameter variations as the model is not an exact representation of the physical system. In addition, it is desired to minimise the steady state error for both the velocity and pressure control. This is evaluated on a stepped and ramped reference. The transient response is evaluated on a stepped reference, where it is desired to minimise the rise time and settling time while having a low or no overshoot. Finally, the closed loop frequency response is evaluated at a sinusoidal reference and with a wide frequency range reference. The controllers will be designed by taking into account the explained characteristics of a control system.

The control of the velocity and pressure are weighted equally during controller design to limit the possible control options. As an example; the reference for the pressure will not be made based on the velocity reference to reduce the tracking error of the velocity. The references are designed independently of each other. Making a reference based on the other reference could, however, improve the tracking. *The overall control objective is to minimise the tracking error for both the velocity and pressure during the different references.*

The piston velocity is one of the states to be controlled, however, it is not measured in the experimental setup. Knowledge of the velocity is, therefore, necessary if a reference is to be followed. Several techniques for state estimation of unmeasured states based on measured states exist[Skogestad and Postlethwaite, 2005, 346-348] or alternatively computing the derivative of the position measurement. *As the purpose is to test control strategies and the results are purely simulation-based, the velocity is assumed to be measured.*

It is chosen not to change the direction of the load force during reference tracking. A change in the direction of the load force changes which pressure is to be controlled. As the direction of the load force is not changed, the same controller is used and switching between controllers during reference tracking is not considered. *The controllers are designed for velocity and rod side pressure. The same controllers are used for velocity and piston side pressure if the response is satisfactory. As a final remark, the controllers are designed for the unscaled model.*

9.2 Control Strategy

In this section, several relevant control strategies are studied which account for the strong directional dependency of the input vector, and the cross couplings as it was earlier found that the couplings are significant when varying operating parameters. As a starting point, a controller is chosen and designed. Other controllers will hereafter be designed to improve the reference tracking.

Classical SISO Control Methods with Decoupling Pre-compensator

Classical SISO control methods include proportional, integral, and differential controllers as well as lag and lead controllers. These controllers are in general simple and have proven robustness as the resultant closed loop system tends to be insensitive to small model inaccuracies.[Philips and Parr, 2013, p. 449] Transient and steady state responses can be improved depending on the choice of controllers. To avoid significant cross couplings when dealing with MIMO systems, a decoupling pre-compensator should be designed and implemented along with the SISO controllers. A decoupling pre-compensator is based on the system model which means it requires an accurate model.[Skogestad and Postlethwaite, 2005, p. 92]

Pole Placement Control Methods

Pole placement methods offer a more complete control by meeting a larger number of specifications than classical SISO methods. Pole placement depends on having an accurate model.[Philips and Parr, 2013, p. 449] Full state feedback requires all states to be measured. The states are assumed measurable since the controllers performance are only simulated.

Optimal Control Methods

Optimal control methods include, among others, LQR which is comparable to a pole placement method. LQR search to reach the reference as fast as possible without aggressive input values while maintaining good stability margins.[Skogestad and Postlethwaite, 2005, p. 349] An extension to LQR is LQI where integrators are implemented to improve the steady state accuracy[Philips and Parr, 2013, p. 486].

Besides the above-mentioned control methods, there exist several other linear control methods along with non-linear control methods. It is chosen to design MIMO controllers using pole placement as this allows closed loop poles to be placed in desired locations. If the controllers do not satisfy the desired performance, other MIMO controllers will be designed based on the achieved performance.

9.3 Pole Placement Control

In this section, controllers are designed using the pole placement method. All states are assumed measurable which means full state feedback is utilised. The notation for time dependence e.g. $x(t)$ is omitted for the remainder of this chapter for ease of reading such $x(t) = x$. To check whether the system is controllable, the controllability matrix for a third order system is expressed in Equation (9.1)[Philips and Parr, 2013, p. 477-478].

$$\mathbf{C}_o = \begin{bmatrix} \mathbf{B} & \mathbf{A}\,\mathbf{B} & \mathbf{A}^2\,\mathbf{B} \end{bmatrix} \tag{9.1}$$

The system is completely controllable since $rank(\mathbf{C}_o) = 3$ for all linearisation points [Brogan, 1991, p. 377-378]. As the system is completely controllable, any set of desired closed loop poles can be achieved by a constant feedback gain matrix $\mathbf{K}_{PP}$[Brogan, 1991, p. 448].

Pole placement design allows all closed loop poles to be placed in desirable locations. The desirable pole locations are found by choosing the desired dynamics of the closed loop system. As mentioned earlier, the uncompensated system consists of a complex conjugate pole pair and a real pole hence the system is a combination of a first and a second order system. The desirable pole locations, λ_1, λ_2, and λ_3, are found by solving the characteristic equations for a first and second order system as shown in Equation (9.2)[Philips and Parr, 2013, p. 137-140].

$$
\begin{aligned}
\tau s + 1 = 0 \quad &\rightarrow \quad \lambda_1 = -\frac{1}{\tau} \\
s^2 + 2\,\zeta\,\omega_n\,s + \omega_n^2 = 0 \quad &\rightarrow \quad \lambda_2, \lambda_3 = -\,\zeta\,\omega_n \pm j\omega_n\sqrt{1-\zeta^2}
\end{aligned}
\tag{9.2}
$$

The system input for a full state feedback controller is expressed in Equation (9.3) for a non-zero set point[Brogan, 1991, p. 443-445].

$$
\mathbf{u} = -\mathbf{K}_{PP}\,\mathbf{x} + \mathbf{F}\,\mathbf{r} \tag{9.3}
$$

Where $\mathbf{r}$ is the reference vector, $\mathbf{K}_{PP}$ is the feedback gain matrix, and $\mathbf{F}$ is a pre-compensator and is defined in Equation (9.4). It should be noted that $\mathbf{r}$ is a 2x1 column vector, $\mathbf{K}_{PP}$ is a 2x3 matrix, and $\mathbf{F}$ is a 2x2 matrix.

$$
\mathbf{F} = -\left[\mathbf{C}(\mathbf{A} - \mathbf{B}\,\mathbf{K}_{PP})^{-1}\mathbf{B}\right]^{-1} \tag{9.4}
$$

$\mathbf{F}$ is the inverse of the closed loop system gain and is found by evaluating the linear model in steady state when the outputs are equal to the references. That ensures zero steady state error in the linearisation point for the linear model. A general block diagram for a linear system with full state feedback control is shown in Figure 9.1.

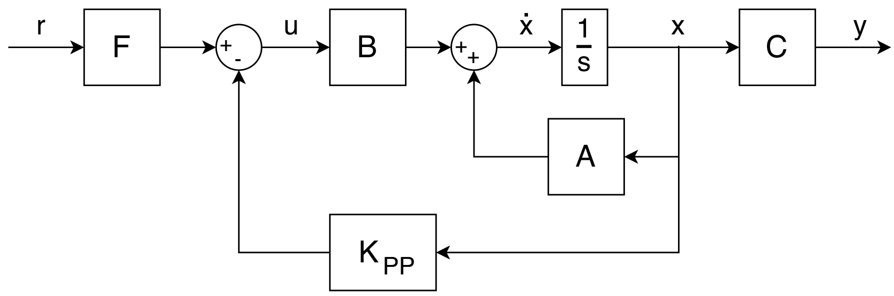

Figure 9.1: Simple block diagram of the controlled system using pole placement.

Where $\mathbf{u} = [x_{vmp} \quad x_{vmr}]^T$ and $\mathbf{x} = [\dot{x}_m \quad p_{mp} \quad p_{mr}]^T$. $\mathbf{y}$ changes depending on which pressure to control. The feedback gain matrix $\mathbf{K}_{PP}$ is found by comparing the closed loop system dynamics with the desired dynamics. However, as it results in an underdetermined system of linear equations, an infinite number of solutions exist for the feedback gain matrix $\mathbf{K}_{PP}$.

A way to get all solutions of the $\mathbf{K}_{PP}$ matrix is by using the method described in [Brogan, 1991]. The deviation of the feedback gain matrix $\mathbf{K}_{PP}$ is included in

Appendix D.1. It is found that the feedback gain matrix $\mathbf{K}_{PP}$ is a function of the six parameters: α_1, α_2, α_3, β_1, β_2, and β_3. This allows the possibility to set up constraints to find a unique solution for $\mathbf{K}_{PP}$. This process has not been included as it is not the focus of this thesis. Instead, the command *place* in MATLAB is used to choose a feedback gain matrix $\mathbf{K}_{PP}$. This command defines constraints to find a solution that minimises the sensitivity to perturbations to get a robust solution[MathWorks, 2020].

9.3.1 Design of Pole Placement Control

The desired closed loop poles were located at $\omega_n = 125$ [rad/s] and $\zeta = 0.7$ for the complex poles and $\tau = 0.1$ [s] for the real pole. This was to increase the system damping where a damping ratio of $\zeta = 0.7$ achieves a combination of fast rise time and small overshoot[Philips and Parr, 2013, p. 141]. A faster response is furthermore achieved by moving the real pole further from the origin. The error between references and outputs increased when changing the location of the complex conjugate pole pair. The increased error was caused by large control signals when moving the closed loop poles away from the open loop system poles. The complex conjugate poles were placed close to the open loop poles instead, however, with increased damping. The real pole was moved along the negative real axis by changing τ. The location of the closed loop eigenvalues was observed to be highly limited by the valve dynamics. The smallest errors were obtained at the final locations in Table 9.1 where piston side pressure and rod side pressure refer to the pressure which is being controlled.

	Uncompensated system	**Piston side pressure**	**Rod side pressure**
λ_1	-0.464	-10	-20
λ_2	$-44.5 + j165$	$-45 + j143$	$-45 + j143$
λ_3	$-44.5 - j165$	$-45 - j143$	$-45 - j143$

Table 9.1: Locations of eigenvalues for the uncompensated system and with state feedback control.

The final locations correspond to $\zeta = 0.3$ and $\omega_n = 150$ [rad/s] for the second order system, $\tau = 0.1$ [s] for piston side pressure control and $\tau = 0.05$ [s] for rod side pressure control for the first order system according to Equation (9.2). The locations of the eigenvalues are plotted in Figure 9.2 along with the location of the valve eigenvalues.

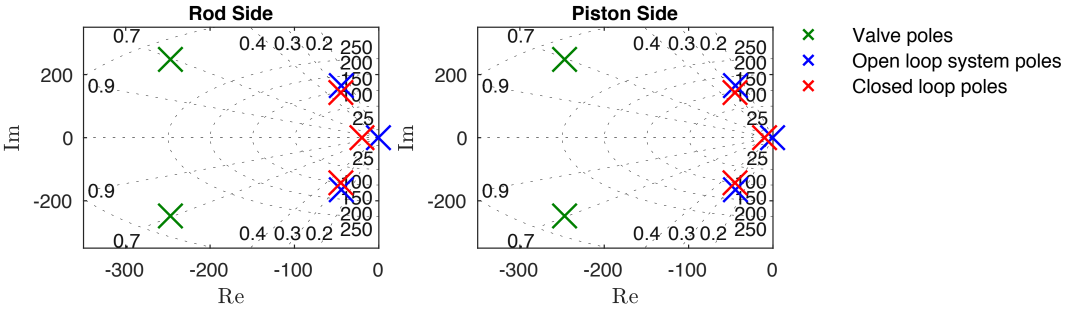

Figure 9.2: Valve eigenvalues, open loop system eigenvalues and closed loop poles for rod side and piston side pressure control.

The closed loop poles have been computed as a function of the piston position stroke length by calculating the eigenvalues for the closed loop system using the same feedback gain matrix, $\mathbf{K}_{PP}$, obtained by pole placement. The non-linear model is linearised for each piston position while using the worst-case linearisation points. The corresponding eigenvalues are then found for each closed loop system matrix, $\mathbf{A}_{cl} = \mathbf{A} - \mathbf{B}\,\mathbf{K}_{PP}$, by updating $\mathbf{A}$ and $\mathbf{B}$ according to the linearised piston position. The eigenvalues for the closed loop system as a function of piston position are shown in Figure 9.3, where the eigenvalues are coloured to distinguish between linearised piston positions and the red dashed line shows the estimated natural frequency of the valve.

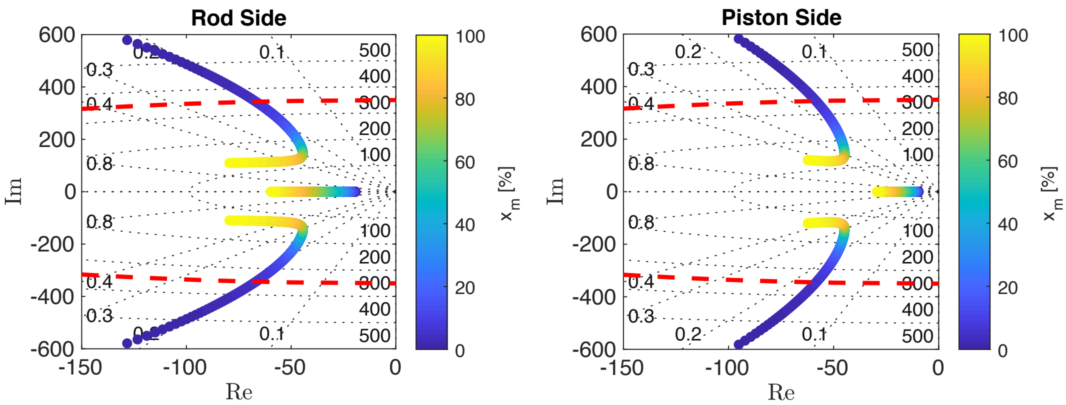

Figure 9.3: Closed loop pole trace when linearised as a function of the piston position using a constant feedback gain matrix obtained by pole placement. The red dashed line shows the natural frequency of the valve.

For lower piston positions the feedback gains found by pole placement move the complex conjugate closed loop poles outside of the valves operating frequency however for most of the piston stroke length, the closed loop poles are below the frequency. The high-frequency control effort is therefore expected to be filtered by the valve dynamics as the closed loop frequency in the lower positions is dictated by the actuating frequency of the valve. Furthermore, it is expected that the closed loop response is dominated by the real pole which moves away from the origin as the piston position is increased. It should be noted that the pole locations in Figure 9.3 are only valid for the linear model for the specific operating points, i.e. velocity, pressures, and valve openings.

The step response when controlling the rod side pressure is now analysed. The compensated response is compared to the uncompensated to determine if the controllers improve the response, as the closed loop poles and open loop poles are relatively close to each other. The step tests are performed in the linear model to leave out any effects caused by non-linearities. The linear model is linearised in the worst-case linearisation point and the velocity reference is stepped, while the rod side pressure reference is constant. The velocity, rod side pressure and valve control effort can be seen in Figure 9.4 when compensated and uncompensated. A pre-compensator, **F**, is calculated for the open loop system as well to be able to compare the uncompensated system with the compensated system.

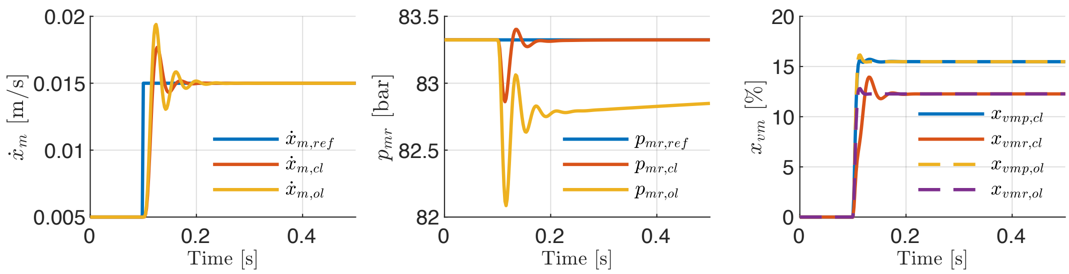

Figure 9.4: Piston velocity, rod side pressure and control effort comparison of open loop and closed loop response in the linear model.

It can be seen that the response for both velocity and pressure improved when closed loop controlled. Both have less overshoot and a more damped response. The settling time is improved for both responses especially the pressure which decreased from a settling time of approximately 8 [s] to approximately 0.1 [s]. It can furthermore be seen that the control effort does not saturate.

Both pressure and velocity responses improved when tested in the particular linear model, however, as it was previously concluded from the linear analysis that the dynamics change depending on operating point, the closed loop step response is tested for the linear model when linearised in three different piston positions. This is to determine how the response varies for different operating points. The step responses for a velocity reference and a constant rod side pressure reference can be seen in Figure 9.5 when tested in the linear model which is linearised in 10, 50 and

90 [%] of total stroke length.

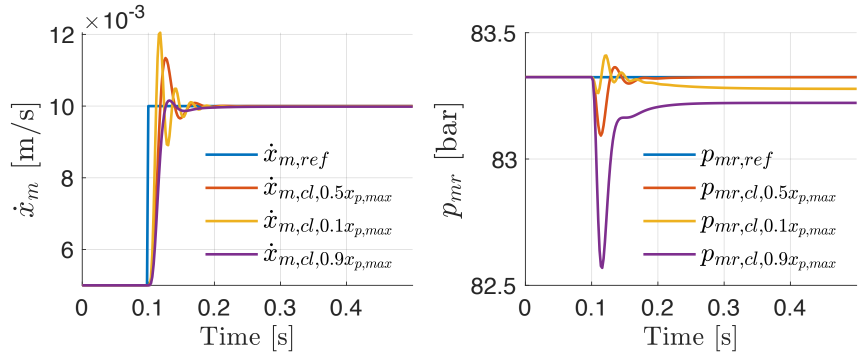

Figure 9.5: Closed loop response of velocity and pressure when tested on the linear model in three different piston positions: 10, 50 and 90 [%] of maximum stroke length.

It can be seen that the response do change when tested in other operating points. The velocity response shows a larger overshoot in the lower piston position, while the response seems improved further for the larger piston positions. The opposite is seen for the rod side pressure tracking, where a large spike happens in the larger position while the response improved in lower piston position. Furthermore, a steady state error occurs on both velocity and pressure.

During the design process, it was found that the closed loop system dynamics change significantly for small changes in the location of the complex conjugate pole pair. The dynamics changed when varying the piston position. It was also shown in Figure 8.2 in Section 8.2 that the location of the poles changes when varying the linearisation point. That means if the poles are placed at the same location regardless of the linearisation point it might result in high control signals in the domain where the closed loop poles are far away from the open loop poles. A way to improve the dynamics in the whole working domain is by implementing gain scheduling. The non-linear model is then linearised depending on the operating point and the controller gains are found for each operating point and updated real-time. By implementing a Linear Quadratic Regulator, LQR, it is not necessary to place the poles but instead tune the penalty matrices $\mathbf{Q}$ and $\mathbf{R}$. The LQR control approach with gain scheduling is described in the following section.

9.4 Linear Quadratic Regulator

Linear Quadratic Regulator, LQR, control with gain scheduling is chosen to improve the response compared to the pole placement method. The implementation is identical to the pole placement, i.e. full state feedback with a pre-compensator, and only the feedback and pre-compensator gains will be updated according to the piston position. The implementation is shown in Figure 9.6.

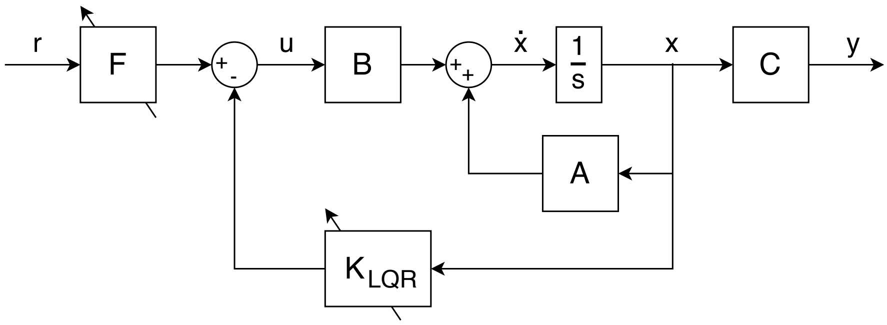

Figure 9.6: Simple block diagram of the controlled system using LQR with gain scheduling.

The arrows in Figure 9.6 indicate that $\mathbf{F}$ and $\mathbf{K}_{LQR}$ are varied as a function of the piston position. As a non-zero set point is desired the control law becomes as shown in Equation (9.5)[Brogan, 1991, p. 443-445].

$$\mathbf{u} = -\mathbf{K}_{LQR}\,\mathbf{x} + \mathbf{F}\,\mathbf{r} \tag{9.5}$$

where $\mathbf{F}$ is the inverse closed loop DC-gain and shown in Equation (9.6).

$$\mathbf{F} = -\left[\mathbf{C}(\mathbf{A} - \mathbf{B}\,\mathbf{K}_{LQR})^{-1}\mathbf{B}\right]^{-1} \tag{9.6}$$

The optimal feedback gain matrix, $\mathbf{K}_{LQR}$, is expressed in Equation (9.7).[Skogestad and Postlethwaite, 2005, p. 346]

$$\mathbf{K}_{LQR} = \mathbf{R}^{-1}\,\mathbf{B}^T\,\mathbf{P} \tag{9.7}$$

where $\mathbf{P} = \mathbf{P}^T \geq 0$ is the unique positive semi-definite solution of the Riccati equation in Equation (9.8).[Skogestad and Postlethwaite, 2005, p. 346]

$$\mathbf{A}^T\,\mathbf{P} + \mathbf{P}\,\mathbf{A} - \mathbf{P}\,\mathbf{B}\,\mathbf{R}^{-1}\,\mathbf{B}^T\,\mathbf{P} + \mathbf{Q} = \mathbf{0} \tag{9.8}$$

Q and **R** are penalty matrices which are to be chosen. **Q** is a positive semi-definite diagonal matrix, $\mathbf{Q} = \mathbf{Q}^T \geq 0$, and **R** is a positive definite diagonal matrix, $\mathbf{R} = \mathbf{R}^T > 0$. The control gain calculated by Equations (9.7) and (9.8) minimises the quadratic cost function in Equation (9.9). [Skogestad and Postlethwaite, 2005, p. 346]

$$J_r = \int_0^\infty [\mathbf{x}^T\mathbf{Q}\mathbf{x} + \mathbf{u}^T\mathbf{R}\mathbf{u}]\, dt \tag{9.9}$$

It seen from Equation (9.9) that **Q** relates to the response of the states, **x**, and **R** relates to the control signals, **u**. The advantage of using the LQR algorithm for finding the feedback gain lies in the ability to weigh both the state response and control signals. Based on the chosen weight matrices **Q** and **R**, the gain matrix $\mathbf{K}_{LQR}$ can be found which satisfies the desired closed loop response and magnitude of control signals.

A gain scheduling strategy is utilised to decrease the steady state error seen during the pole placement design, and furthermore compensate for the varying piston position which were seen in Figure 9.5. The non-linear model is therefore linearised as a function of piston position, and the feedback gain matrix, $\mathbf{K}_{LQR}$, and pre-compensator, **F**, are recomputed for the varying system and input matrices while the weight matrices are kept constant. To get smooth functions and avoid unwanted dynamics for $\mathbf{K}_{LQR}$ and **F**, the points are linearly interpolated with a step size of 1 [%] of the stroke length.

9.4.1 Design of LQR Control

As a starting point for determining the weight matrices, Bryson's rule is used which normalises the control variables and inputs as shown in Equation (9.10).[Johansen, 2019]

$$\begin{aligned} \mathbf{Q}(i,i) &= \frac{1}{e_{i,max}^2} \quad i \in [1,2,3] \\ \mathbf{R}(j,j) &= \frac{1}{u_{j,max}^2} \quad j \in [1,2] \end{aligned} \tag{9.10}$$

Where $e_{i,max}$ and $u_{j,max}$ are the maximum deviation of the controlled states and control inputs, respectively. Bryson's rule is used as a starting point for an iterative process using the simulation while changing the diagonal entries of **Q** and **R** until a satisfactory response in achieved. The weight matrices, **Q** and **R**, have been determined based on the worst-case linearisation point which was found in Section 8.2.

The input weight matrix, **R**, is increased from the normalised value to penalise large control inputs which had a stabilising effect when a load force was applied however at the cost of slower response. The entry of **Q** corresponding to the weight of the velocity error is decreased as that resulted in a satisfactory response however the entries were increased for the pressures to obtain better reference tracking. Controlling the rod side or the piston side pressures yielded satisfactory results using the same feedback gain and pre-compensator gain matrix.

The location of the uncompensated open loop poles and compensated closed loop poles as a function of the piston position are shown in Figure 9.7.

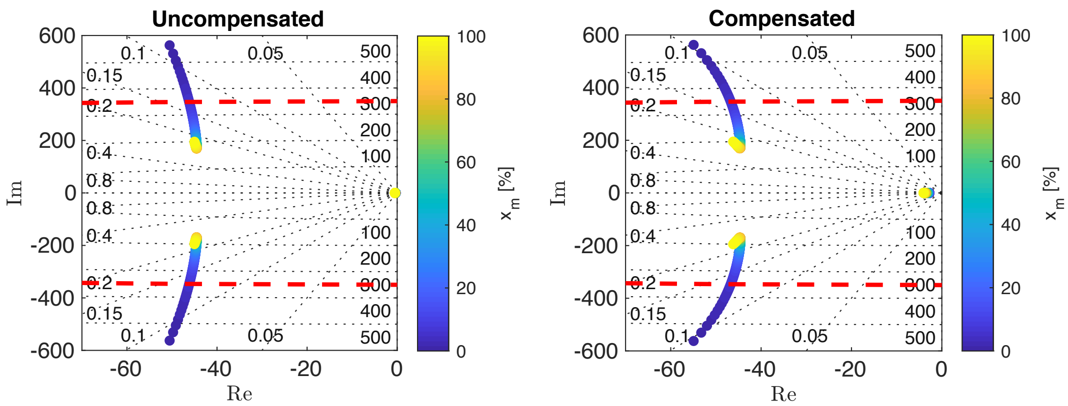

Figure 9.7: Uncompensated system when linearised for the whole piston stroke length, and compensated system when the gains are updated as a function of piston position. The red dashed line shows the natural frequency of the valves.

The compensated poles have been placed close to the uncompensated. The real pole of the compensated system is however increased compared to the uncompensated. Furthermore, at lower piston positions, the complex conjugate pole pair exceeds the natural frequency of the valve. The control effort containing frequency content above the natural frequency of the valve is therefore mitigated due to the physical limitation of the valve as for pole placement. As the pole location of the compensated system is close to the uncompensated, the step responses are compared. The purpose is to determine whether the compensated system has been shaped any different than the uncompensated and conclude on whether open loop control would yield a similar and satisfactory response. The responses of velocity, rod side pressure, and control effort are seen in Figure 9.9.

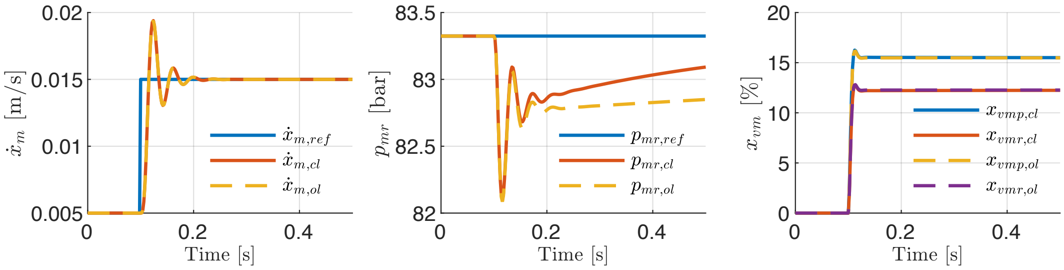

Figure 9.8: Piston velocity, rod side pressure, and control effort comparison of open loop and closed loop response in the linear model.

The velocity response is close to identical when comparing the compensated and uncompensated responses. The pressure response is similar however a settling time of approximately 2 [s] is achieved compared to 8 [s] when open loop controlled. A slight improvement is expected as the real pole is moved further away from the origin for the compensated pole map in Figure 9.7. The valve responses are very similar and do not saturate. While the pressure response improved when closed loop controlled, both pressure and velocity are oscillatory with a large overshoot.

The benefit in choosing gain scheduling lies in achieving the desired response even when operating conditions change. As the closed loop response did improve compared to open loop and to analyse the effects of change in operating conditions, the closed loop response is shown when tested on the linear model in three piston positions. The velocity and rod side pressure response is shown in Figure 9.9.

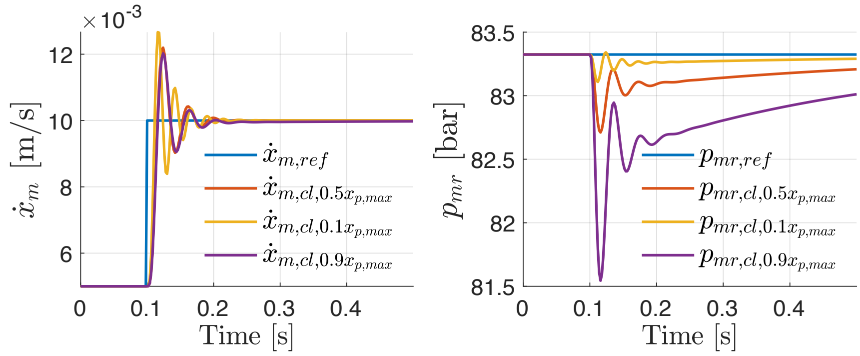

Figure 9.9: Closed loop response of velocity and pressure when tested on the linear model in three different piston positions: 10, 50 and 90 [%] of maximum stroke length.

Both the velocity and pressure responses are oscillatory with large overshoot. This is also evident from the pole map in Figure 9.7 where the largest damping ratio is approximately $\zeta = 0.3$ for the complex conjugate pole pair. There is no improvement in the transient response compared to pole placement, however, the steady state error for both velocity and rod side pressure has been eliminated although not evident in Figure 9.9.

As the steady state error depends on operating points and these are expected to vary in the non-linear model, an integrator is added to the control structure in the next section to guarantee no steady state error during steps, independently of the operating point. This is furthermore to improve the steady state error when operating conditions are changed due to a disturbance. The controller gains will be found using optimal quadratic theory. The controller thus becomes a Linear Quadratic Integral controller, which will be described in the following section.

9.5 Linear Quadratic Integral Control

Linear Quadratic Integral, LQI, control is implemented to remove steady state errors on velocity and pressure during step references by increasing from a system type 0 to a system type 1[Philips and Parr, 2013, p. 199]. An integrator for both the velocity and pressure is implemented as the velocity and pressure control are weighted equally. The system is augmented by introducing two error states defined in Equation (9.11).[Johansen, 2019]

$$\dot{\mathbf{z}} = \begin{bmatrix} \dot{x}_{m,ref} - \dot{x}_m \\ p_{m,ref} - p_m \end{bmatrix} = \mathbf{r} - \mathbf{C}\,\mathbf{x} \tag{9.11}$$

where the pressure error state is either piston or rod side pressure depending on which is controlled. The augmented state space model is shown in Equation (9.12) and the corresponding block diagram in Figure 9.10.[Johansen, 2019]

$$\begin{aligned} \begin{bmatrix} \dot{\mathbf{x}} \\ \dot{\mathbf{z}} \end{bmatrix} &= \overbrace{\begin{bmatrix} \mathbf{A} & \mathbf{0} \\ -\mathbf{C} & \mathbf{0} \end{bmatrix}}^{\mathbf{A}_a} \overbrace{\begin{bmatrix} \mathbf{x} \\ \mathbf{z} \end{bmatrix}}^{\mathbf{x}_a} + \overbrace{\begin{bmatrix} \mathbf{B} \\ \mathbf{0} \end{bmatrix}}^{\mathbf{B}_a} \mathbf{u} + \begin{bmatrix} \mathbf{0} \\ \mathbf{I} \end{bmatrix} \mathbf{r} \\ \mathbf{y} &= \underbrace{\begin{bmatrix} \mathbf{C} & \mathbf{0} \end{bmatrix}}_{\mathbf{C}_a} \begin{bmatrix} \mathbf{x} \\ \mathbf{z} \end{bmatrix} \end{aligned} \tag{9.12}$$

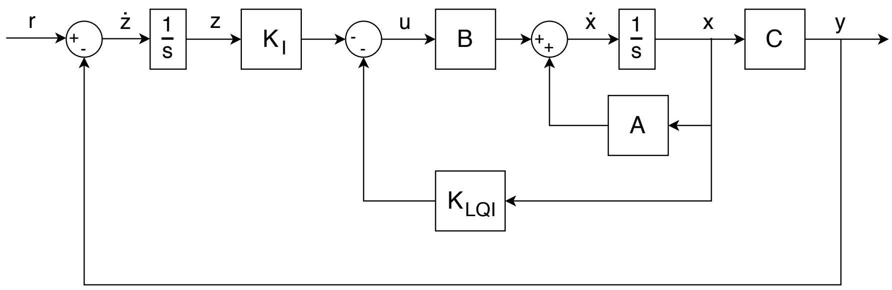

Figure 9.10: Simple block diagram of the controlled system using LQI control.

It should be noted that in addition to state feedback, an outer loop controls the output which is not the case for pole placement and LQR. The LQI controller thereby acts on the error between the reference and output. The control law is expressed in Equation (9.13).[Johansen, 2019]

$$\mathbf{u} = -\mathbf{K}_a\,\mathbf{x}_a \tag{9.13}$$

where $\mathbf{K}_a = [\mathbf{K}_{LQI} \;\; \mathbf{K}_I]$ and the gain matrices $\mathbf{K}_{LQI}$ and $\mathbf{K}_I$ are determined using the optimal quadratic theory presented in Section 9.4. $\mathbf{K}_a$ is the solution to the Riccati equation for the augmented model.

9.5.1 Design of LQI Control

Gain scheduling has not been utilised for this control method as it is expected that the integrator can compensate for the steady state error in all piston positions which was the largest improvement compared to a constant gain. Furthermore, gain scheduling did not prove advantageous compared to a constant gain when comparing the dynamic response of pole placement and LQR with gain scheduling.

The weight matrices $\mathbf{Q}$ and $\mathbf{R}$ are tuned for the worst-case linearisation point. Both weight matrices are chosen similar to those of LQR however as $\mathbf{Q}$ is expanded with two additional diagonal entries compared to LQR due to the two error states, two additional parameters must be tuned. The weight of the error states has been chosen considerably larger than the weight of the three system states which resulted in a faster response as $\mathbf{K}_I$ is increased. The pole locations of the uncompensated and compensated system for piston and rod side pressure are shown in Table 9.2.

	Uncompensated system	**Compensated system**
λ_1	-0.464	-29.6
λ_2	$-44.5 + j165$	$-46.4 + j167$
λ_3	$-44.5 - j165$	$-46.4 - j167$
λ_4		$-9 + j8.8$
λ_5		$-9 - j8.8$

Table 9.2: Locations of eigenvalues for the uncompensated system and with LQI control.

The closed loop and open loop poles have been plotted as a function of the piston position in Figure 9.11 using the constant gain matrix $\mathbf{K}_a$.

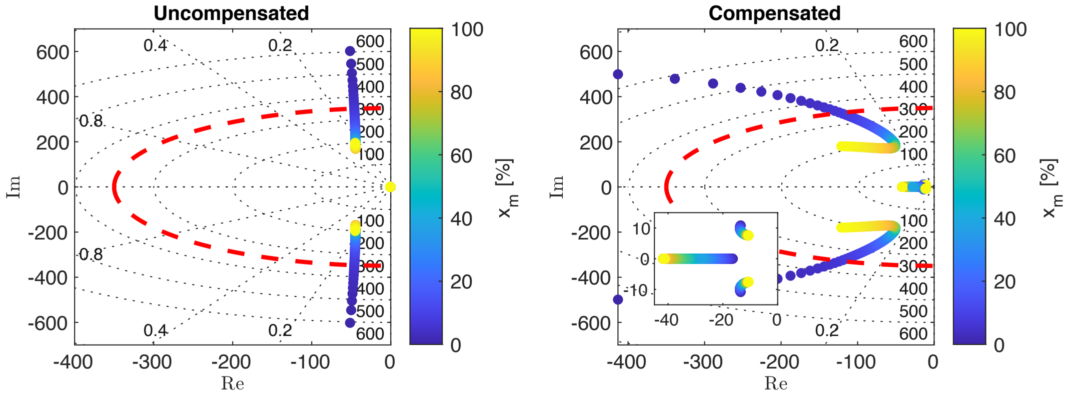

Figure 9.11: Closed loop pole location when linearised for the whole piston stroke length using a constant feedback gain matrix obtained by LQI. A zoomed view of the poles close to the origin is provided in the right figure. The red dashed line shows the natural frequency of the valve.

The complex conjugate pole pair around 10 [rad/s] does not move significantly when the piston position is changed with a damping ratio of approximately $\zeta = 0.7$. From Figure 9.11 it is however evident that the real pole is more aggressive compared to the gain scheduled LQR controller and similar to pole placement travelling from 20 to 40 [rad/s] as the piston position is increased. The faster complex conjugate pole pair exceeds the natural frequency of the valve as was also seen from the previous control methods.

The compensated and uncompensated velocity, rod side pressure and control effort step responses are compared in Figure 9.12.

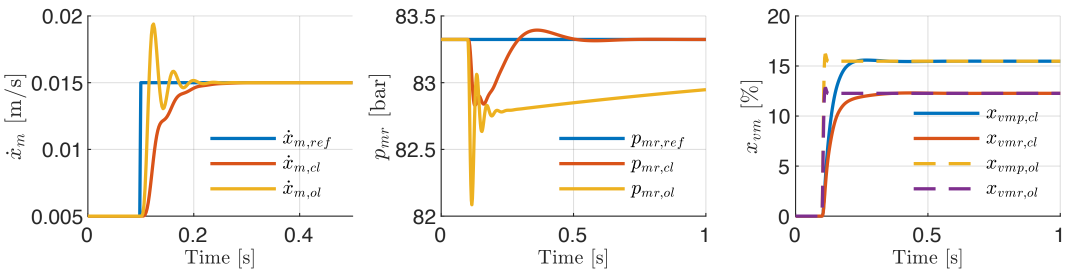

Figure 9.12: Piston velocity, rod side pressure and control effort comparison of open loop and closed loop response in the linear model.

The velocity and pressure responses of the compensated system have improved compared to the uncompensated. It can be seen that the damping of both velocity and pressure is increased and the velocity response has no overshoot. This is also seen in the pole map in Figure 9.11 where the real pole and slowest complex conjugate pole pair increase the system damping. The valve responses of the compensated system are less aggressive compared to the uncompensated and do not saturate.

The velocity and pressure responses for the compensated system have furthermore been tested on a step response for three different piston positions in the linear model. This is to conclude on the transient and steady state response when operating conditions change. The results can be seen in Figure 9.13.

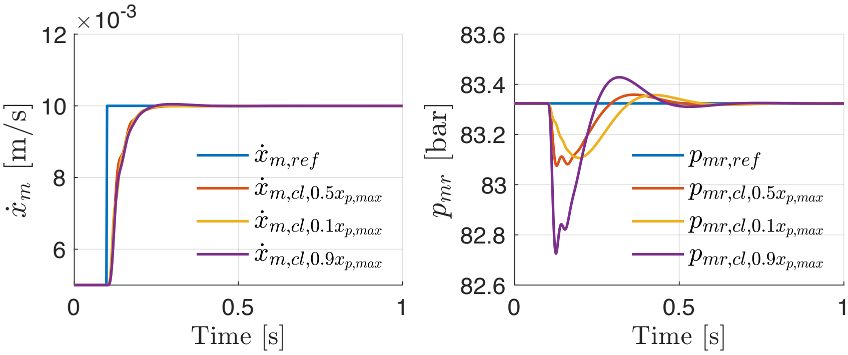

Figure 9.13: Closed loop response of velocity and pressure when tested on the linear model in three different piston positions: 10, 50 and 90 [%] of maximum stroke length.

Figure 9.13 shows a satisfactory velocity response which is close to independent of the piston position with a settling time of approximately 0.2 [s]. The rod side pressure response varies when tested in different piston positions and the worst response is seen close to the end of the stroke length. The settling time for the rod side pressure is approximately 0.5 [s] in all three piston positions. Both velocity and rod side pressures have no steady state error regardless of the tested piston position.

The step responses have now been tested in the linear model for pole placement, LQR with gain scheduling and LQI. The pole placement method showed an underdamped velocity and rod side pressure response, however, a satisfactory settling time. When evaluated in other piston positions, the responses varied and a steady state error occurred. A gain scheduling strategy was proposed to compensate for the change in dynamics when operating conditions varied and furthermore to decrease steady state errors. The response was tuned using LQR, however, when compared to the open loop dynamic response there was no significant improvement. The transient response did not improve when evaluated in other piston positions, however, the steady state error was eliminated for both pressure and velocity at the linearisation point of the pressure and velocity. It was decided to implement an integrator to guarantee no steady state error for a step reference as an error was expected when the controller was tested in the non-linear model. This is due to the implemented gain scheduling only compensating for a change in piston position while other operating conditions could change causing a steady state error. The results of the velocity and rod side *pressure responses have improved and the steady state error is removed.*

The responses have only been compared in the linear model, and the results when tested in the non-linear model are shown in the next chapter where the control strategies are compared. In the next section, the system is analysed to determine the three controllers capabilities when subjected to disturbance and noise.

9.6 Disturbance and Noise Analysis

In this section, the frequency responses of the system with controllers are analysed. The analysis is used to compare the controllers on reference tracking, disturbance rejection, and noise attenuation. Throughout the section, the frequency dependency (s) is omitted for simplicity and a scaled state space model is used to be able to compare the frequency responses. The relation between the unscaled state space model and the scaled state space model is shown in Equation (9.14) where the subscript 's' refers to the scaled model. The inputs are unchanged as the valve openings are already normalised.

$$\mathbf{x} = \mathbf{M}_x \, \mathbf{x}_s, \qquad \dot{\mathbf{x}} = \mathbf{M}_x \, \dot{\mathbf{x}}_s, \qquad \mathbf{u} = \mathbf{M}_u \, \mathbf{u}_s, \qquad \mathbf{y} = \mathbf{M}_y \, \mathbf{y}_s$$

$$\mathbf{M}_x = \begin{bmatrix} \dot{x}_{m,max} & 0 & 0 \\ 0 & p_s & 0 \\ 0 & 0 & p_s \end{bmatrix}, \qquad \mathbf{M}_u = \mathbf{I}, \qquad \mathbf{M}_y = \begin{bmatrix} \dot{x}_{m,max} & 0 \\ 0 & p_s \end{bmatrix} \tag{9.14}$$

The scaled state space model is expressed in Equation (9.15).

$$\dot{\mathbf{x}}_s = \underbrace{\mathbf{M}_x^{-1} \, \mathbf{A} \, \mathbf{M}_x}_{\mathbf{A}_s} \, \mathbf{x}_s + \underbrace{\mathbf{M}_x^{-1} \, \mathbf{A} \, \mathbf{M}_u}_{\mathbf{B}_s} \, \mathbf{u}_s, \qquad \mathbf{y}_s = \underbrace{\mathbf{M}_y^{-1} \, \mathbf{C} \, \mathbf{M}_x}_{\mathbf{C}_s} \, \mathbf{x}_s \tag{9.15}$$

The $\mathbf{Q}$ and $\mathbf{R}$ matrices are likewise scaled by setting $e_{i,max} = u_{j,max} = 1$ according to Equation (9.10) as these were equal to the maximum values used in the scaled model.

The block diagram of the compensated closed loop system controlled using the pole placement method and LQR using the gains from the worst-case linearisation point is shown in Figure 9.14 where disturbance, $\mathbf{d}$, and measurement noise, $\mathbf{n}$, are implemented. It should be noted that $\mathbf{d}$ and $\mathbf{n}$ are scaled 3x1 column vectors.

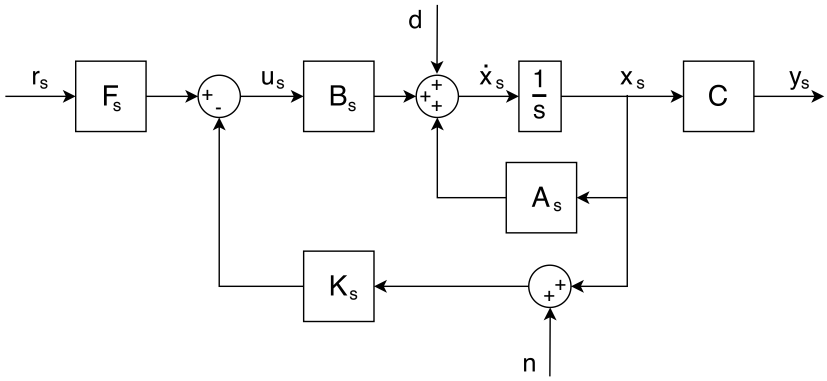

Figure 9.14: Block diagram of system controlled using pole placement and LQR with disturbance and noise.

In Figure 9.14 the disturbance is included in the state equation and could be the term including the load force, F_l, in the mechanical model. The noise is added to the feedback signal as it only affects the measurements.

The closed loop transfer function matrix, $\mathbf{G}_{cl}$, sensitivity function, $\mathbf{S}$, and noise transfer function matrix, $\mathbf{T}$, are expressed in Equation (9.16) and derived in Appendix D.2.1.

$$\begin{aligned}\mathbf{y}_s = & \underbrace{\mathbf{C}_s\,(s\,\mathbf{I} - \mathbf{A}_s + \mathbf{B}_s\,\mathbf{K}_s)^{-1}\,\mathbf{B}_s\,\mathbf{F}_s}_{\mathbf{G}_{cl}}\,\mathbf{r}_s + \underbrace{\mathbf{C}_s\,(s\,\mathbf{I} - \mathbf{A}_s + \mathbf{B}_s\,\mathbf{K}_s)^{-1}}_{\mathbf{S}}\,\mathbf{d} \\ & \underbrace{-\,\mathbf{C}_s\,(s\,\mathbf{I} - \mathbf{A}_s + \mathbf{B}_s\,\mathbf{K}_s)^{-1}\,\mathbf{B}_s\,\mathbf{K}_s}_{\mathbf{T}}\,\mathbf{n}\end{aligned} \tag{9.16}$$

The block diagram of the compensated closed loop system controlled by LQI is shown in Figure 9.15 where disturbance and measurement noise are implemented. The noise is added to the feedback signal and affects both the states and outputs which are fed back.

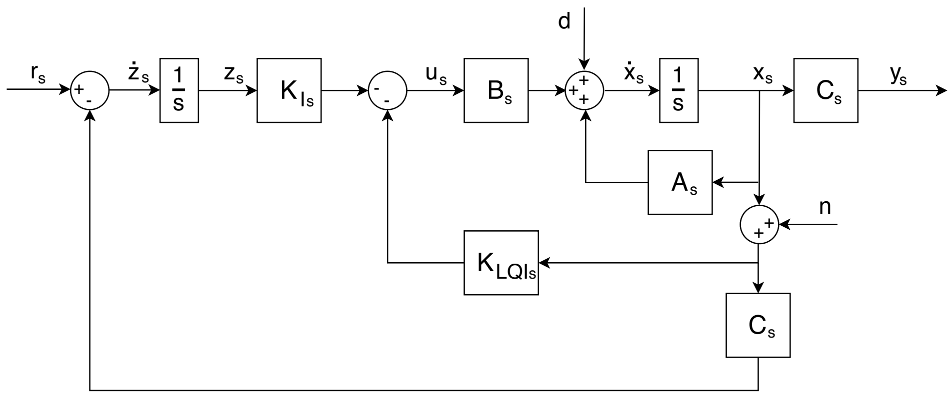

Figure 9.15: Block diagram of system controlled using LQI with disturbance and noise.

The closed loop transfer function matrix, $\mathbf{G}_{cl}$, sensitivity function, $\mathbf{S}$, and noise transfer function matrix, $\mathbf{T}$, are expressed in Equation (9.17) and derived in Appendix D.2.2.

$$
\begin{aligned}
\mathbf{y}_s = & \underbrace{-\,\mathbf{C}_s\left(s\,\mathbf{I}-\mathbf{A}_s+\mathbf{B}_s\,\mathbf{K}_{LQIs}-\mathbf{B}_s\,\mathbf{K}_{Is}\,\frac{1}{s}\,\mathbf{I}\,\mathbf{C}_s\right)^{-1}\mathbf{B}_s\,\mathbf{K}_{Is}\,\frac{1}{s}\,\mathbf{I}}_{\mathbf{G}_{cl}}\;\mathbf{r}_s \\
& + \underbrace{\mathbf{C}_s\left(s\,\mathbf{I}-\mathbf{A}_s+\mathbf{B}_s\,\mathbf{K}_{LQIs}-\mathbf{B}_s\,\mathbf{K}_{Is}\,\frac{1}{s}\,\mathbf{I}\,\mathbf{C}_s\right)^{-1}}_{\mathbf{S}}\;\mathbf{d} \\
& + \underbrace{\mathbf{C}_s\left(s\,\mathbf{I}-\mathbf{A}_s+\mathbf{B}_s\,\mathbf{K}_{LQIs}-\mathbf{B}_s\,\mathbf{K}_{Is}\,\frac{1}{s}\,\mathbf{I}\,\mathbf{C}_s\right)^{-1}\left(\mathbf{B}_s\,\mathbf{K}_{Is}\,\frac{1}{s}\,\mathbf{I}\,\mathbf{C}_s-\mathbf{B}_s\mathbf{K}_{LQIs}\right)}_{\mathbf{T}}\;\mathbf{n}
\end{aligned}
\tag{9.17}
$$

Singular Value Decomposition, SVD, which was described in Section 8.3 can be used to find the maximum and minimum singular values of $\mathbf{G}_{cl}$, $\mathbf{S}$, and $\mathbf{T}$. These maximum and minimum singular values are used to analyse and compare the closed loop systems. The ability of the closed loop system to track references, reject disturbances, and attenuate noise can be analysed by the criteria listed below[Skogestad and Postlethwaite, 2005, p. 341-342]:

- Reference tracking: $\overline{\sigma}(\mathbf{G}_{cl}) \approx \underline{\sigma}(\mathbf{G}_{cl}) \approx 1$
- Disturbance rejection: $\overline{\sigma}(\mathbf{S})$ small
- Noise attenuation: $\overline{\sigma}(\mathbf{T})$ small

However, disturbance rejection is often a requirement for low frequencies whereas noise attenuation is often a requirement for higher frequencies[Skogestad and Postlethwaite, 2005, p. 341-342].

The maximum and minimum singular values of the closed loop transfer function matrices, sensitivity function matrices, and noise transfer function matrices are plotted in Figure 9.16 for the three controllers. The solid lines are maximum singular values and the dashed lines are minimum singular values. The red graphs are for pole placement, PP, control, blue graphs are for LQR control, and green graphs are for LQI control.

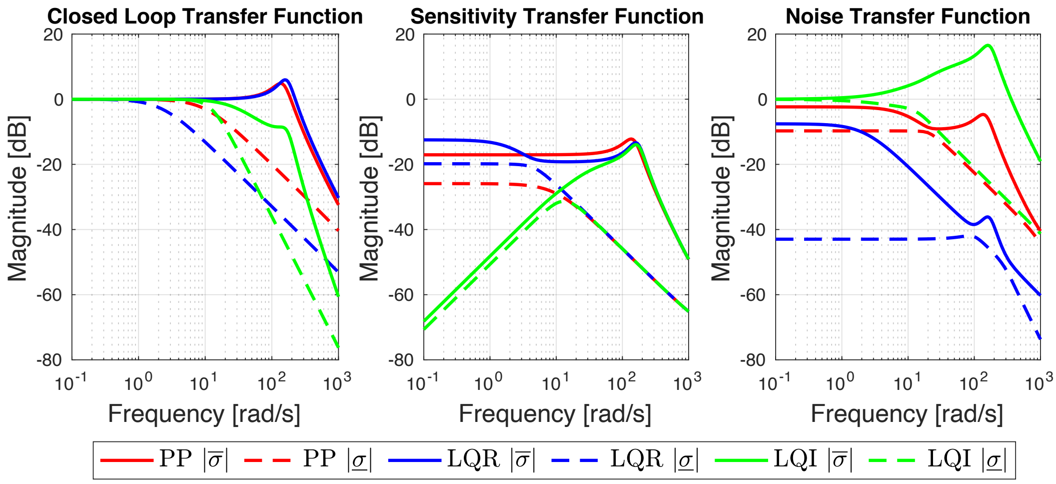

Figure 9.16: Singular values of the closed loop transfer function matrices, sensitivity function matrices, and noise transfer function matrices for the system with controllers.

The left plot in Figure 9.16 shows the frequency responses of the singular values for the three closed loop transfer functions, i.e the relationship between references and outputs. It is seen that $\overline{\sigma}(\mathbf{G}_{cl}) \approx \underline{\sigma}(\mathbf{G}_{cl}) \approx 1$ for frequencies below approximately 1 [rad/s] for all controllers. For the system with LQR control, the minimum singular value starts to decrease at around 1 [rad/s] whereas the maximum singular value is unchanged which means that the gain varies with the direction of the reference vector and that the outputs are not able to follow the references for all reference vector directions. The maximum and minimum singular values diverge around 5 [rad/s] for PP and around 10 [rad/s] for LQI which means the outputs are able to follow higher frequency references for all directions compared to PP and LQR. The two additional integrator poles for LQI result in a steeper decrease in the closed loop system gain for higher frequencies. For the systems with PP and LQR control, the maximum singular values have a resonance peak of 6 [dB] at around 200 [rad/s] whereas the maximum singular value for LQI is less affected and has a lower gain. This is also seen from the location of the poles for LQI in Figure 9.11 where the complex conjugate pole pair results in a higher damping ratio compared to PP and LQR in Figure 9.3 and 9.7, respectively. The resonance peak at 200 [rad/s] for PP and LQR results in amplification of the output signals for some directions of the reference vector. That results in overshoot where a peak of 6 [dB] corresponds to a gain of approximately 2 which is undesired.

The middle plot in Figure 9.16 shows the frequency responses of the singular values for the three sensitivity functions, i.e the relationship between disturbances and outputs. The gains of the singular values for the LQI control method are significantly smaller for lower frequencies compared to PP and LQR which indicates that the LQI controller is more capable of rejecting low frequency disturbances, e.g. a constant load force. At lower frequencies, the system with LQR control has a slightly higher gain than PP, however still around -20 [dB] for both. For higher frequencies, the responses are similar for all controllers where the gains start to decrease which means higher frequency disturbances have a smaller impact on the outputs. The ability of the closed loop systems to reject the load force, F_l, will be further studied when implementing the controllers in the non-linear model in Chapter 10.

The right plot in Figure 9.16 shows the frequency responses of the singular values for the three noise transfer functions, i.e the relationship between measurement noise and outputs. For the system with LQI control, the maximum singular value has a significant resonance peak around 200 [rad/s] which indicates that noise is amplified at these frequencies for some of the directions of the noise vector. The system with LQR control is more capable of attenuating measurement noise at higher frequencies according to Figure 9.16 compared to both PP and LQI, which is desired in a noisy environment.

Even though the LQI controller results in a good closed loop response and reject low frequency disturbances, it is not expected to perform well in practice due to the noise amplification according to the right plot in Figure 9.16. However, it should be noted that the valve dynamics are not included which may filter out higher frequencies. Furthermore, the gain of the closed loop frequency response starts to decrease around 10 [rad/s] which means frequencies of the noise above 10 [rad/s] could be low pass filtered. It will, however, introduce phase lag.

In conclusion, the LQI controller is able to track references over a larger frequency range compared to PP and LQR as $\overline{\sigma}(\boldsymbol{G}_{cl}) \approx \underline{\sigma}(\boldsymbol{G}_{cl}) \approx 1$ up to a higher frequency. LQI is better at rejecting low frequency disturbances than PP and LQR as $\overline{\sigma}(\boldsymbol{S})$ is smaller for lower frequencies, however LQI has a higher noise gain which means measurement noise may be amplified. LQR is better at attenuate measurement noise compared to PP and LQI as $\overline{\sigma}(\boldsymbol{T})$ is smaller for higher frequencies. Based on the closed loop, disturbance, and noise analysis, LQI yields the best results if measurement noise is accounted for.

Chapter 10

Results and Discussion

The results when implementing the controllers designed in Chapter 9 are presented in this chapter. For each of the control methods, the following characteristics are analysed: stability, disturbance rejection, sensitivity to parameter variation, steady state error, transient response, and closed loop frequency response[Philips and Parr, 2013, p. 175]. These characteristics are analysed to be able to compare the different control methods.

As there was no access to the physical test facilities to evaluate the designed controllers, emphasis is put on testing the controllers in a physical environment. All controllers are tested in the non-linear simulation model where measurement noise and discrete effects are included as described in Appendix C.2. The sensitivity towards model uncertainties of each control system is analysed by varying system parameters. The disturbance rejection is tested by adding the load force. The maximum allowed load force is defined in Appendix C.4. Steady state and transient responses are analysed visually and by calculating the Mean Absolute Error, MAE, between the references and system outputs.

10.1 Simulation Results

In this section, the controllers are tested in the non-linear simulation model. A reference trajectory is developed to compare the controller performance. The reference tracking of the controllers will first be visually compared for two different test conditions. First with a varying velocity and constant pressure references and thereafter a low amplitude sinusoidal velocity reference and varying pressure reference. Hereafter, the reference tracking for parameter variation and for other operating conditions is numerically compared with the Mean Absolute Error, MAE, between reference and output. Finally, the steady state errors for PP and LQR are compared.

10.1.1 Visual Comparison of First Test Condition

The first test condition for visual comparison is with the velocity reference shown in Figure 10.1.

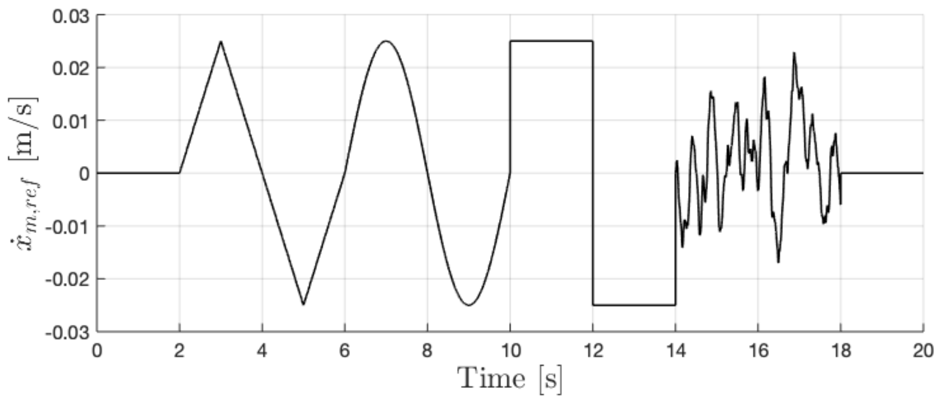

Figure 10.1: Velocity reference containing ramp, low frequency sinusoidal, step and wide-frequency reference.

The velocity reference includes a ramp, sinusoidal, stepped, and wide-frequency reference. The initial piston position is 50 [%] of stroke length, the peak velocity is ± 0.025 [m/s] and the rod side pressure reference, $p_{mr,ref}$, is constant at 50 [bar]. As no load force is applied during these tests, the maximum negative velocity is -0.03 [m/s] and the maximum positive velocity is 0.05 [m/s] for $p_{mr,ref}$=50 [bar] according to Figure C.9 which means the references are within the saturation limits.

Ramp and Step References

The PP, LQR with gain scheduling, and LQI controllers are compared for ramp and step references in Figure 10.2

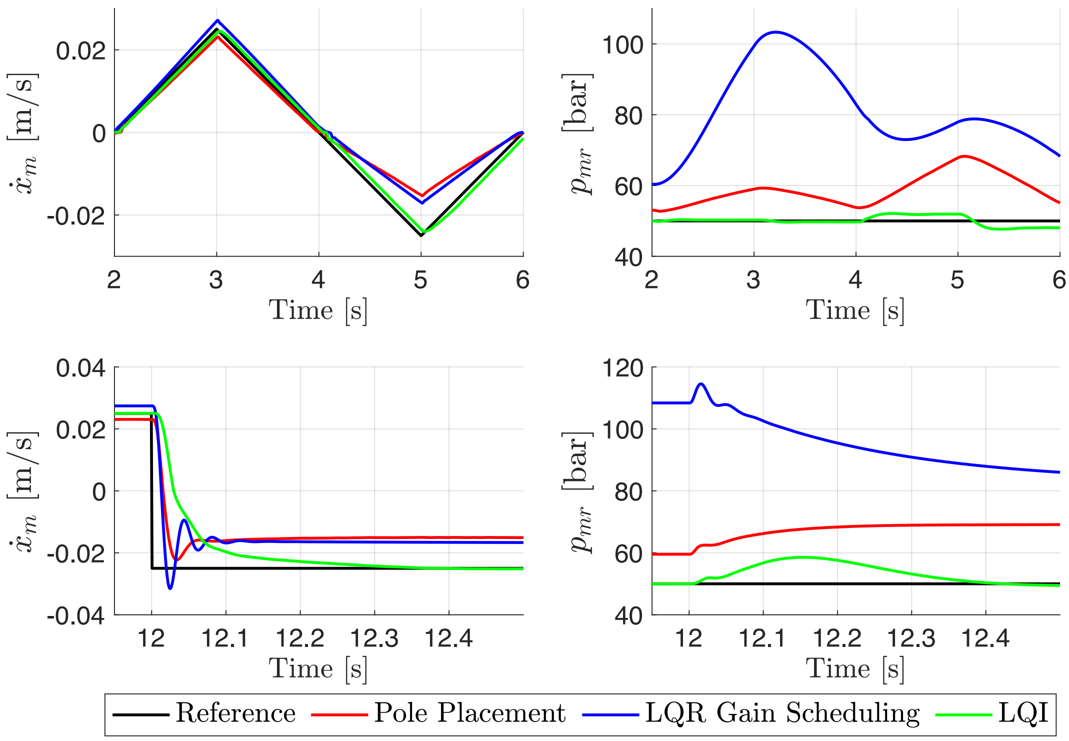

Figure 10.2: Velocity and rod side pressure response for the velocity reference presented in Figure 10.1 and a constant rod side pressure reference.

The steady state velocity error during step for PP and LQR is constant and for ramp references increasing, while the error is zero for the step reference and constant during the ramp when considering LQI. This is due to the PP and LQR controlled systems being type 0 systems while the order of the LQI controlled system was increased to a type 1 when the integrators were added[Philips and Parr, 2013, 199].

PP and LQR are not able to follow negative velocity references. This could be caused by the controllers being developed based on a linear model which is linearised in a positive velocity. As the velocity reference is in the opposite direction, a larger control gain is required due to the area ratio which is not accounted for in the control design. LQI can follow negative velocity references as the integrator compensates for the error between outputs and references.

The step responses of the velocity show a fast rise time, large overshoot and oscillatory response for LQR. A smaller overshoot and less oscillatory response is achieved for PP while the rise time is lower compared to LQR. LQI shows the slowest response however without any oscillations and overshoot. The settling time of PP and LQR are similar, where LQI is slower.

These results were also found during the design of the controllers where a slower and more damped response was seen for LQI when tested on the linear model as a slower complex conjugate pole pair was placed with a damping ratio of approximately $\zeta = 0.7$. PP and LQR are seen to be more dominated by the underdamped complex conjugate pole pair.

The rod side pressure controlled using PP and LQR shows a general offset compared to the reference, where the offset is greatest for LQR. When the rod side pressure is controlled by LQI the tracking is generally better and during the constant velocity reference, the steady state pressure error is eliminated. The pressure response during all references in Figure 10.1 is similar and is therefore not commented further.

Sinusoidal and Wide-Frequency References

The PP, LQR with gain scheduling, and LQI controllers are compared for sinusoidal and wide-frequency references in Figure 10.3.

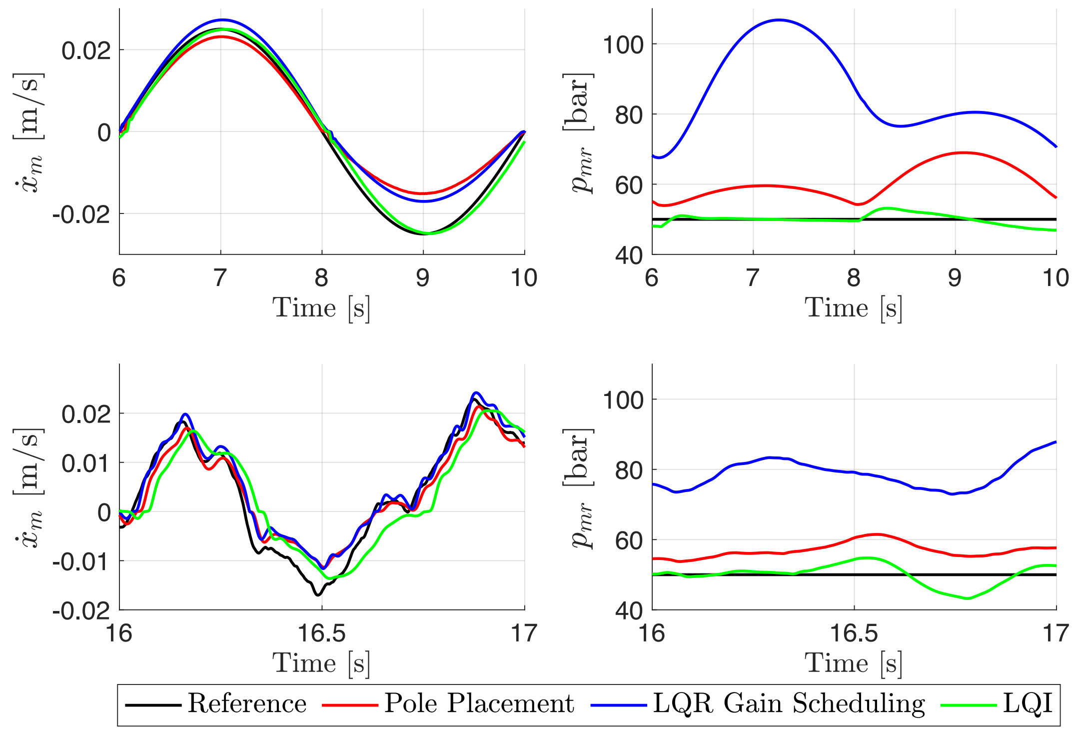

Figure 10.3: Velocity and rod side pressure response for the velocity reference presented in Figure 10.1 and a constant rod side pressure reference.

PP and LQR are not capable of following negative velocity references for the sinusoidal and wide-frequency references as was also seen for the ramp reference. The bandwidth of PP and LQR is however higher for the wide-frequency range compared to LQI for positive velocities, where satisfactory reference tracking is achieved. LQI generally lags the wide-frequency reference due to the additional slower complex conjugate pole pair. A faster rise time for PP and LQR was seen during the step response, which is the probable cause of greater reference tracking for the wide-frequency reference. The closed loop transfer functions in Figure 9.16 show a larger frequency reference tracking for certain input directions for PP and LQR compared to LQI which may explain the improved reference tracking.

The valve control effort is shown for the tested reference in Figure 10.4.

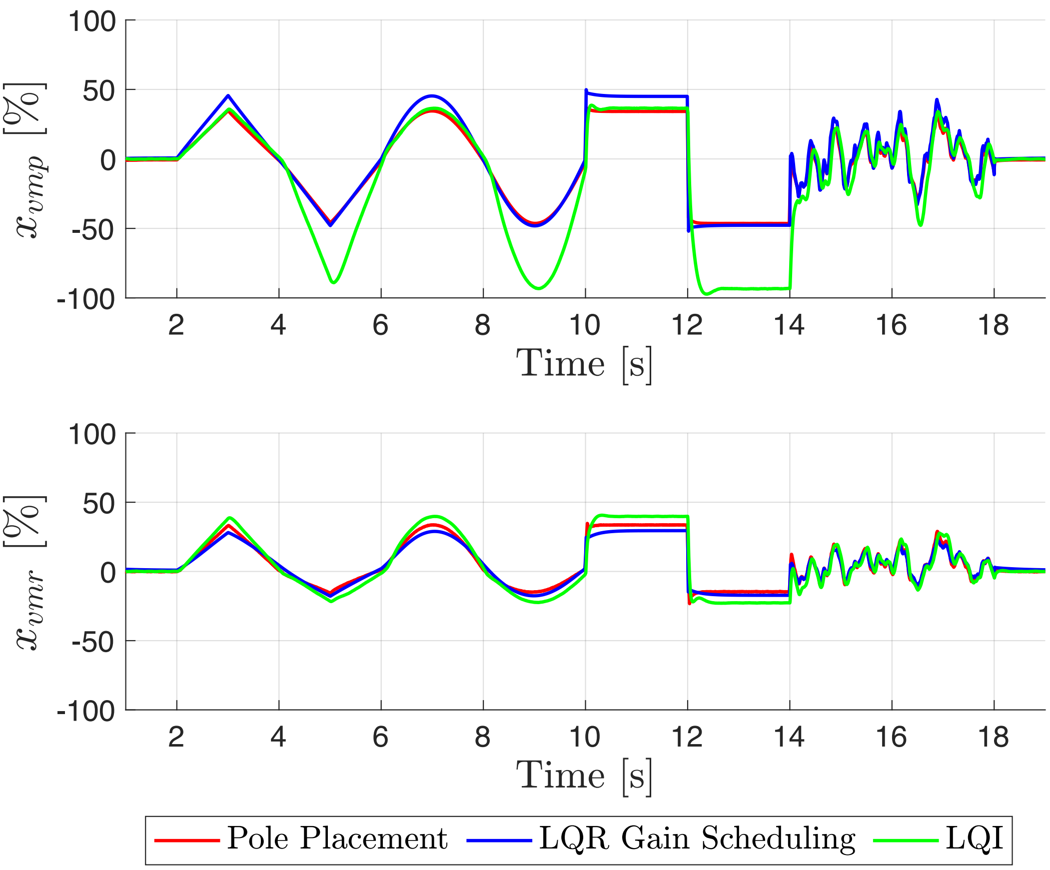

Figure 10.4: Control effort of the valves during the reference in Figure 10.1.

The control outputs for PP and LQR are similar however LQI stands out during the negative velocity where x_{vmp} is close to saturating due to a low piston side pressure caused by the already low rod side pressure reference. It should be noted that negative x_{vmp} connects the piston side chamber to tank, and negative x_{vmr} connects the rod side chamber to pump. To achieve the desired negative velocity, the valve has to almost open fully as the pressure drop across the orifice is low when connected to tank which is also seen in Figure C.9 where the velocity and pressure references are close to the saturation limit. The reason why the valves are close to saturation only for negative velocities may be caused by the area ratio of the cylinder. Accelerating the piston in the negative direction requires a higher pressure in the rod side chamber as $A_{mr} < A_{mp}$. Since PP and LQR are not linearised for negative velocities, a lower control effort for x_{vmp} is observed compared to LQI.

During the wide-frequency reference it can be seen how the control outputs of LQI generally lags the control outputs of PP and LQR which was also seen during the response in Figure 10.3. This may be caused by the additional integrator poles which introduce phase lag.

10.1.2 Visual Comparison of Second Test Condition

The second test condition for visual comparison is with the rod side pressure reference shown in Figure 10.5.

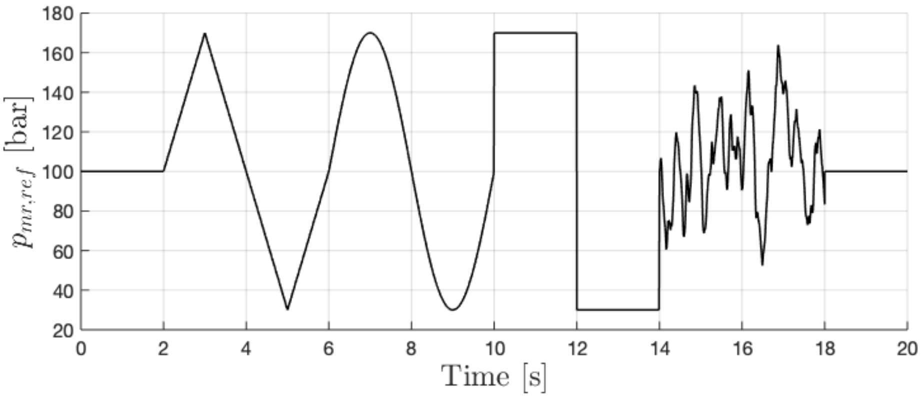

Figure 10.5: Rod side pressure reference containing ramp, low frequency sinusoidal, step and wide-frequency reference.

The pressure reference includes the same trajectories as the velocity reference. The pressure reference covers a pressure range from 30 [bar] to 170 [bar], where $p_s = 200$ [bar]. The velocity reference is sinusoidal with an amplitude of 0.0075 [m/s]. The initial piston position is 50 [%] of stroke length, and no load force is applied.

Ramp and Step References

The PP, LQR with gain scheduling, and LQI controllers are compared for ramp and steps references in Figure 10.6.

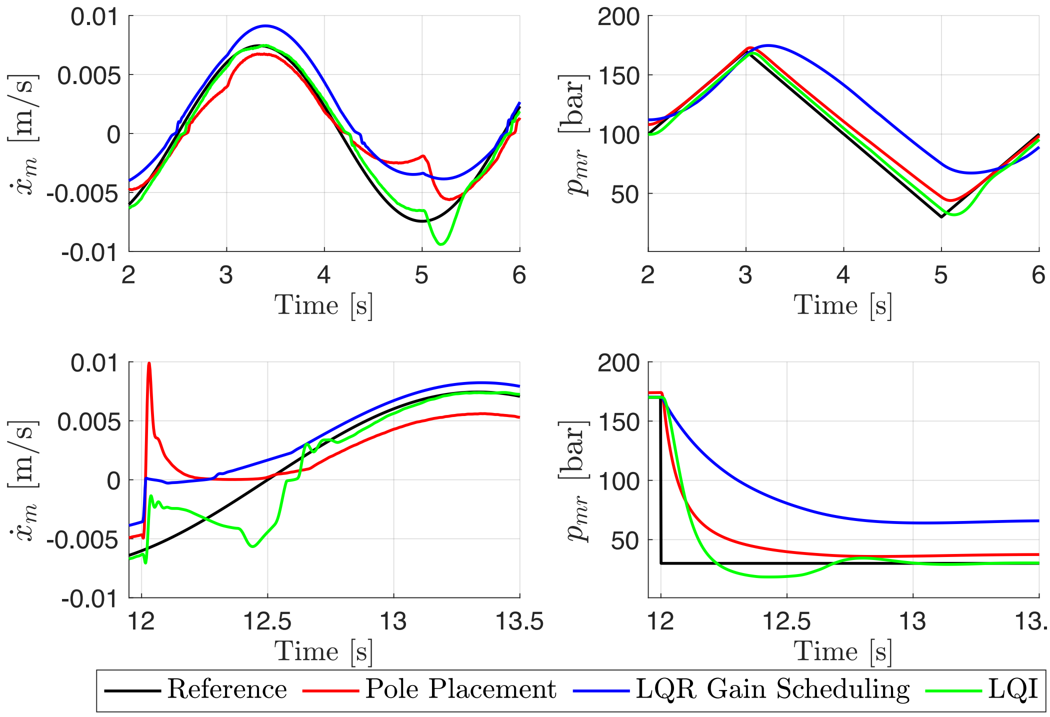

Figure 10.6: Velocity and rod side pressure response with the rod side pressure reference seen in Figure 10.5 and a velocity sinusoidal reference.

The rod side pressure reference is followed well during the ramp and step references when controlled with LQI. A constant steady state error during the ramp and zero steady state error during the step is seen. The error during the ramp builds up when looking at the PP response, while a constant error during steps is seen. For the LQR response, the pressure error during the ramp reference is close to constant and a constant steady state error is also seen during the step. Apart from the LQR response during ramp reference, the theory regarding system types holds true as was also seen when the reference was tested on velocity.

For the transient rod side pressure response during step references, PP and LQR have no overshoot, while LQI has a larger overshoot. The rise time of PP and LQI is similar and low compared to LQR which has a slow rise time. The settling time for the three controllers is approximately equal.

The velocity is generally followed in Figure 10.6 and 10.7, where LQI shows the best reference tracking.

Sinusoidal and Wide-Frequency References

The PP, LQR with gain scheduling, and LQI controllers are compared for sinusoidal and wide-frequency references in Figure 10.7.

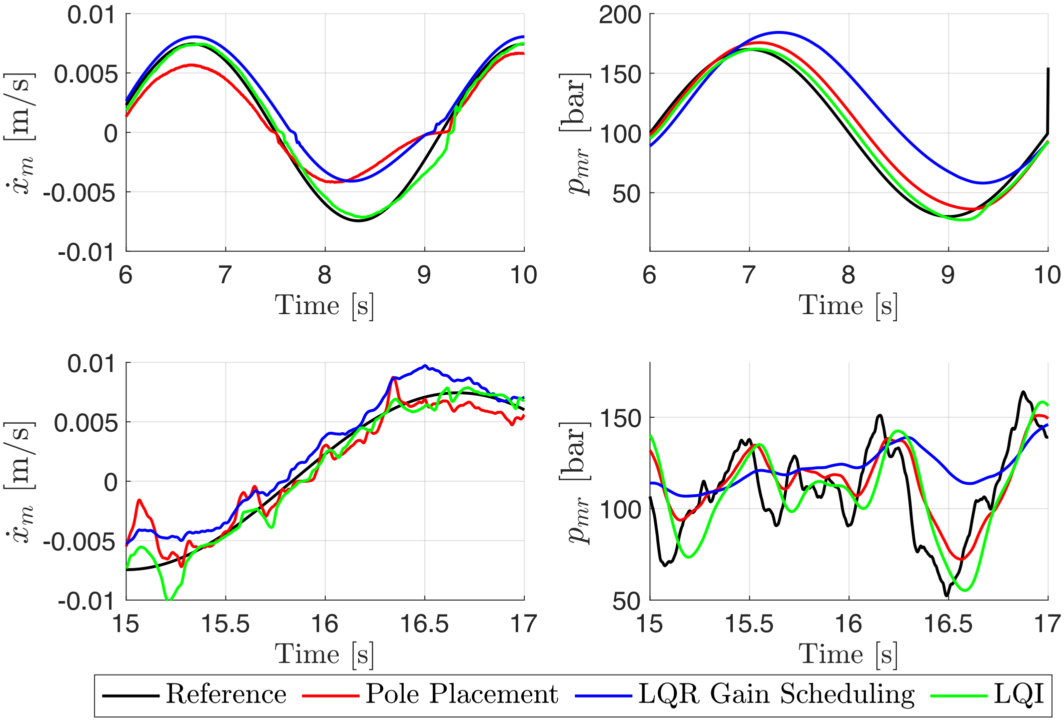

Figure 10.7: Velocity and rod side pressure response with the rod side pressure reference seen in Figure 10.5 and a velocity sinusoidal reference.

The rod side pressure reference tracking for the low frequency sine wave is in general followed well for PP and even better for LQI while LQR lags the reference significantly.

For the wide-frequency pressure reference it can be seen that LQR does not follow the reference well which is justified by the slow rise time seen during the step reference. This may be explained by the closed loop frequency response of the singular values in Figure 9.16 where the lower singular value gain decreases earlier for LQR compared to PP and LQI indicating worse reference tracking for certain reference directions. PP and LQI generally lag the pressure reference, however improved responses are seen compared to LQR.

The valve control effort during the tested reference in Figure 10.6 and 10.7 is seen in Figure 10.8.

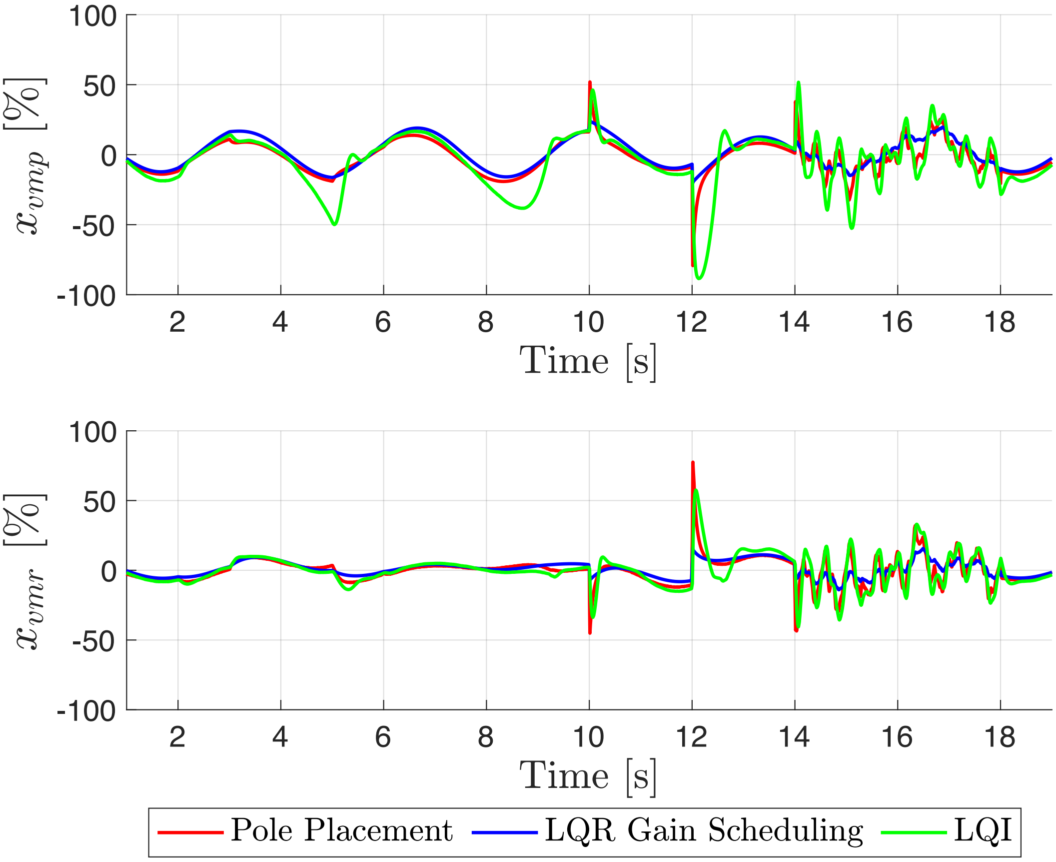

Figure 10.8: Control effort of the valves during the reference in Figure 10.5.

The control effort for LQI has larger fluctuations than PP and LQR. When tested on the wide-frequency reference, the control effort of LQR is low compared to PP and LQI, which confirms the slow response seen in Figures 10.6 and 10.7.

Noise with a frequency up to 3100 [rad/s] was implemented on the feedback signal for all controllers. As seen in the noise transfer functions in Figure 9.16, the LQI controller has a significant resonance peak around 200 [rad/s] and is expected to amplify noise. This is not seen to have any effect on the responses. The natural frequency of the valve dynamics is 350 [rad/s] and frequencies above that are expected to be filtered out. As the peak occurs at 200 [rad/s] noise at these frequencies are not expected to be attenuated. However, the noise amplification is dependent on the direction of the noise vector and is not amplified for all directions. Noise in a physical system can still be a problem as other noise vector directions and higher frequencies or amplitudes may be present and in that case, filters should be designed and implemented.

In conclusion, a generally better response is seen for LQI control in Figures 10.2, 10.3, 10.6, and 10.7. The system follows both negative and positive velocities, eliminates steady state error during step references for pressure and velocity, and a small constant error is seen during ramp references. The step response is damped with small or no overshoot. A lower bandwidth for LQI is, however, seen for the wide-frequency reference. The measurement noise does not have an impact on the responses even though the LQI controller was expected to amplify noise. When both pressure and velocities are to be controlled equally the LQI controller shows more promising results compared to PP and LQR where especially LQR deviates from the pressure reference.

The controllers have now been tested in the non-linear model for piston positions where the linear controllers were designed. In the next section, the controllers are tested for different piston positions and pressures to conclude on the controllers ability to handle change in operating conditions.

10.1.3 Operating Conditions

The visual comparison was limited to the same piston position and control of the rod side pressure. The performance at 10, 50, and 90 [%] of stroke length will be numerically compared as well as the performance for different pressure references for p_{mr} and p_{mp} at 10, 100, and 180 [bar]. The mean absolute error, MAE, is calculated using Equation (10.1) for each operating condition, where r is the velocity or pressure reference, y is the simulated velocity or pressure output, and n is the number of data points with a sampling frequency of 1 [kHz].

$$\text{MAE} = \frac{\sum_{i=1}^{n} |r_i - y_i|}{n} \tag{10.1}$$

MAE is chosen compared to the root mean square error, RMSE, as MAE weights large errors less. Both methods are however expected to give nearly same results. The lower the MAE is, the lower the error between the reference and simulated output is. During the change of operating conditions, no load force is applied and the velocity reference contains the first 14 [s] of Figure 10.1 but with a peak of 0.014 [m/s] to make sure that the valves do not saturate. MAE is calculated from $1 - 14$ [s] as the controllers need to settle at the references. All the different operating conditions are shown in Table 10.1.

		x_m [%]			p_m [bar]		
		10	50	90	10	100	180
		Pole placement					
$\dot{x}_m$ [m/s]	$10^{-4}\cdot$	20	19	20	36	19	-
p_{mp} [bar]		2.1	2.1	2.1	5.4	2.1	-
$\dot{x}_m$ [m/s]	$10^{-4}\cdot$	14	13	13	-	13	22
p_{mr} [bar]		5.8	5.9	5.9	-	5.9	3.5
		LQR with gain scheduling					
$\dot{x}_m$ [m/s]	$10^{-4}\cdot$	20	21	22	23	21	-
p_{mp} [bar]		8.7	8.9	9.2	20	8.9	-
$\dot{x}_m$ [m/s]	$10^{-4}\cdot$	21	21	22	-	21	21
p_{mr} [bar]		20	20	20	-	20	15
		LQI					
$\dot{x}_m$ [m/s]	$10^{-4}\cdot$	5.9	5.7	6.0	10	5.7	-
p_{mp} [bar]		0.23	0.22	0.23	1.3	0.22	-
$\dot{x}_m$ [m/s]	$10^{-4}\cdot$	5.6	5.5	5.9	-	5.5	5.9
p_{mr} [bar]		0.32	0.30	0.34	-	0.30	0.35

Table 10.1: MAE for velocity and pressures when operating conditions are changed.

The left column describes whether $\dot{x}_m$ and p_{mp} or $\dot{x}_m$ and p_{mr} are controlled. The top row describes the initial piston position and pressure reference. The pressure reference is 100 [bar] when changing the initial piston position between 10, 50, and 90 [%]. The initial piston position is at 50 [%] of stroke length when changing the pressure reference between 10, 100 and 180 [bar]. The value inside each cell of the table is the calculated MAE. When the p_{mp} reference is 180 [bar] it requires the rod side pressure to be higher than the supply pressure as $p_{mr} \approx p_{mp}/\alpha$. The cells are therefore referred to as '-'. When the p_{mr} reference is 10 [bar] it requires the piston side pressure to be $p_{mp} \approx p_{mr}\,\alpha \approx 5.9$ [bar]. The pressure levels become even lower during pressure tracking. This operating condition will, therefore, test the limit of possible pressure and velocity references rather than comparing the performance of the controllers. As an example, this is seen in Figure C.9 for case 4 where the negative velocity reference is limited by the low $p_{mr,ref}$ with no load force. These cells are, therefore, also referred to as '-'.

The errors are very similar at all piston positions. This was as expected for LQR as the gains were updated as a function of the piston position. The same tendency is however seen for PP and LQI, and the necessity of gain scheduling can therefore be questioned. The steady state error for LQR and PP at different piston positions is later compared, where this is further discussed.

From the continuity equations, when the volume decreases in the piston side chamber for $x_m = 10$ [%], the piston side pressure gradient gain increases. Likewise, the rod side pressure gradient gain increases for $x_m = 90$ [%]. This could result in pressure oscillations, however, it did not have any effect on the error.

At 10 [bar] pressure reference, the oil stiffness, β, is low. According to the continuity equation, the pressure gradient gain is therefore lower and the system is expected to becomes slower. This is generally seen from Table 10.1 where the pressures of 100 and 180 [bar] result in a more stiff oil and thereby also a lower error with the exception of p_{mp} when tested with LQR.

The linearisation point chosen when controllers were designed, was based on a worst-case condition to guarantee system stability when operating conditions change. *While the MAE differs in Table 10.1 when operating conditions were changed it can be concluded that stability was still maintained.*

10.1.4 Parameter Variations and Disturbance Rejection

In this section, it is analysed whether the controllers are robust towards disturbances and parameter variations. The parameters used during control design are based on the same parameters used in the simulation model. As errors between the physical test setup and simulation model were seen during validation, the controllers are tested when parameters are varied to determine how the controller performance differs when tested in a different environment.

The varied parameters are the ones which contribute the most to the uncertainty; viscous friction, B, Coulomb friction, τ_c, the oil bulk modulus, β_0, and the air content in the fluid, α, and have been increased and decreased from the validated values. They are individually changed according to the estimated uncertainty of each parameter. Changing the inertia will furthermore generalise the results, it is, however, omitted. The robustness against the load force F_l is analysed by changing it from 0% to 25% and 75% of max allowed load force which is defined in Figure C.10.

The mean absolute error is calculated before and after the parameter variation. The difference in the mean absolute error, ΔMAE, before and after the parameter variation is calculated using Equation (10.2).

$$\Delta\text{MAE} = \text{MAE}_{after} - \text{MAE}_{before} \tag{10.2}$$

ΔMAE will only show how much the error is changed, and not the relative change before and after the parameter variation. To determine whether the controllers are robust towards parameter variation, ΔMAE must be seen in relation to MAE_{before}. As LQI has a lower MAE than PP and LQR as seen in Table 10.1, ΔMAE must equally be lower for LQI to have the same relative change in error, compared to PP and LQR.

The same reference is used for all comparisons: the initial piston position $x_{m,i} = 50$ [%] of stroke length, the velocity reference contains the first 14 [s] of Figure 10.1, $p_{mr,ref} = 50$ [bar], and the load force $F_l = 0$ [N]. The load force is however changed in the last column. MAE is calculated from $1 - 14$ [s] as the outputs need to settle at the references.

		B		τ_c		β_0		α		F_l	
		-25%	25%	-100%	100%	-25%	25%	-50%	50%	25%	75%
		Pole placement									
$\dot{x}_m$ [m/s]	$10^{-5}\cdot$	-3.8	3.7	-2.3	2.6	-1.1	-0.85	-0.34	-0.17	34	510
p_{mr} [bar]	$10^{-2}\cdot$	4.9	-3.2	-0.25	0.29	0.66	0.51	0.65	0.92	580	3300
		LQR with gain scheduling									
$\dot{x}_m$ [m/s]	$10^{-5}\cdot$	1.8	-1.3	-0.029	0.21	0.56	-0.48	-0.43	0.47	-170	-82
p_{mr} [bar]	$10^{-2}\cdot$	7.0	-7.2	1.9	-2.2	13	-8.3	-4.4	4.1	-1700	340
		LQI									
$\dot{x}_m$ [m/s]	$10^{-5}\cdot$	-2.4	2.4	-0.71	0.85	0.15	-0.084	-0.23	0.29	-7.6	0.23
p_{mr} [bar]	$10^{-2}\cdot$	-3.2	3.2	-1.4	1.2	1.7	-0.9	-0.12	1.4	-18	-1.1

Table 10.2: ΔMAE when system parameters are varied.

In Table 10.2, the ΔMAE values when changing parameters are shown. It should be noted that all values for velocity are multiplied by 10^{-5} and all values for pressure are multiplied by 10^{-2}. It is seen in the table that the change in MAE is small and in the same range for all controllers when changing B, τ_C, β_0, and α. Furthermore, ΔMAE is small and a mix of positive and negative values which indicates that the changes are caused by other uncertainties as well, e.g. improved operating conditions. *As LQI has a lower MAE compared to PP and LQR and ΔMAE is equal for the three controllers, the relative change in error for LQI is higher than PP and LQR.*

In Table 10.2 it is seen that the LQI controller is robust towards the change in load force, F_l, due to the small ΔMAE whereas the ΔMAE's for PP and LQR are significantly larger. This was also seen in the frequency response of the sensitivity function in Figure 9.16 where the low frequency gain is significantly smaller for LQI.

The robustness towards the change in load force is shown by stepping the load force for a visual comparison. The settling time of the load steps is 0.04 [s] and the initial piston position is 50 [%] of the stroke length. The velocity and pressure references are shown in Figure 10.9 together with the comparison of the controllers.

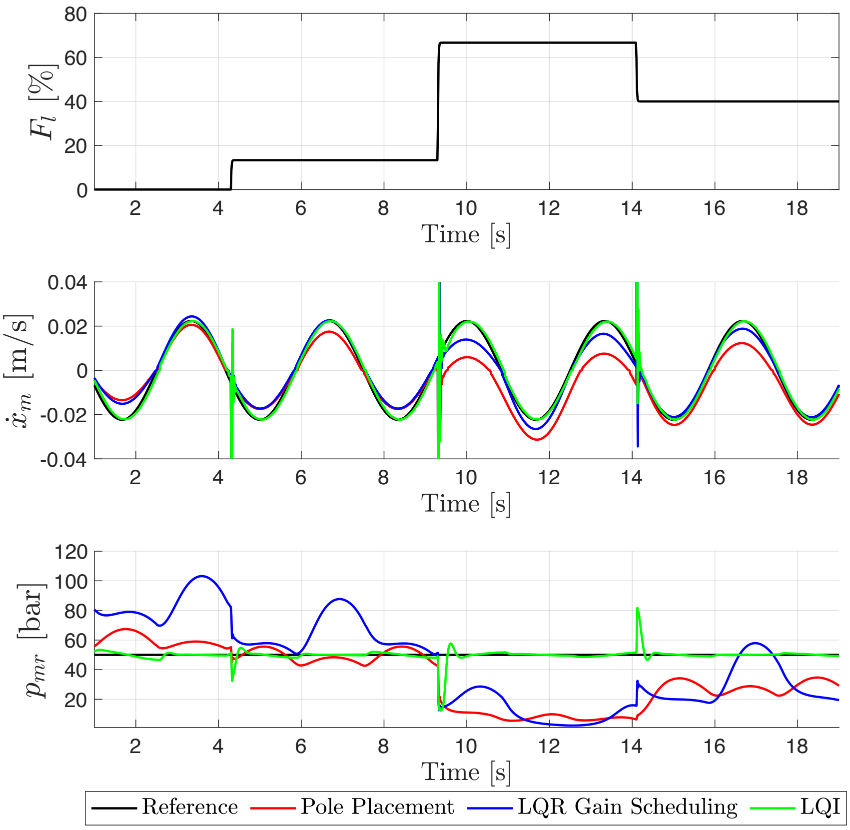

Figure 10.9: Velocity and pressure references and outputs for all controller when stepping the load force.

In Figure 10.9 the same tendency is seen where LQI follows the reference for both velocity and pressure with a small error. During the steps where higher frequencies are present, the PP, LQR and LQI controllers result in velocity spikes which can be related to the frequency response of the sensitivity functions in Figure 9.16 where the gains are equal for higher frequencies and spike around 200 [rad/s]. The PP and LQR controllers follow the velocity with a slightly larger error and the pressure with a significantly larger error compared to LQI. The control signals, x_{vmp} and x_{vmr}, are not plotted but did not saturate and it was observed that LQI results in slightly more aggressive control signals. This is due to the integrators acting on the tracking error between reference and output for LQI which is not the case for PP and LQR. *In conclusion, all controllers are fairly insensitive to parameter variations, and LQI is robust towards changes in the load force.*

10.1.5 Steady State Error

By designing LQR with gain scheduling it is expected that the steady state error will decrease compared to PP control since the pre-compensator gain is updated as a function of the piston position. The steady state errors for these two controllers are compared for velocity reference steps from 0 [m/s] to ±0.03 [m/s] and for pressure reference steps from 100 [bar] to 150 [bar]. This is done for an initial stroke length of 10, 50, and 90 [%]. The comparison is seen in Table 10.3 and *LQI is not shown due to zero steady state error for all tests.*

			+0.03 [m/s]	−0.03 [m/s]	+50 [bar]
x_m [%]	Reference		**Pole placement**		
10	$\dot{x}_m$ [m/s]	$10^{-4}\cdot$	4.3	83	7.7
	p_{mr} [bar]		0.22	15	7.7
50	$\dot{x}_m$ [m/s]	$10^{-4}\cdot$	5.1	81	8.0
	p_{mr} [bar]		0.93	15	7.7
90	$\dot{x}_m$ [m/s]	$10^{-4}\cdot$	7.9	78	7.9
	p_{mr} [bar]		0.59	7.2	7.8
			LQR with gain scheduling		
10	$\dot{x}_m$ [m/s]	$10^{-4}\cdot$	22	77	14
	p_{mr} [bar]		40	7.7	21
50	$\dot{x}_m$ [m/s]	$10^{-4}\cdot$	22	77	14
	p_{mr} [bar]		40	7.2	21
90	$\dot{x}_m$ [m/s]	$10^{-4}\cdot$	54	83	15
	p_{mr} [bar]		42	15	21

Table 10.3: Steady state error when PP and LQR are tested for a step reference on velocity and pressure.

The values in each cell are the absolute value of the steady state error. It is expected that the LQR with gain scheduling would have a lower steady state error at 10 and 90 [%] of stroke length compared to PP since the linearisation point for pole placement, PP, is $x_m = 50$ [%]. When stepping the linear model with LQR with gain scheduling at 10, 50 and 90 [%] of stroke length in Figure 9.9, the steady state error was eliminated, but by doing the same for PP in Figure 9.5, the steady state error was constant at 10 and 90 [%] of stroke length. The steady state error is, however, in general lower for PP at 10, 50 and 90 [%] of stroke length in Table 10.3. *As the error of PP does not change depending on the piston position LQR with gain scheduling proved unnecessary in regards to steady state error.*

10.1.6 Final Remarks

The validation was only conducted for piston positions between 70 and 85 [%] of the piston stroke length. The model must in addition be validated in other piston position and velocities. The controller performance is therefore not guaranteed in practice due to possible model deviations.

The controllers were designed based on a worst-case linearisation point. The point was chosen as a compromise between low natural frequency, low damping ratio and largest coupling of the system. It is assumed that the controllers will ensure system stability in the whole operating domain as this is the most conservative case. As none of the controlled systems became unstable the chosen strategy proved successful.

Chapter 11

Conclusion

The focus of this thesis is Investigation of Separate Meter-In Separate Meter-Out Control Strategies. The second part contains an analysis and control of a specific hydraulic SMISMO system and the following question has been answered during Part II:

- *How can controllers be designed for the system to reduce reference tracking error?*

To answer the question, a dynamic model was derived, validated, and analysed. The system was linearised in a worst-case linearisation point which considers the natural frequency, damping ratio and system couplings. As the system proved to be ill-conditioned and large couplings occur, MIMO controllers were designed. The linear controllers were tested under several conditions to conclude on reference tracking.

Three controllers were designed: Pole Placement, PP, Linear Quadratic Regulator, LQR, with gain scheduling, and Linear Quadratic Integral, LQI. The controllers were designed to minimise tracking error where velocity and pressure reference tracking were weighted equally.

In regards to steady state error, for stepped and ramped velocity and pressure references, LQI was superior compared to PP and LQR with gain scheduling. The integral action on the reference error of the LQI controller eliminated the steady state error during step references and with a constant error during ramped references. Both PP and LQR with gain scheduling had a constant steady state error and increasing error during ramped references. Even though the feedback gain matrix and pre-compensator for LQR with gain scheduling were updated as a function of the piston position, the steady state error was higher compared to PP.

For the transient response during stepped velocity references, the rise time of PP and LQR was lower compared to LQI. When stepping the pressure reference, the rise time of PP and LQI was lower compared to LQR. The settling time when stepping the velocity was twice as low for PP and LQR compared to LQI. When stepping the pressure the settling time were equal for PP, LQR, and LQI. During the settling time of stepped references, PP had a lower tracking error compared to LQR and LQI. The lower rise time of PP did not result in a large overshoot and the tracking error was kept lower.

The responses for the wide-frequency velocity reference when controlled with PP and LQR showed a larger bandwidth compared to LQI. However, when pressure was controlled, LQR showed a lower bandwidth compared to PP and LQI. The LQI was lagging the reference for higher frequencies due to the introduced phase lag caused by the additional integrator poles. When parameters were varied, LQI showed the greatest relative change in tracking error. The absolute change in error was however similar for PP, LQR and LQI. Finally, the disturbance rejection of LQI showed better results for both velocity and pressure control compared to PP and LQR due to the low gain of the sensitivity function at lower frequencies. Furthermore, the integrators act on the tracking error between reference and output for LQI which was not the case for PP and LQR.

LQI generally lowered reference tracking error when all references are weighted equally. The noise amplification should, however, be considered if implemented in a physical test setup.

Chapter 12

Future Works

This chapter will present relevant future work in continuation of the work conducted throughout this thesis.

Piston Velocity Gain Scheduling

In Part II, the system was linearised in a positive piston velocity and it was seen that the PP and LQR controllers were poor at tracking negative velocities possibly due to the piston area ratio. An extension to the control method could be gain scheduling where the gains are calculated as a function of piston velocities. In that way, the controller would account for the piston area ratio and possibly improve the tracking for negative piston velocities.

Piston Velocity Estimation

For the controllers to be implemented in the given test setup in Part II, the piston velocity should be estimated. That would require an estimator to be designed which estimates the velocity based on the available measurements. The poles for the estimator should be placed, such that the velocity estimation is updated faster than the controller acts. The estimator could be extended to a Kalman filter which finds the optimal estimator gain matrix[Skogestad and Postlethwaite, 2005, p. 346].

Switching Control

It was found that the pressure in the non-load carrying chamber should be controlled meaning the control outputs must change depending on the direction of the load force. Throughout the thesis, the controllers have not been tested for changes in the load force direction. To be able to implement the controllers in a physical environment where the direction of the load force may change, changing between controllers should be considered. For full state feedback control, the switching between controllers would require the feedback gain matrix and pre-compensator to change. The switching should be made such that high frequencies do not affect the dynamics. This could be done by interpolation between the values to get a continuous signal such that a smooth transition is achieved.

Weight of Control Variables

The characteristics of the tested controllers were evaluated equally for velocity and pressure control. This decision was possible as an application was not considered. If a specific application is chosen, the importance of one control variable may not be as important as the other. Instead, one of the control variables may be designed to improve the response of the other. As an example, if pressure control was weighted less than the velocity in this thesis, the velocity tracking may be improved.

Part III

Appendices

Appendix A

Transfer Functions

Piston Position

$$\frac{x_p(s)}{Q_p(s)} = g_{x_pQ_p}(s) = \frac{A_p\,\beta_p\,V_r}{(V_p\,V_r\,M\,s^2 + A_p^2\,\beta_p\,V_r + A_r^2\,\beta_r\,V_p)\,s} \tag{A.1}$$

$$\frac{x_p(s)}{Q_r(s)} = g_{x_pQ_r}(s) = \frac{A_r\,\beta_r\,V_p}{(V_p\,V_r\,M\,s^2 + A_p^2\,\beta_p\,V_r + A_r^2\,\beta_r\,V_p)\,s} \tag{A.2}$$

$$\frac{x_p(s)}{x_{vp}(s)} = g_{x_px_{vp}}(s) = \frac{a_1\,s + a_0}{(b_3\,s^3 + b_2\,s^2 + b_1\,s + b_0)\,s} \tag{A.3}$$

where:

$$\begin{aligned}
a_1 &= A_p\,\beta_p\,k_{Q_px_{vp}}\,V_r \\
a_0 &= A_p\,\beta_p\,\beta_r\,k_{Q_px_{vp}}\,k_{Q_pp_r} \\
b_3 &= V_p\,V_r\,M \\
b_2 &= -\beta_p\,k_{Q_pp_p}\,V_r\,M + \beta_r\,k_{Q_rp_r}\,V_p\,M \\
b_1 &= -\beta_p\,\beta_r\,k_{Q_pp_p}\,k_{Q_rp_r}\,M + A_p^2\,\beta_p\,V_r + A_r^2\,\beta_r\,V_p \\
b_0 &= A_p^2\,\beta_p\,\beta_r\,k_{Q_rp_r} - A_r^2\,\beta_p\,\beta_r\,k_{Q_pp_p}
\end{aligned} \tag{A.4}$$

$$\frac{x_p(s)}{x_{vr}(s)} = g_{x_p x_{vr}}(s) = \frac{a_3\, s + a_2}{(b_3\, s^3 + b_2\, s^2 + b_1\, s + b_0)\, s} \tag{A.5}$$

where b_3, b_2, b_1, and b_0 are expressed in Equation (A.4) and:

$$\begin{aligned} a_3 &= A_r\, \beta_r\, k_{Q_r x_{vr}}\, V_p \\ a_2 &= -A_r\, \beta_p\, \beta_r\, k_{Q_r x_{vr}}\, k_{Q_p p_p} \end{aligned} \tag{A.6}$$

Piston Velocity

$$\frac{\dot{x}_p(s)}{Q_p(s)} = g_{\dot{x}_p Q_p}(s) = \frac{A_p\, \beta_p\, V_r}{V_p\, V_r\, M\, s^2 + A_p^2\, \beta_p\, V_r + A_r^2\, \beta_r\, V_p} \tag{A.7}$$

$$\frac{\dot{x}_p(s)}{Q_r(s)} = g_{\dot{x}_p Q_r}(s) = \frac{A_r\, \beta_r\, V_p}{V_p\, V_r\, M\, s^2 + A_p^2\, \beta_p\, V_r + A_r^2\, \beta_r\, V_p} \tag{A.8}$$

$$\frac{\dot{x}_p(s)}{x_{vp}(s)} = g_{\dot{x}_p x_{vp}}(s) = \frac{a_1\, s + a_0}{b_3\, s^3 + b_2\, s^2 + b_1\, s + b_0} \tag{A.9}$$

where a_1, a_0, b_3, b_2, b_1, and b_0 are expressed in Equation (A.4).

$$\frac{\dot{x}_p(s)}{x_{vr}(s)} = g_{\dot{x}_p x_{vr}}(s) = \frac{a_3\, s + a_2}{b_3\, s^3 + b_2\, s^2 + b_1\, s + b_0} \tag{A.10}$$

where a_3 and a_2 are expressed in Equation (A.6), and b_3, b_2, b_1, and b_0 are expressed in Equation (A.4).

Piston Acceleration

$$\frac{\ddot{x}_p(s)}{Q_p(s)} = g_{\ddot{x}_p Q_p}(s) = \frac{A_p\, \beta_p\, V_r\, s}{V_p\, V_r\, M\, s^2 + A_p^2\, \beta_p\, V_r + A_r^2\, \beta_r\, V_p} \tag{A.11}$$

$$\frac{\ddot{x}_p(s)}{Q_r(s)} = g_{\ddot{x}_p Q_r}(s) = \frac{A_r\, \beta_r\, V_p\, s}{V_p\, V_r\, M\, s^2 + A_p^2\, \beta_p\, V_r + A_r^2\, \beta_r\, V_p} \tag{A.12}$$

$$\frac{\ddot{x}_p(s)}{x_{vp}(s)} = g_{\ddot{x}_p x_{vp}}(s) = \frac{(a_1\, s + a_0)\, s}{b_3\, s^3 + b_2\, s^2 + b_1\, s + b_0} \tag{A.13}$$

where a_1, a_0, b_3, b_2, b_1, and b_0 are expressed in Equation (A.4).

$$\frac{\ddot{x}_p(s)}{x_{vr}(s)} = g_{\ddot{x}_p x_{vr}}(s) = \frac{(a_3\, s + a_2)\, s}{b_3\, s^3 + b_2\, s^2 + b_1\, s + b_0} \tag{A.14}$$

where a_3 and a_2 are expressed in Equation (A.6), and b_3, b_2, b_1, and b_0 are expressed in Equation (A.4).

Piston Side Pressure

$$\frac{p_p(s)}{Q_p(s)} = g_{p_p Q_p}(s) = \frac{\beta_p\, V_r\, M\, s^2 + A_r^2\, \beta_p\, \beta_r}{(V_p\, V_r\, M\, s^2 + A_p^2\, \beta_p\, V_r + A_r^2\, \beta_r\, V_p)\, s} \tag{A.15}$$

$$\frac{p_p(s)}{Q_r(s)} = g_{p_p Q_r}(s) = -\frac{A_p\, A_r\, \beta_p\, \beta_r}{(V_p\, V_r\, M\, s^2 + A_p^2\, \beta_p\, V_r + A_r^2\, \beta_r\, V_p)\, s} \tag{A.16}$$

$$\frac{p_p(s)}{x_{vp}(s)} = g_{p_p x_{vp}}(s) = \frac{a_6\, s^2 + a_5\, s + a_4}{b_3\, s^3 + b_2\, s^2 + b_1\, s + b_0} \tag{A.17}$$

where b_3, b_2, b_1, and b_0 are expressed in Equation (A.4) and:

$$\begin{aligned} a_6 &= \beta_p\, k_{Q_p x_{vp}}\, V_r\, M \\ a_5 &= \beta_p\, \beta_r\, k_{Q_p x_{vp}}\, k_{Q_r p_r}\, M \\ a_4 &= A_r^2\, \beta_p\, \beta_r\, k_{Q_p x_{vp}} \end{aligned} \tag{A.18}$$

$$\frac{p_p(s)}{x_{vr}(s)} = g_{p_p x_{vr}}(s) = \frac{a_7}{b_3\, s^3 + b_2\, s^2 + b_1\, s + b_0} \tag{A.19}$$

where b_3, b_2, b_1, and b_0 are expressed in Equation (A.4) and:

$$a_7 = -A_p\, A_r\, \beta_p\, \beta_r\, k_{Q_r x_{vr}} \tag{A.20}$$

Rod Side Pressure

$$\frac{p_r(s)}{Q_p(s)} = g_{p_r Q_p}(s) = \frac{A_p\, A_r\, \beta_p\, \beta_r}{(V_p\, V_r\, M\, s^2 + A_p^2\, \beta_p\, V_r + A_r^2\, \beta_r\, V_p)\, s} \tag{A.21}$$

$$\frac{p_r(s)}{Q_r(s)} = g_{p_r Q_r}(s) = -\frac{\beta_r\, V_p\, M\, s^2 + A_p^2\, \beta_p\, \beta_r}{(V_p\, V_r\, M\, s^2 + A_p^2\, \beta_p\, V_r + A_r^2\, \beta_r\, V_p)\, s} \tag{A.22}$$

$$\frac{p_r(s)}{X_{vp}(s)} = g_{p_r x_{vp}}(s) = \frac{a_8}{b_3\, s^3 + b_2\, s^2 + b_1\, s + b_0} \tag{A.23}$$

where b_3, b_2, b_1, and b_0 are expressed in Equation (A.4) and:

$$a_8 = A_p\, A_r\, \beta_p\, \beta_r\, k_{Q_p x_{vp}} \tag{A.24}$$

$$\frac{p_r(s)}{x_{vr}(s)} = g_{p_r x_{vr}}(s) = \frac{a_{11}\, s^2 + a_{10}\, s + a_9}{b_3\, s^3 + b_2\, s^2 + b_1\, s + b_0} \tag{A.25}$$

where b_3, b_2, b_1, and b_0 are expressed in Equation (A.4) and:

$$\begin{aligned} a_{11} &= -\beta_r\, k_{Q_r x_{vr}}\, V_p\, M \\ a_{10} &= \beta_p\, \beta_r\, k_{Q_r x_{vr}}\, k_{Q_p p_p}\, M \\ a_4 &= -A_p^2\, \beta_p\, \beta_r\, k_{Q_r x_{vr}} \end{aligned} \tag{A.26}$$

Piston Side Flow

$$\frac{Q_p(s)}{x_{vp}(s)} = g_{Q_p x_{vp}}(s) = \frac{a_{13}\, s + a_{12}}{b_3\, s^3 + b_2\, s^2 + b_1\, s + b_0} \tag{A.27}$$

where b_3, b_2, b_1, and b_0 are expressed in Equation (A.4) and:

$$\begin{aligned} a_{13} &= A_p^2\, \beta_p\, k_{Q_p x_{vp}}\, V_r \\ a_{12} &= A_p^2\, \beta_p\, \beta_r\, k_{Q_p x_{vp}}\, k_{Q_r p_r} \end{aligned} \tag{A.28}$$

$$\frac{Q_p(s)}{x_{vr}(s)} = g_{Q_p x_{vr}}(s) = \frac{a_{15}\, s + a_{14}}{b_3\, s^3 + b_2\, s^2 + b_1\, s + b_0} \tag{A.29}$$

where b_3, b_2, b_1, and b_0 are expressed in Equation (A.4) and:

$$\begin{aligned} a_{15} &= -A_p\, A_r\, \beta_r\, k_{Q_r x_{vr}}\, V_p \\ a_{14} &= A_p\, A_r\, \beta_p\, \beta_r\, k_{Q_r x_{vr}}\, k_{Q_p p_p} \end{aligned} \tag{A.30}$$

Rod Side Flow

$$\frac{Q_r(s)}{x_{vp}(s)} = g_{Q_r x_{vp}}(s) = \frac{a_{17}\, s + a_{16}}{b_3\, s^3 + b_2\, s^2 + b_1\, s + b_0} \tag{A.31}$$

where b_3, b_2, b_1, and b_0 are expressed in Equation (A.4) and:

$$\begin{aligned} a_{17} &= A_p\, A_r\, \beta_p\, k_{Q_p x_{vp}}\, V_r \\ a_{16} &= A_p\, A_r\, \beta_p\, \beta_r\, k_{Q_p x_{vp}}\, k_{Q_r p_r} \end{aligned} \tag{A.32}$$

$$\frac{Q_r(s)}{x_{vr}(s)} = g_{Q_r x_{vr}}(s) = \frac{a_{19}\, s + a_{18}}{b_3\, s^3 + b_2\, s^2 + b_1\, s + b_0} \tag{A.33}$$

where b_3, b_2, b_1, and b_0 are expressed in Equation (A.4) and:

$$\begin{aligned} a_{19} &= A_r^2\, \beta_r\, k_{Q_r x_{vr}}\, V_p \\ a_{18} &= -A_r^2\, \beta_p\, \beta_r\, k_{Q_r x_{vr}}\, k_{Q_p p_p} \end{aligned} \tag{A.34}$$

Appendix B

Relative Gain Array

B.1 Piston Side Pressure with Flows as Input

The transfer function matrix where $y_1 = p_p$ and $y_2 = x_p$ is shown in Equation (B.1).

$$\begin{bmatrix} p_p(s) \\ x_p(s) \end{bmatrix} = \begin{bmatrix} g_{p_pQ_p}(s) & g_{p_pQ_r}(s) \\ g_{x_pQ_p}(s) & g_{x_pQ_r}(s) \end{bmatrix} \begin{bmatrix} Q_p(s) \\ Q_r(s) \end{bmatrix} \tag{B.1}$$

The relative gain, $\lambda^d_{p,f}$, is derived in Equations (B.2) to (B.5).

$$\lambda_{p,f}^{d} = \frac{1}{1 - \frac{g_{p_p Q_r}(s)\, g_{x_p Q_p}(s)}{g_{p_p Q_p}(s)\, g_{x_p Q_r}(s)}} \tag{B.2}$$

$$\Updownarrow$$

$$= \frac{1}{1 - \frac{-\frac{A_p\, A_r\, \beta_p\, \beta_r}{(V_p\, V_r\, M\, s^2 + A_p^2\, \beta_p\, V_r + A_r^2\, \beta_r\, V_p)\, s}\, \frac{A_p\, \beta_p\, V_r}{(V_p\, V_r\, M\, s^2 + A_p^2\, \beta_p\, V_r + A_r^2\, \beta_r\, V_p)\, s}}{\frac{\beta_p\, V_r\, M\, s^2 + A_r^2\, \beta_p\, \beta_r}{(V_p\, V_r\, M\, s^2 + A_p^2\, \beta_p\, V_r + A_r^2\, \beta_r\, V_p)\, s}\, \frac{A_r\, \beta_r\, V_p}{(V_p\, V_r\, M\, s^2 + A_p^2\, \beta_p\, V_r + A_r^2\, \beta_r\, V_p)\, s}}} \tag{B.3}$$

$$\Updownarrow$$

$$= \frac{1}{1 - \frac{-A_p^2\, A_r\, \beta_p^2\, \beta_r\, V_r}{A_r\, \beta_r\, V_p\, \beta_p\, V_r\, M\, s^2 + A_r^3\, \beta_r^2\, V_p\, \beta_p}} = \frac{1}{1 + \frac{A_p^2\, \beta_p\, V_r}{V_p\, V_r\, M\, s^2 + A_r^2\, \beta_r\, V_p}} \tag{B.4}$$

$$\Updownarrow$$

$$= \frac{V_p\, V_r\, M\, s^2 + A_r^2\, \beta_r\, V_p}{V_p\, V_r\, M\, s^2 + A_r^2\, \beta_r\, V_p + A_p^2\, \beta_p\, V_r} \tag{B.5}$$

The denominators of the transfer functions in Equation (B.3) are equal and cancel out in Equation (B.4).

B.1.1 Derivation of Frequencies Piston Side Pressure

$$\omega_w = \sqrt{\frac{A_r\, \beta_r}{M\, (L - x_p)}} \tag{B.6}$$

$$\begin{aligned} \omega_n &= \sqrt{\frac{A_p^2\, \beta_p\, V_r + A_r^2\, \beta_r\, V_p}{M\, V_p\, V_r}} = \sqrt{\frac{A_p^2\, \beta_p\, A_r\, (L - x_p) + A_r^2\, \beta_r\, A_p\, x_p}{M\, A_p\, x_p\, A_r\, (L - x_p)}} \\ &= \sqrt{\frac{A_p\, \beta_p\, (L - x_p) + A_r\, \beta_r\, x_p}{M\, x_p\, (L - x_p)}} = \sqrt{\frac{A_p\, \beta_p}{M\, x_p} + \frac{A_r\, \beta_r}{M\, (L - x_p)}} \end{aligned} \tag{B.7}$$

$$\begin{aligned} \omega_{c1} &= \sqrt{\frac{A_r^2\, \beta_r\, V_p - A_p^2\, \beta_p\, V_r}{V_p\, V_r\, M}} = \sqrt{\frac{A_r^2\, \beta_r\, A_p\, x_p - A_p^2\, \beta_p\, A_r\, (L - x_p)}{A_p\, x_p\, A_r\, (L - x_p)\, M}} \\ &= \sqrt{\frac{A_r\, \beta_r\, x_p - A_p\, \beta_p\, (L - x_p)}{x_p\, (L - x_p)\, M}} = \sqrt{\frac{A_r\, \beta_r}{(L - x_p)\, M} - \frac{A_p\, \beta_p}{x_p\, M}} \end{aligned} \tag{B.8}$$

$$\begin{aligned} \omega_{c2} &= \sqrt{\frac{A_p^2\, \beta_p\, V_r + 3\, A_r^2\, \beta_r\, V_p}{3\, V_p\, V_r\, M}} = \sqrt{\frac{A_p^2\, \beta_p\, A_r\, (L - x_p) + 3\, A_r^2\, \beta_r\, A_p\, x_p}{3\, A_p\, x_p\, A_r\, (L - x_p)\, M}} \\ &= \sqrt{\frac{A_p\, \beta_p\, (L - x_p) + 3\, A_r\, \beta_r\, x_p}{3\, x_p\, (L - x_p)\, M}} = \sqrt{\frac{1}{3}\, \frac{A_p\, \beta_p}{x_p\, M} + \frac{A_r\, \beta_r}{(L - x_p)\, M}} \end{aligned} \tag{B.9}$$

$$\omega_p = \sqrt{\frac{A_p^2\,\beta_p\,V_r + A_r^2\,\beta_r\,V_p}{V_p\,V_r\,M}} = \sqrt{\frac{A_p\,\beta_p}{M\,x_p} + \frac{A_r\,\beta_r}{M\,(L - x_p)}} = \omega_n \tag{B.10}$$

$$\begin{aligned}
\lambda_{p,f}^{o} &= \frac{A_p^2\,\beta_p\,V_r}{V_p\,V_r\,M\,s^2 + A_r^2\,\beta_r\,V_p + A_p^2\,\beta_p\,V_r} = \frac{1}{1 + \frac{V_p\,V_r\,M\,s^2 + A_r^2\,\beta_r\,V_p}{A_p^2\,\beta_p\,V_r}} \\
&\frac{V_p\,V_r\,M\,s^2 + A_r^2\,\beta_r\,V_p}{A_p^2\,\beta_p\,V_r} = -1 \rightarrow \frac{-V_p\,V_r\,M\,\omega_p^2 + A_r^2\,\beta_r\,V_p}{A_p^2\,\beta_p\,V_r} = -1 \\
V_p\,V_r\,M\,\omega_p^2 - A_r^2\,\beta_r\,V_p &= A_p^2\,\beta_p\,V_r \rightarrow \omega_p = \sqrt{\frac{A_p^2\,\beta_p\,V_r + A_r^2\,\beta_r\,V_p}{V_p V_r M}}
\end{aligned} \tag{B.11}$$

B.2 Rod Side Pressure with Flows as Inputs

The relative gain, $\lambda_{r,f}^{d}$, is expressed in Equation (B.12) when pairing the diagonal.

$$\lambda_{r,f}^{d} = \frac{A_r^2\,\beta_r\,V_p}{V_p\,V_r\,M\,s^2 + A_p^2\,\beta_p\,V_r + A_r^2\,\beta_r\,V_p} \tag{B.12}$$

The relative gain, $\lambda_{r,f}^{o}$, when pairing the off-diagonal is expressed in Equation (B.13).

$$\lambda_{r,f}^{o} = \frac{V_p\,V_r\,M\,s^2 + A_p^2\,\beta_p\,V_r}{V_p\,V_r\,M\,s^2 + A_p^2\,\beta_p\,V_r + A_r^2\,\beta_r\,V_p} \tag{B.13}$$

Equation (B.14) should be satisfied to get $\lambda_{r,f}^{d}$ as close to 1 as possible.

$$\begin{aligned} &|A_r^2\,\beta_r\,V_p| \gg |V_p\,V_r\,M\,s^2 + A_p^2\,\beta_p\,V_r| \\ &\Updownarrow \\ &|A_r^2\,\beta_r| \gg \left| V_r\,M\,s^2 + A_p^2\,\beta_p\,\frac{V_r}{V_p} \right| \end{aligned} \tag{B.14}$$

The volumes, $V_p = x_p\,A_p$ and $V_r = (L - x_p)\,A_r$, are substituted into Equation (B.14) where the dead volumes, V_{p0} and V_{r0}, are neglected.

$$\lambda_{r,f}^{d} \approx 1: \quad 1 \gg \left| \frac{(L - x_p)\,M}{A_r\,\beta_r}\,s^2 + \frac{\beta_p}{\beta_r}\,\frac{A_p}{A_r}\,\frac{L - x_p}{x_p} \right| \tag{B.15}$$

The inequality is opposite when pairing the off-diagonal:

$$\lambda_{r,f}^{o} \approx 1: \quad 1 \ll \left| \frac{(L - x_p)\,M}{A_r\,\beta_r}\,s^2 + \frac{\beta_p}{\beta_r}\,\frac{A_p}{A_r}\,\frac{L - x_p}{x_p} \right| \tag{B.16}$$

B.2.1 Low Frequency Range

The relative gains are evaluated in the low frequency range by letting $s \to 0$. The simplified expressions are shown in Equations (B.17) and (B.18), where $\gamma = \beta_r/\beta_p$, $\alpha = A_r/A_p$, and $\epsilon = x_p/(L - x_p)$.

$$\lambda^d_{r,f} \approx 1: \qquad 1 \gg \left|\frac{\beta_p}{\beta_r}\,\frac{A_p}{A_r}\,\frac{L-x_p}{x_p}\right| \Rightarrow 1 \ll \left|\frac{\beta_r}{\beta_p}\,\frac{A_r}{A_p}\,\frac{x_p}{L-x_p}\right| = |\gamma\,\alpha\,\epsilon| \tag{B.17}$$

$$\lambda^o_{r,f} \approx 1: \qquad 1 \ll \left|\frac{\beta_p}{\beta_r}\,\frac{A_p}{A_r}\,\frac{L-x_p}{x_p}\right| \Rightarrow 1 \gg \left|\frac{\beta_r}{\beta_p}\,\frac{A_r}{A_p}\,\frac{x_p}{L-x_p}\right| = |\gamma\,\alpha\,\epsilon| \tag{B.18}$$

It should be noted that Equations (B.17) and (B.18) are equal to Equations (5.21) and (5.22), respectively. *That means the conclusion for* $\lambda^d_{r,f}$ *is the same as for* $\lambda^d_{p,f}$*, and the conclusion for* $\lambda^o_{r,f}$ *is the same as for* $\lambda^o_{p,f}$ *at low frequencies.*

B.2.2 Transition Frequency Range

The frequency dependent inequalities are repeated in Equations (B.19) and (B.20) where s is substituted by $j\,\omega$.

$$\lambda^d_{r,f} \approx 1: \qquad 1 \gg \left|-\frac{(L-x_p)\,M}{A_r\,\beta_r}\,\omega^2 + \frac{\beta_p}{\beta_r}\,\frac{A_p}{A_r}\,\frac{L-x_p}{x_p}\right| \tag{B.19}$$

$$\lambda^o_{r,f} \approx 1: \qquad 1 \ll \left|-\frac{(L-x_p)\,M}{A_r\,\beta_r}\,\omega^2 + \frac{\beta_p}{\beta_r}\,\frac{A_p}{A_r}\,\frac{L-x_p}{x_p}\right| \tag{B.20}$$

The frequency, ω_w, at which the right hand sides of Equations (B.19) and (B.20) equal 0 is expressed in Equation (B.21).

$$-\frac{(L-x_p)\,M}{A_r\,\beta_r}\,\omega_w^2 + \frac{\beta_p}{\beta_r}\,\frac{A_p}{A_r}\,\frac{L-x_p}{x_p} = 0 \tag{B.21}$$

For the frequency, ω_w, $\lambda^d_{r,f} = 1$, and couplings are less significant when pairing the diagonal. The frequency, ω_w, is isolated in Equation (B.22).

$$\omega_w = \sqrt{\frac{\beta_p}{\beta_r}\,\frac{A_p}{A_r}\,\frac{L-x_p}{x_p}\,\frac{A_r\,\beta_r}{(L-x_p)\,M}} = \sqrt{\frac{A_p\,\beta_p}{M\,x_p}} \tag{B.22}$$

The natural frequency is expressed in Equation (B.23).

$$\omega_n = \sqrt{\frac{A_p\,\beta_p}{M\,x_p} + \frac{A_r\,\beta_r}{M\,(L - x_p)}} = \sqrt{\omega_w^2 + \frac{A_r\,\beta_r}{M\,(L - x_p)}} \tag{B.23}$$

The frequency ω_w is expressed as a function of ω_n in Equation (B.24).

$$\omega_w = \sqrt{\omega_n^2 - \frac{A_r\,\beta_r}{M\,(L - x_p)}} \tag{B.24}$$

It is seen from Equation (B.24) that as β_p and A_p increase, both frequencies increase, and as β_r and A_r increase, ω_n increases whereas ω_w is unaffected. *It is concluded that $\lambda^d_{r,f} = 1$ at the frequency ω_w which is lower than the natural frequency.*

B.2.3 Coupled Frequencies and High Frequencies

The frequency, ω_c, at which $\lambda^d_{r,f}$ and $\lambda^o_{r,f}$ cross and the cross couplings become significant is found by letting $\lambda^d_{r,f} = 0.5$.

$$\begin{gathered}\lambda^d_{r,f} = \frac{A_r^2\,\beta_r\,V_p}{-V_p\,V_r\,M\,\omega_c^2 + A_p^2\,\beta_p\,V_r + A_r^2\,\beta_r\,V_p} = K \\ \Updownarrow \\ \omega_c = \sqrt{\frac{K\,A_p^2\,\beta_p\,V_r + (K-1)\,A_r^2\,\beta_r\,V_p}{K\,V_p\,V_r\,M}}\end{gathered} \tag{B.25}$$

K is then substituted by 0.5 resulting in ω_c in Equation (B.30).

$$\omega_c = \sqrt{\frac{0.5\,A_p^2\,\beta_p\,V_r - 0.5\,A_r^2\,\beta_r\,V_p}{0.5\,V_p\,V_r\,M}} = \sqrt{\frac{A_p\,\beta_p}{x_p\,M} - \frac{A_r\,\beta_r}{(L - x_p)\,M}} \tag{B.26}$$

There is a positive and a negative fraction in Equation (B.30), which means ω_c is only real if the following is satisfied:

$$\frac{A_r\,\beta_r}{(L - x_p)\,M} \leq \frac{A_p\,\beta_p}{x_p\,M} \qquad \Rightarrow \qquad 1 \geq \alpha\gamma\epsilon \tag{B.27}$$

That means ω_c is real if the inequality in Equation (5.35) is satisfied.

The relative gain is reformulated in Equation (B.28), to find the frequency, ω_p at which $\lambda^d_{r,f}$ peaks.

$$\lambda^d_{r,f} = \frac{1}{1 + \frac{-V_p\,V_r\,M\,\omega_p^2 + A_p^2\,\beta_p\,V_r}{A_r^2\,\beta_r\,V_p}} \tag{B.28}$$

The positive frequency, ω_p, at which $\lambda^d_{r,f} \to \infty$ happens is found in Equation (B.2.3).

$$\omega_p = \sqrt{\frac{A_p^2\,\beta_p\,V_r + A_r^2\,\beta_r\,V_p}{V_p\,V_r\,M}} = \sqrt{\frac{A_p\,\beta_p}{M\,x_p} + \frac{A_r\,\beta_r}{M\,(L - x_p)}} = \omega_n \tag{B.29}$$

It is seen from Equation that the frequency ω_p is equal to the frequency ω_n. The same is valid for the peak of $\lambda^o_{r,f}$.

It is concluded that $\lambda^d_{r,f}$ and $\lambda^o_{r,f}$ cross in the frequency ω_c expressed in Equation (B.30) *if the inequality in Equation* (B.27) *is satisfied. Furthermore, $\lambda^d_{r,f}$ peaks at the natural frequency ω_n. Finally, the high frequency range when $s \to \infty$, couplings for the pairing X_p/Q_p and P_r/Q_r are less significant as $\lambda^o_{r,f} \to 1$.*

B.2.4 Derivation of Frequencies Rod Side Pressure

$$\begin{aligned}
\omega_{c1} &= \sqrt{\frac{0.5\,A_p^2\,\beta_p\,V_r - 0.5\,A_r^2\,\beta_r\,V_p}{0.5\,V_p\,V_r\,M}} = \sqrt{\frac{A_p^2\,\beta_p\,V_r - A_r^2\,\beta_r\,V_p}{V_p\,V_r\,M}} \\
&= \sqrt{\frac{A_p^2\,\beta_p\,A_r\,(L - x_p) - A_r^2\,\beta_r\,A_p\,x_p}{A_p\,x_p\,A_r\,(L - x_p)\,M}} = \sqrt{\frac{A_p\,\beta_p\,(L - x_p) - A_r\,\beta_r\,x_p}{x_p\,(L - x_p)\,M}} \\
&= \sqrt{\frac{A_p\,\beta_p}{x_p\,M} - \frac{A_r\,\beta_r}{(L - x_p)\,M}}
\end{aligned} \tag{B.30}$$

$$\begin{aligned}
\omega_{c2} &= \sqrt{\frac{-0.5\,A_p^2\,\beta_p\,V_r - 1.5\,A_r^2\,\beta_r\,V_p}{-0.5\,V_p\,V_r\,M}} = \sqrt{\frac{A_p^2\,\beta_p\,V_r + 3\,A_r^2\,\beta_r\,V_p}{V_p\,V_r\,M}} \\
&= \sqrt{\frac{A_p^2\,\beta_p\,A_r\,(L - x_p) + 3\,A_r^2\,\beta_r\,A_p\,x_p}{A_p\,x_p\,A_r\,(L - x_p)\,M}} = \sqrt{\frac{A_p\,\beta_p\,(L - x_p) + 3\,A_r\,\beta_r\,x_p}{x_p\,(L - x_p)\,M}} \\
&= \sqrt{\frac{A_p\,\beta_p}{x_p\,M} + \frac{3\,A_r\,\beta_r}{(L - x_p)\,M}}
\end{aligned} \tag{B.31}$$

B.3 Piston Side Pressure with Valve Openings as Inputs

The transfer function matrix where $y_1 = Q_p$ and $y_2 = p_p$ is shown in Equation (B.32).

$$\begin{bmatrix} p_p(s) \\ Q_p(s) \end{bmatrix} = \begin{bmatrix} g_{p_p x_{vp}}(s) & g_{p_p x_{vr}}(s) \\ g_{Q_p x_{vp}}(s) & g_{Q_p x_{vr}}(s) \end{bmatrix} \begin{bmatrix} x_{vp}(s) \\ x_{vr}(s) \end{bmatrix} \tag{B.32}$$

The relative gain, $\lambda_{p,v}^{d}$, is derived in Equations (B.33) to (B.36).

$$\lambda_{p,v}^{d} = \frac{1}{1 - \frac{g_{Q_p x_{vp}}(s)\, g_{p_p x_{vr}}(s)}{g_{Q_p x_{vr}}(s)\, g_{p_p x_{vp}}(s)}} \tag{B.33}$$

$$\Updownarrow$$

$$= \frac{1}{1 - \frac{\frac{a_{13}\,s + a_{12}}{b_3\,s^3 + b_2\,s^2 + b_1\,s + b_0}\,\frac{a_7}{b_3\,s^3 + b_2\,s^2 + b_1\,s + b_0}}{\frac{a_{15}\,s + a_{14}}{b_3\,s^3 + b_2\,s^2 + b_1\,s + b_0}\,\frac{a_6\,s^2 + a_5\,s + a_4}{b_3\,s^3 + b_2\,s^2 + b_1\,s + b_0}}} = \frac{1}{1 - \frac{(a_{13}\,s + a_{12})\,a_7}{(a_{15}\,s + a_{14})\,(a_6\,s^2 + a_5\,s + a_4)}} \tag{B.34}$$

$$\Updownarrow$$

$$= \frac{1}{1 - \frac{a_7\,a_{13}\,s + a_7\,a_{12}}{a_6\,a_{15}s^3 + (a_5\,a_{15} + a_6\,a_{14})\,s^2 + (a_4\,a_{15} + a_5\,a_{14})\,s + a_4\,a_{14}}} \tag{B.35}$$

$$\Updownarrow$$

$$= \frac{a_6\,a_{15}s^3 + (a_5\,a_{15} + a_6\,a_{14})\,s^2 + (a_4\,a_{15} + a_5\,a_{14})\,s + a_4\,a_{14}}{a_6\,a_{15}s^3 + (a_5\,a_{15} + a_6\,a_{14})\,s^2 + (a_4\,a_{15} + a_5\,a_{14})\,s + a_4\,a_{14} - a_7\,a_{13}\,s + a_7\,a_{12}} \tag{B.36}$$

The coefficients are substituted and it is found that:

$$\lambda_{p,v}^{d} = -\frac{\left(\beta_p k_{Q_p,p_p} - V_p s\right)\left(\beta_r M k_{Q_r,p_r} s + M\,V_r s^2 + \beta_r {A_r}^2\right)}{{A_p}^2 \beta_p\left(\beta_r k_{Q_r,p_r} + V_r s\right) - \left(\beta_p k_{Q_p,p_p} - V_p s\right)\left(\beta_r M k_{Q_r,p_r} s + M\,V_r s^2 + \beta_r {A_r}^2\right)} \tag{B.37}$$

The rest of the relative gains are derived in the same way.

B.3.1 Low Frequency Range

The black contours in Figure B.1 are identical to Figure 5.8 but the load force is defined as Equation (B.38) where the supply pressure is overdimensioned compared to the load force.

$$
\begin{aligned}
F_{l,neg} &= 0.1\, p_s\, A_p - 0.5\, p_s\, A_r \\
F_{l,pos} &= 0.5\, p_s\, A_p - 0.1\, p_s\, A_r
\end{aligned}
\tag{B.38}
$$

Assuming the maximum pressure to be supply pressure, the system can reach steady state for larger load forces, than the system is designed for.

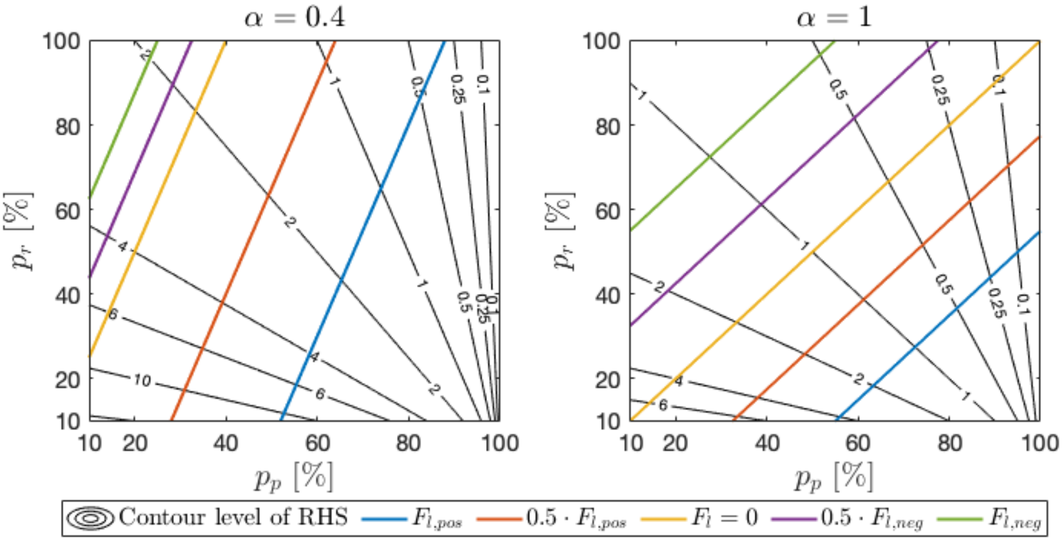

Figure B.1: Contour plot showing the value of the right hand side, RHS, of Equation 5.48.

For steady state to be reached, only the pressure combinations between the green and blue contours are viable. As seen from the figure, an over-dimensioned supply pressure will reduce the pressure working area compared to Figure 5.8.

Appendix C

Dynamic Modelling and Implementation

C.1 Valve Dynamics

The valve dynamics of the experimental test setup are estimated in this appendix. The purpose is to model the relation between a valve reference and the actual valve opening. The actuation limit is taken into account during controller design and implemented in the non-linear simulation model. The approximations are based on the closed loop frequency response for the valve spool following references of $\pm 10\%$ of max stroke length. It is assumed that a second order transfer function can sufficiently capture the dynamics. The frequency response is limited for a larger change in stroke length by including slew rate limitations in the model.

C.1.1 Main Cylinder Valves

The valves connected to the main cylinder are manufactured by *Moog* and will be referred to as *Moog*[Moog, 2020]. The approximated bode diagram is shown in Figure C.1.

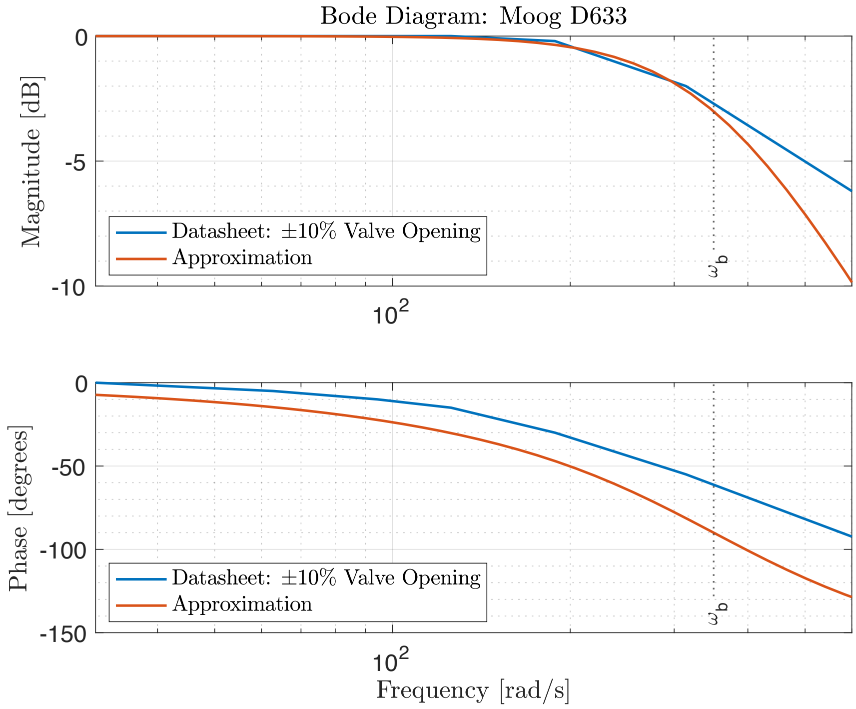

Figure C.1: Bode diagram comparison of datasheet and approximated valve transfer function. The bandwidth is approximately 350 [rad/s].

It is seen how the magnitudes are very similar until the bandwidth frequency. The phase lag is generally approximately 10 [degrees] larger for the approximation than the datasheet. As the resemblance is considered sufficient, and the approximation is more conservative than the datasheet, the approximation is deemed valid. The transfer function, $G_{Moog}(s)$, natural frequency, $\omega_{n,Moog}$, and damping ratio, ζ_{Moog}, are shown in Equation (C.1).

$$G_{Moog}(s) = \frac{x_{v,Moog}}{x^*_{v,Moog}} = \frac{122.5\,10^3}{s^2 + 495\,s + 122.5\,10^3} \qquad \begin{aligned} \omega_{n,Moog} &= 350\,[rad/s] \\ \zeta_{Moog} &= 0.707 \end{aligned} \tag{C.1}$$

In Equation (C.1), $x^*_{v,Moog}$ is the valve opening reference and $x_{v,Moog}$ is the actual valve opening. The slew rate limitation is found by looking at the step response of the valve opening in the datasheet which is shown in Figure C.2 and the estimation is shown in Figure C.3.

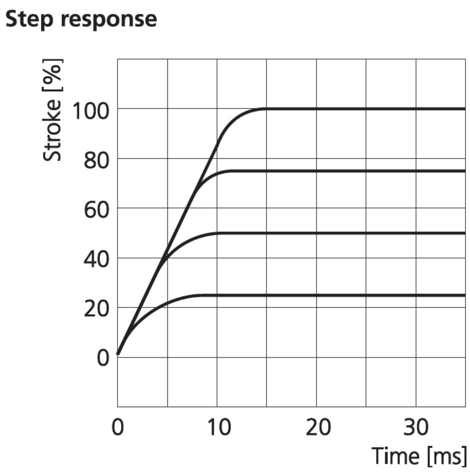

Figure C.2: Step response for MOOG D633 valve[Moog, 2020].

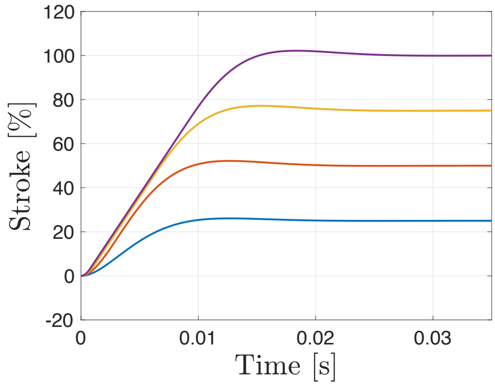

Figure C.3: Estimated step response for MOOG D633 valve.

The slope of the response in Figure C.2 is found to be $\dot{x}_{v,Moog,lim} = 8$ [%/ms]. The valve dynamics are implemented as shown in Figure C.4.

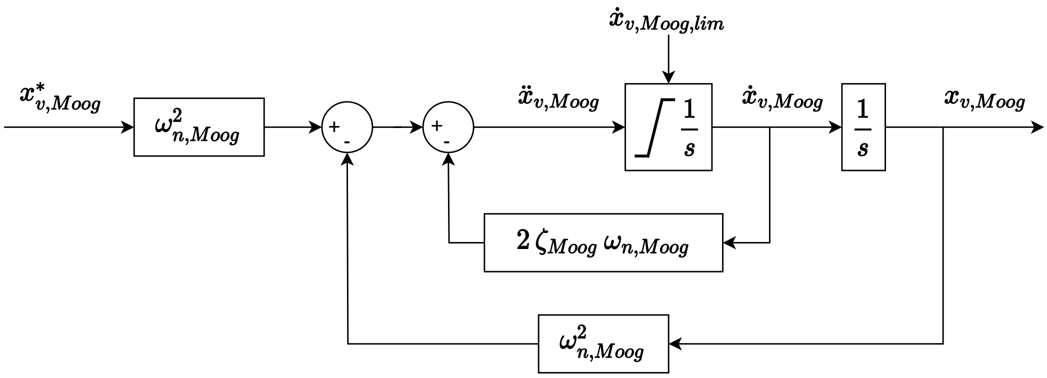

Figure C.4: Implementation of valve dynamics for Moog valves.

C.1.2 Load Cylinder Valve

The valve connected to the load cylinder is manufactured by Bosch Rexroth and will be referred to as *Rexroth*[Rexroth, 2020]. The estimated bode diagram is shown in Figure C.5.

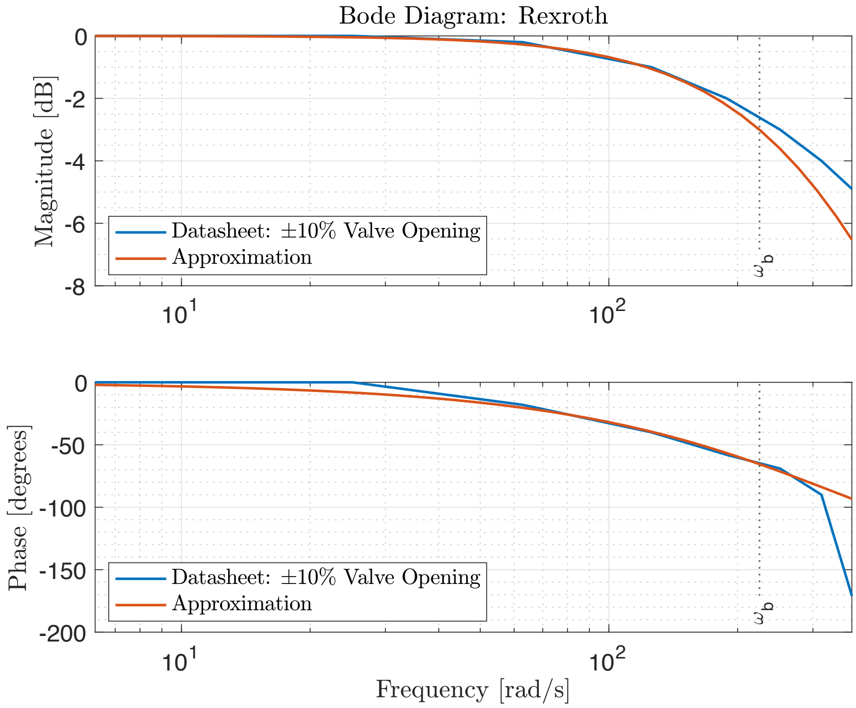

Figure C.5: Bode diagram comparison of datasheet and approximated valve transfer function. The bandwidth is approximately 225 [rad/s].

It can be seen how both the magnitude and phase of the approximation is captured for the relevant frequencies until the bandwidth of the valve. The frequency response is therefore deemed valid and the transfer function is shown in Equation (C.2), where $G_{Rexroth}(s)$ is the transfer function, $\omega_{n,Rexroth}$ is the natural frequency, and $\zeta_{Rexroth}$ is the damping ratio.

$$G_{Rexroth}(s) = \frac{x_{v,Rexroth}}{x^*_{v,Rexroth}} = \frac{122.5\,10^3}{s^2 + 700\,s + 122.5\,10^3} \qquad \begin{aligned} \omega_{n,Rexroth} &= 350\,[rad/s] \\ \zeta_{Rexroth} &= 1 \end{aligned} \tag{C.2}$$

In Equation (C.2), $x^*_{v,Rexroth}$ is the valve opening reference and $x_{v,Rexroth}$ is the actual valve opening. The slew rate limitation is found by looking at the step response of the valve opening in the datasheet as for the Moog valve. The slew rate limitation is found to be $\dot{x}_{v,Rexrooth,lim} = 3.5$ [%/ms]. The valve dynamics are implemented as shown in Figure C.6.

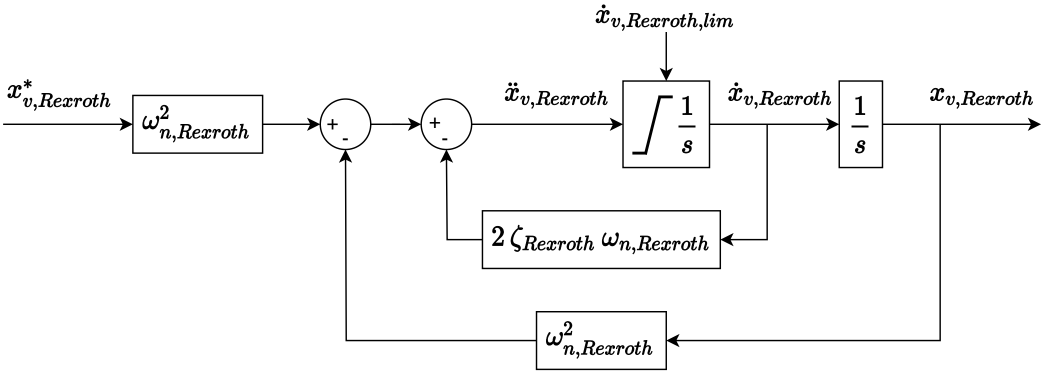

Figure C.6: Implementation of valve dynamics for Rexrooth valve.

C.2 Discrete Implementation

The discrete implementation is presented in this section to represent the physical test setup. The sampling frequency for discrete calculations in the simulations is set to the frequency of the microcontroller by adding a zero-order hold block to the output signal of the controller before the plant which is the valve reference signal. This limits the execution time of the controller.

Noise, n, is added to the measurement signals during feedback and the implementation can be seen in Figure C.7 for signal x.

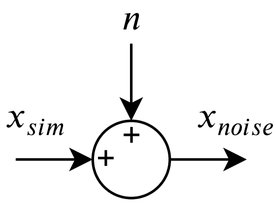

Figure C.7: Noise generation for feedback signals.

The noise amplitude is based on the amplitude of the measured experimental signals. The pressure noise is based on a four-second pressure measurement with a mean value of zero. The velocity noise is based on a four-second position measurement with a mean value of zero. The position measurement is multiplied by a gain to decrease the magnitude as the units differ. The noise of the signals is then looped and added to the simulated signal as seen in Figure C.7.

C.3 Mechanical Model

The pitch acceleration, $\ddot{\theta}$, is expressed as a function of the main piston position. The pitch angle, θ, is related to the main cylinder pitch angle, θ_m, by Equation (C.3). The coefficient c is constant which implies that $\dot{\theta}_m = \dot{\theta}$ and $\ddot{\theta}_m = \ddot{\theta}$.

$$\theta_m = \theta + c \tag{C.3}$$

The pitch acceleration can thereby be found by deriving θ_m. The law of cosines is used to relate the angles to the piston positions from Figure 7.4 as expressed in Equation (C.4).

$$\theta_m = cos^{-1}\left(\frac{r_m^2 + H_m^2 - S_m^2}{2 r_m H_m}\right), \qquad S_m = S_{m,min} + x_m \tag{C.4}$$

The angle is differentiated with respect to time once and twice to get angular velocity and acceleration in Equation (C.5) and (C.6), respectively.

$$\dot{\theta}_m = \underbrace{\frac{\partial \theta_m}{\partial x_m}}_{G_m} \frac{\partial x_m}{\partial t} = G_m\, \dot{x}_m \tag{C.5}$$

$$\ddot{\theta}_m = \dot{G}_m\, \dot{x}_m + G_m\, \ddot{x}_m, \qquad \dot{G}_m = \underbrace{\frac{\partial G_m}{\partial x_m}}_{G_n} \frac{\partial x_m}{\partial t} = G_n\, \dot{x}_m \tag{C.6}$$

Finally, the pitch acceleration is expressed as a function of the main piston position and velocity in Equation (C.7).

$$\ddot{\theta} = G_n\, \dot{x}_m^2 + G_m\, \ddot{x}_m \tag{C.7}$$

The angles ψ_m and ψ_l from Equation (7.10) are expressed as a function of the main piston position using the law of cosines in Equations (C.8) and (C.9).

$$\psi_m = cos^{-1}\left(\frac{r_m^2 + (S_{m,min} + x_m)^2 - H_m^2}{2\, r_m\, (S_{m,min} + x_m)}\right) \tag{C.8}$$

$$\psi_l = cos^{-1}\left(\frac{r_l^2 + S_l^2 - H_l^2}{2\, r_l\, S_l}\right) \tag{C.9}$$

$$S_l = \sqrt{r_l^2 + H_l^2 - 2\, r_l\, H_l\, cos(\theta_l)} \tag{C.10}$$

$$\theta_l = \theta_{tot} - cos^{-1}\left(\frac{r_m^2 + H_m^2 - (S_{m,min} + x_m)^2}{2\, r_l\, (S_{m,min} + x_m)}\right) \tag{C.11}$$

where $\theta_{tot} = \theta_m + \theta_l$ which is constant, is evaluated at $\theta_{tot} = \theta_{m,max} + \theta_{l,min}$. The angle, ψ_l, is expressed as a function of x_m by substituting θ_l from Equation (C.11) into Equation (C.10) which is further substituted into Equation (C.9).

The pitch acceleration, $\ddot{\theta}$, and the angles, ψ_m and ψ_l, are substituted into Newton's Second Law from Equation (7.12) to express the mechanical model in actuator space. The mechanical model is expressed in actuator space in Equation (C.12).

$$\ddot{x}_m = \frac{1}{I_{eq}\, G_m}\Big(F_m\, G_{m1} - (B\, G_m + I_{eq}\, G_n\, \dot{x}_m)\, \dot{x}_m - tanh(\dot{x}_m\, c)\, \tau_C - F_l\, G_{l1}\Big) \tag{C.12}$$

G_m, G_n, G_{m1}, and G_{l1} are expressed in Equation (C.13).

$$\begin{aligned}
G_m &= \frac{S_m}{H_m\, r_m \sqrt{1 - \frac{(H_m^2 - S_m^2 + r_m^2)^2}{4\, H_m^2\, r_m^2}}} \\
G_n &= \frac{1}{H_m\, r_m \sqrt{1 - \frac{(H_m^2 - S_m^2 + r_m^2)^2}{4\, H_m^2\, r_m^2}}} - \frac{S_m^2 (H_m^2 - S_m^2 + r_m^2)}{2\, H_m^3\, r_m^3 \left(1 - \frac{(H_m^2 - S_m^2 + r_m^2)^2}{4\, H_m^2\, r_m^2}\right)^{\frac{3}{2}}} \\
G_{m1} &= \frac{r_m}{2}\sqrt{4 - \frac{(H_m^2 - S_m^2 + r_m^2)^2}{H_m^2\, r_m^2}} \\
G_{l1} &= r_l \sqrt{\frac{sin\left(\theta_{tot} - cos^{-1}\left(\frac{H_m^2 - S_m^2 + r_m^2}{2\, H_m\, r_m}\right)\right)^2 H_l^2}{H_l^2 - 2\, H_l\, cos\left(\theta_{tot} - cos^{-1}\left(\frac{H_m^2 - S_m^2 + r_m^2}{2\, H_m\, r_m}\right)\right) r_l + r_l^2}}
\end{aligned} \tag{C.13}$$

It should be noted that G_m, G_n, G_{m1}, and G_{l1} are all functions of the main piston position, x_m, as $S_m = S_{m,min} + x_m$.

C.4 Load Force

In this section the maximum load force is determined. The maximum allowed load force is derived from Newton's Second Law in actuator space shown in Equation (C.14) in steady state.

$$0 = F_m\, G_{m1} - (B\, G_m + I_{eq}\, G_n\, \dot{x}_m)\, \dot{x}_m - tanh(\dot{x}_m\, c)\, \tau_C - F_l\, G_{l1} \tag{C.14}$$

By rearranging Equation (C.14) and neglecting the Coulomb and viscous friction terms, the maximum positive and negative load force, $F_{l,pos}$ and $F_{l,neg}$, are defined from the maximum positive and negative piston force, $F_{m,pos}$ and $F_{m,neg}$, in Equations (C.15) and (C.16).

$$F_{l,pos} = F_{m,pos}\frac{G_{m1}}{G_{l1}}, \qquad F_{m,pos} = p_s A_{mp} - p_t A_{mr} \tag{C.15}$$

$$F_{l,neg} = F_{m,neg}\frac{G_{m1}}{G_{l1}}, \qquad F_{m,neg} = p_t A_{mp} - p_s A_{mr} \tag{C.16}$$

It should be noted that as G_{m1} and G_{l1} depend on the piston position, $F_{l,pos}$ and $F_{l,neg}$ will also depend on the piston position. By the defined maximum positive and negative load force, the piston force is guaranteed to be equal to or larger than the load force, if the load carrying chamber is supply pressure and the non-load carrying chamber is tank pressure. It is decided to further reduce the load force which allow the control of the pressures for any given load force. This is analysed in the following section along with the maximum velocity and pressure references depending on the load force.

C.4.1 Limitations of References

In this section, the maximum allowed velocity and pressure references are determined. For simplicity, these limitations are found in steady state. For a constant velocity, Equation (C.17) must equal Equation (C.18), when both x_{vmp} and x_{vmr} are positive or both negative.

$$\dot{x}_m = \begin{cases} \frac{1}{A_{mp}} k_{vm}\, x_{vmp} \sqrt{|p_s - p_{mp}|}\,, & x_{vmp} \geq 0 \\ \frac{1}{A_{mp}} k_{vm}\, |x_{vmp}| \sqrt{|p_t - p_{mp}|}\,, & x_{vmp} < 0 \end{cases} \tag{C.17}$$

$$\dot{x}_m = \begin{cases} \frac{1}{A_{mr}} k_{vm}\, x_{vmr} \sqrt{|p_{mr} - p_t|}\,, & x_{vmr} \geq 0 \\ \frac{1}{A_{mr}} k_{vm}\, |x_{vmr}| \sqrt{|p_{mr} - p_s|}\,, & x_{vmr} < 0 \end{cases} \tag{C.18}$$

Furthermore, p_{mp} and p_{mr} are determined from Newton's Second Law in steady state from Equation (C.14) and by neglecting the Coulomb and viscous friction terms, the load force term is isolated as Equation (C.19), where G_{m1} and G_{l1} are position dependent.

$$F_l\, G_{l1} = (p_{mp}\, A_{mp} - p_{mr}\, A_{mr}\,)\, G_{m1} \tag{C.19}$$

Choosing the load forces, F_l, and piston positions, x_m, the possible pressure combinations of p_{mp} and p_{mr} are determined from Equation (C.19).

By inserting the pressure combinations into Equations (C.17) and (C.18), and having $x_{vmp} = 100$ [%] and $x_{vmr} = 100$ [%], the maximum positive steady state velocity is found as a function of p_{mp}, p_{mr}, F_l, and x_m. The maximum steady state velocity is, however, limited by lowest velocity of Equation (C.17) and (C.18) where either x_{vmp} or x_{vmr} is reduced from fully opened to guarantee both equations result in the same steady state velocity. This is shown in Figure C.8 for positive velocity where both x_{vmp} and x_{vmr} are fully opened. The steady state velocity is found where the graphs intersect.

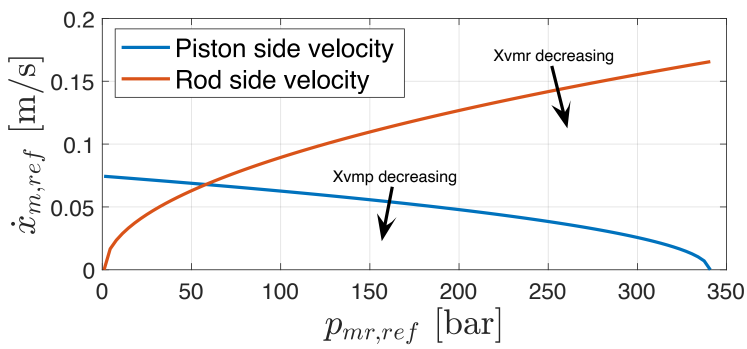

Figure C.8: The positive piston side velocity from Equation (C.17) and rod side velocity from Equation (C.18) for $x_m = 50$ [%] of stroke length and no load force.

Since the velocity found from the piston side in Equation (C.17) must equal Equation (C.18) describing the velocity found from the rod side, x_{vmr} must be reduced if pressure references above approximately 60 [bar] are desired. Below 60 [bar] x_{vmp} must be reduced. The maximum negative steady state velocity depending on the pressure reference is similarly found where x_{vmp} and x_{vmr} are negative. The available velocity reference dependent on the pressure reference is shown in Figure C.9 for the four cases used for the control combination analysis shown in Figure 3.2.

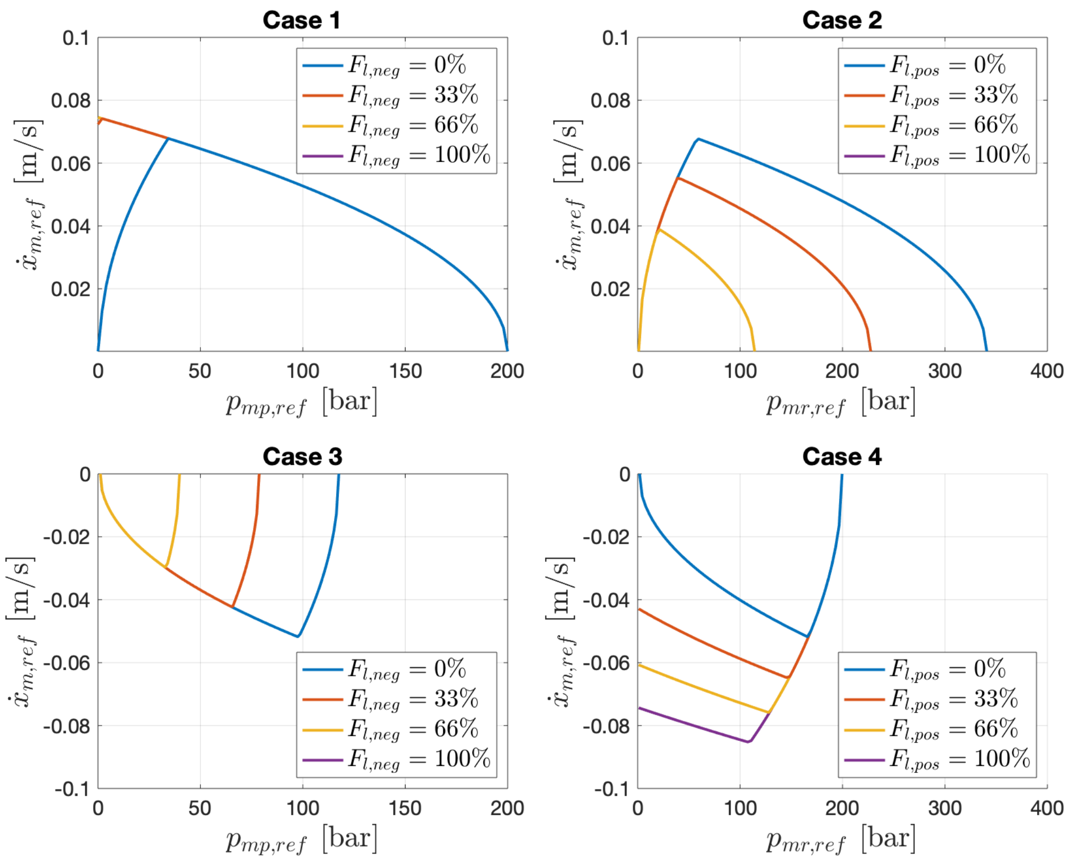

Figure C.9: The limitations of the pressure and velocity references for positive and negative load force, where $p_s = 200$ [bar].

The load force is varied to observe how it affects the pressure and velocity reference. Figure C.9 is only shown for $x_m = 50$ [%] of stroke length. It must be noticed, that the limits of the velocity and pressure references are partly on top of each other when the load force changes. For case 2 and 3, when the load force increases, the available pressure and velocity references are more limited. When $F_{l,pos} = 100$ [%] in case 2 and $F_{l,neg} = 100$ [%] in case 3, only one pressure combination results in zero acceleration and the velocity becomes 0 [m/s]. The purple line is therefore not seen. For case 1 and 4, when the load force increases, the available pressure and velocity references are increased. For case 1 the load forces for $F_{l,neg} = 33$ [%], 66 [%] and 100 [%] are on top of each other and showed as the red line in the plot. The velocity and pressure references are therefore equally limited at $F_{l,neg} = 33$, 66 and 100 [%] for case 1.

To ensure a wide range of pressure and velocity references for the four cases, it is chosen to limit the load force F_l to maximum 66 [%] of $F_{l,pos}$ and $F_{l,neg}$.

As G_{l1} is position dependent, the load force term $F_l\, G_{l1}$ will not be 66 [%] of the maximum piston force for all piston positions if F_l is constant for all piston positions. It is therefore chosen to have three different values of F_l which ensure, that $F_l\, G_{l1} = 0.66 \cdot F_{m,pos}\, G_{m1}$ for $x_m = 10$, 50 and 90 [%]. This is illustrated in Figure C.10, where the maximum allowed load force will change between the yellow, purple, and green load force depending on the piston position. The same applies for the negative load force.

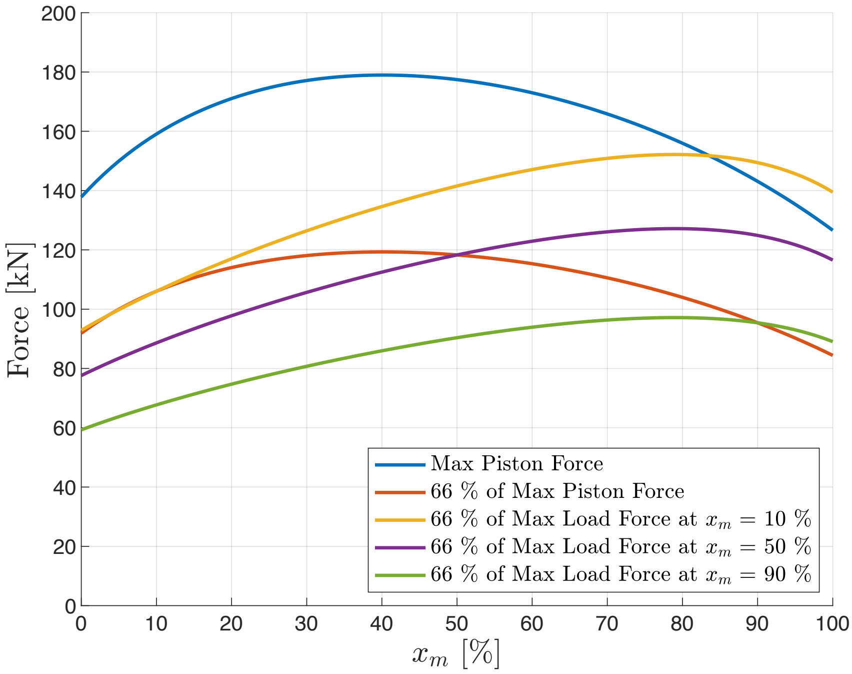

Figure C.10: The load force change between the yellow, purple, and green load force depending on the piston position.

C.5 Linear Model Validation

The linear model is validated by comparing step responses of the linear models with the non-linear model for several arbitrarily chosen linearisation points, hence comparing each linear model with the non-linear model. The validation is conducted to verify if the linear model correctly depicts the system dynamics and can be used as a representation for system analysis and control purposes.

The models are stepped from the linearised operating points and the step size is small to validate the linear model in the vicinity of the operating point. The hydraulic model of the load side cylinder is omitted, and the load force is set to zero. To linearise the non-linear model, six dependent operating points must be found; piston position, x_m^*, piston velocity, $\dot{x}_m^*$, piston side pressure, p_{mp}^*, rod side pressure, p_{mr}^*, piston side valve opening, x_{vmp}^* and rod side valve opening, x_{vmr}^*. The three dynamic equations for the system are solved in steady state; Newtons second law from Equation (7.14) and two continuity equations from Equation (7.6) i.e. where $\ddot{x}_m = 0$, $\dot{p}_{mp} = 0$, and $\dot{p}_{mr} = 0$. Three operating points should, therefore, be chosen and the remaining three are calculated using the steady state equations. Figures C.11, C.12 and C.13 show the step response of the velocity and piston side pressure of the non-linear and linear models when linearised in three different piston positions.

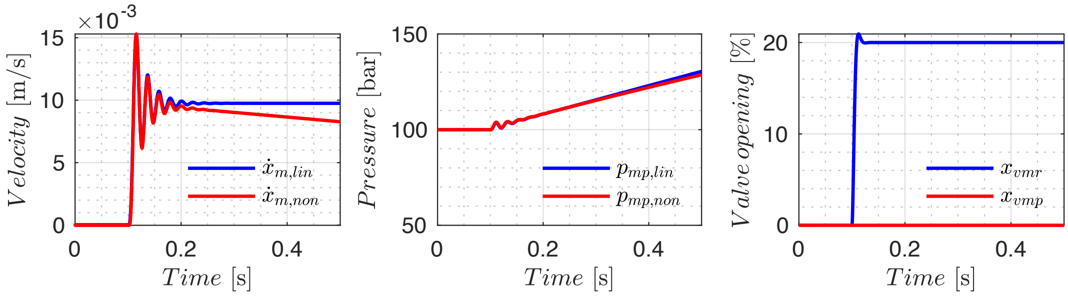

Figure C.11: Linearisation points: $x_m^* = 10\,[\%]$, $\dot{x}_m^* = 0\,[m/s]$, $p_{mp}^* = 100\,[bar]$, $p_{mr}^* = 170\,[bar]$, $x_{vmp}^* = 0\,[\%]$, $x_{vmr}^* = 0\,[\%]$.

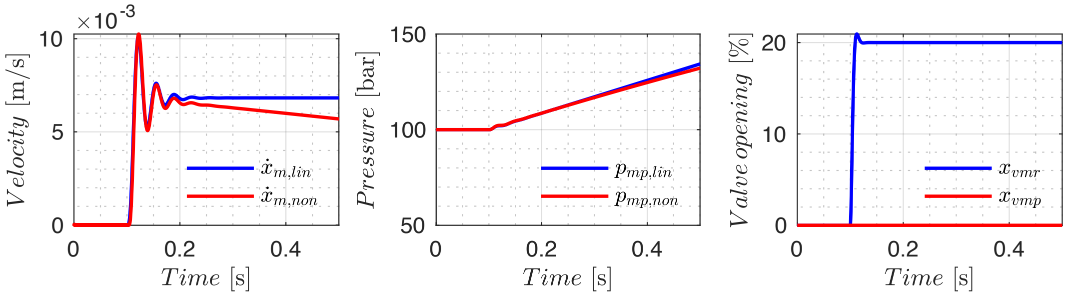

Figure C.12: Linearisation points: $x_m^* = 50\,[\%]$, $\dot{x}_m^* = 0\,[m/s]$, $p_{mp}^* = 100\,[bar]$, $p_{mr}^* = 170\,[bar]$, $x_{vmp}^* = 0\,[\%]$, $x_{vmr}^* = 0\,[\%]$.

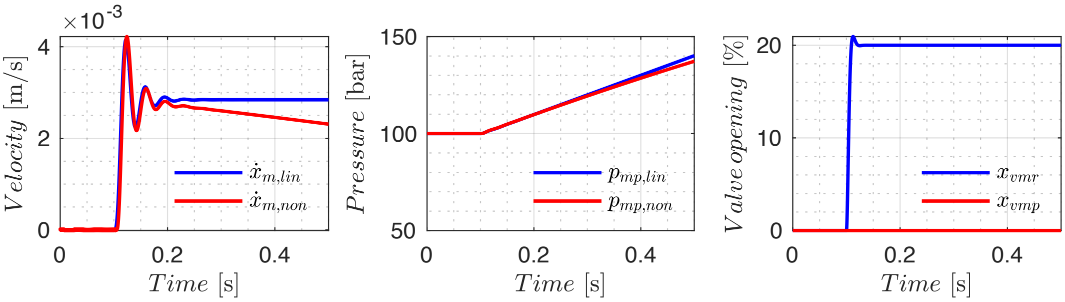

Figure C.13: Linearisation points: $x_m^* = 90\,[\%]$, $\dot{x}_m^* = 0\,[m/s]$, $p_{mp}^* = 100\,[bar]$, $p_{mr}^* = 170\,[bar]$, $x_{vmp}^* = 0\,[\%]$, $x_{vmr}^* = 0\,[\%]$.

Figure C.14 shows the velocity and rod side pressure.

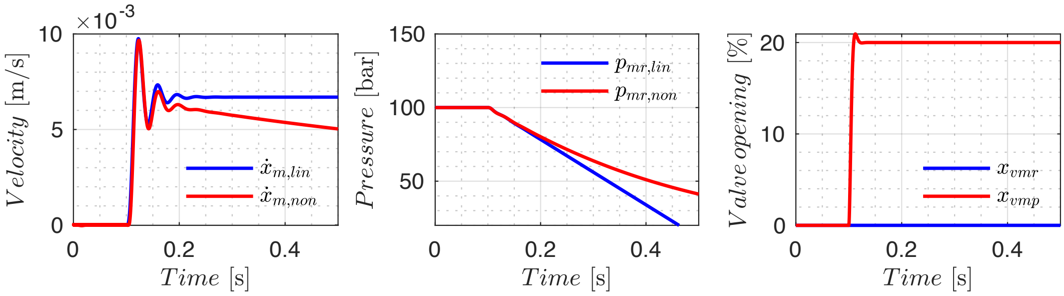

Figure C.14: Linearisation points: $x_m^* = 50\,[\%]$, $\dot{x}_m^* = 0\,[m/s]$, $p_{mp}^* = 59\,[bar]$, $p_{mr}^* = 100\,[bar]$, $x_{vmp}^* = 0\,[\%]$, $x_{vmr}^* = 0\,[\%]$.

Figure C.15 shows the velocity and piston side pressure when both valves are stepped.

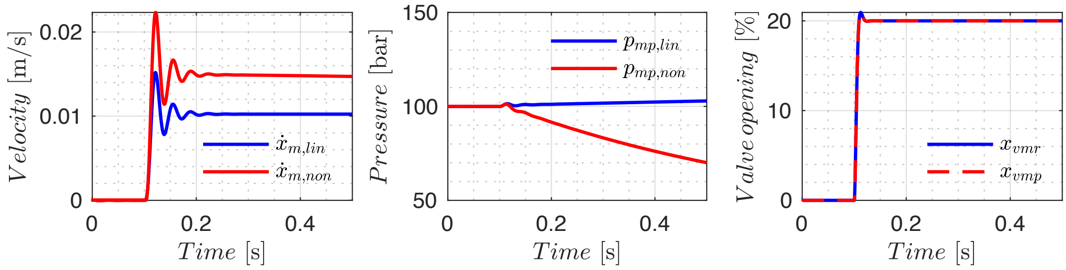

Figure C.15: Linearisation points: $x_m^* = 50\,[\%]$, $\dot{x}_m^* = 0\,[m/s]$, $p_{mp}^* = 100\,[bar]$, $p_{mr}^* = 170\,[bar]$, $x_{vmp}^* = 0\,[\%]$, $x_{vmr}^* = 0\,[\%]$.

The response has been examined for several other linear models were linearisation points for piston positions, velocity magnitudes and directions, valve input magnitudes and directions, and pressures were varied and the general dynamics were captured. *The linear model is therefore deemed valid for further analysis.*

Appendix D

Control

D.1 Pole Placement

A way to get all solutions of the $\mathbf{K}_{PP}$ matrix is by using the method described in [Brogan, 1991]. The eigenvalues of the closed loop system are the roots of the expression in Equation (D.1), where λ_i refers to the ith desired eigenvalue and $i = 1, 2, 3$[Brogan, 1991, p. 448].

$$det(\lambda_i \, \mathbf{I} - (\mathbf{A} - \mathbf{B} \, \mathbf{K}_{PP})) = 0 \tag{D.1}$$

It is seen from Equation (D.1) that there is at least one non-zero vector, $\boldsymbol{\psi}_i$, according to Equation (D.2).

$$(\lambda_i \, \mathbf{I} - (\mathbf{A} - \mathbf{B} \, \mathbf{K}_{PP})) \, \boldsymbol{\psi}_i = \mathbf{0} \tag{D.2}$$

$$\Updownarrow$$

$$(\mathbf{A} - \mathbf{B} \, \mathbf{K}_{PP}) \, \boldsymbol{\psi}_i = \lambda_i \, \boldsymbol{\psi}_i \tag{D.3}$$

From Equation (D.3) it is seen that $\boldsymbol{\psi}_i$ is an eigenvector of the closed loop system associated with the eigenvalue λ_i[Brogan, 1991, p. 449-451]. Equation (D.2) is rewritten in Equation (D.4).

$$\begin{bmatrix}(\lambda_i - \mathbf{A}) & \mathbf{B}\end{bmatrix} \underbrace{\begin{bmatrix}\boldsymbol{\psi}_i \\ \mathbf{K}_{PP}\,\boldsymbol{\psi}_i\end{bmatrix}}_{\boldsymbol{\xi}_i} = \mathbf{0} \tag{D.4}$$

For each of the three desired eigenvalues, λ_i, Equation (D.4) is solved for the corresponding unknown $\boldsymbol{\xi}_i$. It should be noted that there are r, i.e. the number of inputs, independent solution vectors $\boldsymbol{\xi}_i$ for each λ_i when solving Equation (D.4)[Brogan, 1991, p. 450]. In Equation (D.4) the n, i.e. the order of the system matrix $\mathbf{A}$, top components of each column of $\boldsymbol{\xi}_i$ form a closed loop eigenvector, $\boldsymbol{\psi}_i$, and the remaining bottom components are the matrix $\mathbf{K}_{PP}$ multiplied by the same vector[Brogan, 1991, p. 449-451].

Equation (D.4) contains three linear equations and by selecting two elements of $\boldsymbol{\xi}_i$, the values of the remaining elements can be found. The three $\boldsymbol{\xi}$ vectors are shown in Equation (D.5) where α_i and β_i are values which need to be specified and γ_i, δ_i, and σ_i are functions of these values. γ_i, δ_i, and σ_i are found by solving Equation (D.4).

$$\begin{aligned}
\boldsymbol{\xi}_1 &= \begin{bmatrix}\alpha_1 & \beta_1 & \gamma_1(\alpha_1,\beta_1) & \delta_1(\alpha_1,\beta_1) & \sigma_1(\alpha_1,\beta_1)\end{bmatrix}^T \\
\boldsymbol{\xi}_2 &= \begin{bmatrix}\alpha_2 & \beta_2 & \gamma_2(\alpha_2,\beta_2) & \delta_2(\alpha_2,\beta_2) & \sigma_2(\alpha_2,\beta_2)\end{bmatrix}^T \\
\boldsymbol{\xi}_3 &= \begin{bmatrix}\alpha_3 & \beta_3 & \gamma_3(\alpha_3,\beta_3) & \delta_3(\alpha_3,\beta_3) & \sigma_3(\alpha_3,\beta_3)\end{bmatrix}^T
\end{aligned} \tag{D.5}$$

By varying α_i and β_i it can be found that each of the $\boldsymbol{\xi}$ vectors contains two linear independent vectors since $r = 2$. This is shown in Equation (D.6) for two inputs where the matrix $\mathbf{U}$ is partitioned.

$$\mathbf{U}(\lambda_i) = \begin{bmatrix}\psi_1 & \psi_2 \\ F_1 & F_2\end{bmatrix} = \begin{bmatrix}\boldsymbol{\psi}(\lambda_i) \\ \mathbf{F}(\lambda_i)\end{bmatrix} \tag{D.6}$$

$\mathbf{U}(\lambda_1)$, $\mathbf{U}(\lambda_2)$, and $\mathbf{U}(\lambda_3)$ are found using Equation (D.6). Substituting $\mathbf{F}_i = \mathbf{K}_{PP}\,\boldsymbol{\psi}_i$ yields Equation (D.7).

$$\mathbf{K}_{PP}\underbrace{\begin{bmatrix}\psi(\lambda_1) & \psi(\lambda_2) & \psi(\lambda_3)\end{bmatrix}}_{\boldsymbol{\Delta}} = \underbrace{\begin{bmatrix}F(\lambda_1) & F(\lambda_2) & F(\lambda_3)\end{bmatrix}}_{\boldsymbol{\Gamma}} \tag{D.7}$$

It should be noted that it is an overdetermined system since there is more than one input. Since the system is controllable, n linearly independent columns from both sides of Equation (D.7) can be selected, i.e. one column for each λ_i[Brogan, 1991, p. 451]. However, as each of the $\boldsymbol{\xi}$ vectors in Equation (D.5) contains both vectors, one column for each eigenvalue is automatically chosen by choosing the constants α_i and β_i. The matrices $\boldsymbol{\Gamma}_s$ and $\boldsymbol{\Delta}_s$ contain the selected columns from $\boldsymbol{\Gamma}$ and $\boldsymbol{\Delta}$, respectively. The feedback gain matrix is solved using Equation (D.8).

$$\mathbf{K}_{PP} = \boldsymbol{\Gamma}_s \, \boldsymbol{\Delta}_s^{-1} \tag{D.8}$$

The feedback gain matrix $\mathbf{K}_{PP}$ is a function of the six parameters: α_1, α_2, α_3, β_1, β_2, and β_3.

D.2 Disturbance and Noise Analysis

The transfer function matrices relating references, disturbances, and measurement noise to the outputs are derived for all control methods in this appendix.

D.2.1 Pole Placement and LQR

The block diagram in Figure 9.14 is valid for both pole placement and LQR and the transfer function matrices are derived based on that. The state equation, system output equation, and system input equation are expressed in Equations (D.9), (D.10), and (D.11), respectively.

$$\dot{\mathbf{x}}_s = \mathbf{A}_s \, \mathbf{x}_s + \mathbf{B}_s \, \mathbf{u}_s + \mathbf{d} \tag{D.9}$$
$$\mathbf{y}_s = \mathbf{C}_s \, \mathbf{x}_s \tag{D.10}$$
$$\mathbf{u}_s = \mathbf{F}_s \, \mathbf{r}_s - \mathbf{K}_s \, \mathbf{x}_s - \mathbf{K}_s \, \mathbf{n} \tag{D.11}$$

Equation (D.11) is the substituted into Equation (D.9) yielding Equation (D.12).

$$\begin{aligned} &\dot{\mathbf{x}}_s = \mathbf{A}_s \, \mathbf{x}_s + \mathbf{B}_s \, \mathbf{F}_s \, \mathbf{r}_s - \mathbf{B}_s \, \mathbf{K}_s \, \mathbf{x}_s - \mathbf{B}_s \, \mathbf{K}_s \, \mathbf{n} + \mathbf{d} \\ &\Updownarrow \\ &(s \, \mathbf{I} - \mathbf{A}_s + \mathbf{B}_s \, \mathbf{K}_s) \, \mathbf{x}_s = \mathbf{B}_s \, \mathbf{F}_s \, \mathbf{r}_s - \mathbf{B}_s \, \mathbf{K}_s \, \mathbf{n} + \mathbf{d} \end{aligned} \tag{D.12}$$

Substituting Equation (D.10) into Equation (D.12) yields:

$$(s\,\mathbf{I} - \mathbf{A}_s + \mathbf{B}_s\,\mathbf{K}_s)\,\mathbf{C}_s^{-1}\,\mathbf{y}_s = \mathbf{B}_s\,\mathbf{F}_s\,\mathbf{r}_s - \mathbf{B}_s\,\mathbf{K}_s\,\mathbf{n} + \mathbf{d} \tag{D.13}$$

By rearranging Equation (D.13), the transfer function matrices are expressed as shown in Equation (D.14).

$$\begin{aligned}\mathbf{y}_s = &\underbrace{\mathbf{C}_s\,(s\,\mathbf{I} - \mathbf{A}_s + \mathbf{B}_s\,\mathbf{K}_s)^{-1}\,\mathbf{B}_s\,\mathbf{F}_s}_{\mathbf{G}_{cl}}\;\mathbf{r}_s + \underbrace{\mathbf{C}_s\,(s\,\mathbf{I} - \mathbf{A}_s + \mathbf{B}_s\,\mathbf{K}_s)^{-1}}_{\mathbf{S}}\;\mathbf{d}\\ &\underbrace{-\mathbf{C}_s\,(s\,\mathbf{I} - \mathbf{A}_s + \mathbf{B}_s\,\mathbf{K}_s)^{-1}\,\mathbf{B}_s\,\mathbf{K}_s}_{\mathbf{T}}\;\mathbf{n}\end{aligned} \tag{D.14}$$

D.2.2 LQI

The block diagram in Figure 9.15 is valid for LQI and the transfer function matrices are derived based on that. The state equations, system output equation, and system input equation are expressed in Equations (D.15), (D.16), (D.17), and (D.18), respectively.

$$\dot{\mathbf{x}}_s = \mathbf{A}_s\,\mathbf{x}_s + \mathbf{B}_s\,\mathbf{u}_s + \mathbf{d} \tag{D.15}$$
$$\dot{\mathbf{z}}_s = \mathbf{r}_s - \mathbf{C}_s\,\mathbf{x}_s - \mathbf{C}_s\,\mathbf{n} \tag{D.16}$$
$$\mathbf{y}_s = \mathbf{C}_s\,\mathbf{x}_s \tag{D.17}$$
$$\mathbf{u}_s = -\mathbf{K}_{I,s}\,\mathbf{z}_s - \mathbf{K}_{LQI,s}\,\mathbf{x}_s - \mathbf{K}_{LQI,s}\,\mathbf{n} \tag{D.18}$$

Substituting Equation (D.18) into Equation (D.15) yields:

$$\begin{aligned}&\dot{\mathbf{x}}_s = \mathbf{A}_s\,\mathbf{x}_s - \mathbf{B}_s\,\mathbf{K}_{I,s}\,\mathbf{z}_s - \mathbf{B}_s\,\mathbf{K}_{LQI,s}\,\mathbf{x}_s - \mathbf{B}_s\,\mathbf{K}_{LQI,s}\,\mathbf{n} + \mathbf{d}\\ &\Updownarrow\\ &(s\,\mathbf{I} - \mathbf{A}_s + \mathbf{B}_s\,\mathbf{K}_{LQI,s})\,\mathbf{x}_s = -\mathbf{B}_s\,\mathbf{K}_{I,s}\,\mathbf{z}_s - \mathbf{B}_s\mathbf{K}_{LQI,s}\,\mathbf{n} + \mathbf{d}\end{aligned} \tag{D.19}$$

Equation (D.16) is then isolated for $\mathbf{z}$ which is substituted into Equation (D.19) yielding Equation (D.20).

$$
\begin{aligned}
(s\,\mathbf{I}-\mathbf{A}_s+\mathbf{B}_s\,\mathbf{K}_{LQI,s})\,\mathbf{x}_s &= -\,\mathbf{B}_s\,\mathbf{K}_{I,s}\,\frac{1}{s}\,\mathbf{I}\,\mathbf{r}_s+\mathbf{B}_s\,\mathbf{K}_{I,s}\,\frac{1}{s}\,\mathbf{I}\,\mathbf{C}_s\,\mathbf{x}_s \\
&\quad +\mathbf{B}_s\,\mathbf{K}_{I,s}\,\frac{1}{s}\,\mathbf{I}\,\mathbf{C}_s\,\mathbf{n}-\mathbf{B}_s\mathbf{K}_{LQI,s}\,\mathbf{n}+\mathbf{d} \\
&\Updownarrow \\
\left(s\,\mathbf{I}-\mathbf{A}_s+\mathbf{B}_s\,\mathbf{K}_{LQI,s}-\mathbf{B}_s\,\mathbf{K}_{I,s}\,\frac{1}{s}\,\mathbf{I}\,\mathbf{C}_s\right)\,\mathbf{x}_s &= -\,\mathbf{B}_s\,\mathbf{K}_{I,s}\,\frac{1}{s}\,\mathbf{I}\,\mathbf{r}_s \\
&\quad +\left(\mathbf{B}_s\,\mathbf{K}_{I,s}\,\frac{1}{s}\,\mathbf{I}\,\mathbf{C}_s-\mathbf{B}_s\mathbf{K}_{LQI,s}\right)\mathbf{n}+\mathbf{d}
\end{aligned}
\tag{D.20}
$$

Substituting Equation (D.17) into Equation (D.20) yields:

$$
\begin{aligned}
\left(s\,\mathbf{I}-\mathbf{A}_s+\mathbf{B}_s\,\mathbf{K}_{LQI,s}-\mathbf{B}_s\,\mathbf{K}_{I,s}\,\frac{1}{s}\,\mathbf{I}\,\mathbf{C}_s\right)\,\mathbf{C}_s^{-1}\,\mathbf{y}_s &= -\,\mathbf{B}_s\,\mathbf{K}_{I,s}\,\frac{1}{s}\,\mathbf{I}\,\mathbf{r}_s \\
&\quad +\left(\mathbf{B}_s\,\mathbf{K}_{I,s}\,\frac{1}{s}\,\mathbf{I}\,\mathbf{C}_s-\mathbf{B}_s\mathbf{K}_{LQI,s}\right)\,\mathbf{n}+\mathbf{d}
\end{aligned}
\tag{D.21}
$$

By rearranging Equation (D.21), the transfer function matrices are expressed as shown in Equation (D.22).

$$
\begin{aligned}
\mathbf{y}_s = & \underbrace{-\,\mathbf{C}_s\,\left(s\,\mathbf{I}-\mathbf{A}_s+\mathbf{B}_s\,\mathbf{K}_{LQI,s}-\mathbf{B}_s\,\mathbf{K}_{I,s}\,\frac{1}{s}\,\mathbf{I}\,\mathbf{C}_s\right)^{-1}\,\mathbf{B}_s\,\mathbf{K}_{I,s}\,\frac{1}{s}\,\mathbf{I}}_{\mathbf{G}_{cl}}\,\mathbf{r}_s \\
& +\underbrace{\mathbf{C}_s\,\left(s\,\mathbf{I}-\mathbf{A}_s+\mathbf{B}_s\,\mathbf{K}_{LQI,s}-\mathbf{B}_s\,\mathbf{K}_{I,s}\,\frac{1}{s}\,\mathbf{I}\,\mathbf{C}_s\right)^{-1}}_{\mathbf{S}}\,\mathbf{d} \\
& +\underbrace{\mathbf{C}_s\,\left(s\,\mathbf{I}-\mathbf{A}_s+\mathbf{B}_s\,\mathbf{K}_{LQI,s}-\mathbf{B}_s\,\mathbf{K}_{I,s}\,\frac{1}{s}\,\mathbf{I}\,\mathbf{C}_s\right)^{-1}\,\left(\mathbf{B}_s\,\mathbf{K}_{I,s}\,\frac{1}{s}\,\mathbf{I}\,\mathbf{C}_s-\mathbf{B}_s\mathbf{K}_{LQI,s}\right)}_{\mathbf{T}}\,\mathbf{n}
\end{aligned}
\tag{D.22}
$$

D.3 Optimal Controller Gains

The weight matrices $\mathbf{Q}$ and $\mathbf{R}$ for the scaled state space model are shown in Equations (D.23) and (D.24) for LQR and LQI, respectively.

$$\mathbf{Q} = \begin{bmatrix} 0.05 & 0 & 0 \\ 0 & 10 & 0 \\ 0 & 0 & 10 \end{bmatrix} \qquad \mathbf{R} = \begin{bmatrix} 100 & 0 \\ 0 & 100 \end{bmatrix} \tag{D.23}$$

$$\mathbf{Q} = \begin{bmatrix} 0.1 & 0 & 0 & 0 & 0 \\ 0 & 10 & 0 & 0 & 0 \\ 0 & 0 & 10 & 0 & 0 \\ 0 & 0 & 0 & 1 \cdot 10^5 & 0 \\ 0 & 0 & 0 & 0 & 1 \cdot 10^5 \end{bmatrix} \qquad \mathbf{R} = \begin{bmatrix} 100 & 0 \\ 0 & 100 \end{bmatrix} \tag{D.24}$$

Bibliography

Brogan, W. L. (1991). Modern control theory. ISBN 0-13-590415-3.

Goodwin, G. C., Graebe, S. F., and Salgado, M. E. (2000). Control system design. ISBN 13 978-0-139-58653-8.

Guangrong, C., Junzheng, W., Shoukun, W., Jiangbo, Z., and Wei, S. (2019). The separate meter in separate meter out control system using dual servo valves based on indirect adaptive robust dynamic surface control. Article.

Hansen, A. H. (2019). Fluid power systems. Draft version 0.4 - A Lecture Note.

Hansen, A. H., Pedersen, H. C., Andersen, T. O., and Wachmann, L. (2011a). Design of energy efficient smismo-els control strategies. Article.

Hansen, A. H., Pedersen, H. C., Andersen, T. O., and Wachmann, L. (2011b). Investigation of energy saving separate meter-in separate meter-out control strategies. Article.

Hoberg, N. H., Clausen, J. M., Mogensen, P. M., Jessen, R. H., and Bak-Jensen, T. (2019). Linear and non-linear load force control of a hil test bench for wind turbine pitch systems. AAU project.

Johansen, P. (2019). Multivariable control course.

MathWorks (2020). Help center place. https://se.mathworks.com/help/control/ref/place.html.

Meriam, J. L. and Kraige, L. G. (2013). Dynamics. ISBN 978-1-118-08345-1.

Moog (2020). Valve datasheet. https://www.moog.com/literature/ICD/Moog-Valves-D633_D634-Catalog-en.pdf.

Pedersen, H. C., Andersen, T. O., Hansen, R. H., and Stubkier, S. (2010). Investigation of separate meter-in separate meter-out control strategies for systems with over centre valves.

Philips, C. L. and Parr, J. M. (2013). Feedback control systems. ISBN 978-93-325-0760-9.

Rath, G. and Zaev, E. (2017). Optimal control for hydraulic system with separate meter-in and separate meter-out. Article.

Rexroth, B. (2020). Valve datasheet. https://dc-kr.resource.bosch.com/media/kr/products_9/data_sheet_8/4wree/re29061_2012-11_wree.pdf.

Skogestad, S. and Postlethwaite, I. (2005). Multivariable feedback control - analysis and design. ISBN-13 978-0-470-01167-6.

TAON (2020). Taon hydraulic component cylinders. https://taon.dk/en/cylinders-4/.

Vedel, S. B., Bendtsen, D. H., Zubarev, S., and Hovda, S. (2019). Controller design for a hil test bench for pitch systems. AAU project.